The Effect of Yttrium on Wear, Corrosion and Corrosive Wear of Mg-Al Alloys

by

Meisam Nouri

A thesis submitted in partial fulfillment of the requirements for the degree of

Doctor of Philosophy

in

Materials Engineering

Department of Chemical and Materials Engineering

University of Alberta

Abstract

Magnesium remarkably deserves considerable interest from industry especially transportation sector because of its high strength to weight ratio. However, poor wear resistance and low corrosion resistance of magnesium are barriers to extend use of its alloys.

Yttrium is one of rare-earth elements which has been demonstrated effectiveness in improving the corrosion resistance and tribological properties of some metallic alloys. In this work, the effects of yttrium on wear, corrosion and corrosive wear of as-cast Mg-3 wt% Al and AZ31 alloys were investigated. It was shown that the added yttrium increased the dry wear resistance of the alloys through the formation of a harder second phases.

The corrosion resistance of the alloys was evaluated in tap water and salt solution. A small amount of added Y improved the corrosion resistance but such benefit decreased at higher yttrium contents. Corrosive wear tests were performed in the same environment for the alloys. The improvement in corrosive wear resistance mainly came from the reduction of corrosion-wear synergy caused by the added yttrium, which increased both hardness and corrosion resistance. Relevant mechanisms to express the observations and the correlation between the performance and microstructure were analyzed and discussed in details.

In addition to modification of the corrosion potential of bulk magnesium through alloying elements, tailoring its surface oxide film is an alternative approach for enhanced resistance to corrosion. In this study, effects of small amounts of a yttrium on the strength of surface oxide film formed on Mg-3 wt% Al alloy and its adherence to the substrate were investigated. It is demonstrated that the yttrium addition decreased the component ratio of hydroxides to oxides, mainly $Mg(OH)_2$ to MgO, in the surface oxide film, leading to markedly enhanced mechanical strength and resis-

tance to scratch with stronger adherence to the substrate. However, as the nominal yttrium concentration exceeded a certain level, the beneficial effect of Y on the film was weakened. Efforts were made to clarify underlying mechanisms.

Surface modification is an effective approach for increasing wear and corrosion resistance of materials without affecting their bulk properties. Among various surface modification techniques, aluminizing is an economical and effective one which has been applied to various alloys. The effectiveness of aluminizing might be further enhanced by alloying with rare earth elements such as yttrium. In this research, effects of yttrium-incorporated aluminizing on the resistance of AZ31 alloy to corrosion, wear, and corrosive wear were investigated. The study demonstrates that aluminizing can be beneficial to the resistance of the alloy to wear, corrosion and corrosive wear. The addition of yttrium increased the benefits, largely attributed to the associated passive film.

Effectiveness of aluminizing can be further enhanced by surface nanocrystallization. In this study, effects of surface nanocrystallization on the effectiveness of aluminizing in enhancing the resistance of AZ31 alloy to corrosion, wear and corrosive wear were investigated. The results demonstrated that aluminizing was effective to increase the resistance of the Mg alloy to surface failures. Surface nanocrystallization expanded the improvement, largely attributed to increased surface hardness and enhanced passivation capability.

Preface

The materials presented in the current thesis are parts of a research supervised by Dr. Dongyang Li. The experiments were conducted in Dr. Dongyang Li's lab and other research labs in The University of Alberta. Some chapters of this thesis have been published in or submitted to peer-reviewed journals and its format is paper-based. Therefore, there might be repetitions in some parts of this thesis.

Chapter 3 of this thesis is published as "Beneficial effects of yttrium on the performance of Mg-3%Al alloy during wear, corrosion and corrosive wear" by Meisam Nouri, Xiaoguang Sun, and D.Y.Li in *Tribology International* 67 (2013) 154-163. The experiments were conducted by Meisam Nouri and Xiaoguang Sun.

Chapter 4 of this thesis is published as "Corrosive wear resistance of Mg-Al-Zn alloys with alloyed yttrium" by Xiaoguang Sun, Meisam Nouri, You Wang, and D.Y.Li in *Wear* 302 (2013) 1624-1632. The experiments were conducted by Meisam Nouri and Xiaoguang Sun.

Chapter 5 of this thesis is published as "The role of minor yttrium in tailoring the failure resistance of surface oxide film formed on Mg alloys" by Meisam Nouri, Ziran Liu, Dongyang Li, Xiaoguo Yan, Nabila Tahreen, and Daolun Chen in *Thin Solid Films* 615 (2016) 29-37. The experiments were conducted by Meisam Nouri and first principle calculations were made by Ziran Liu.

Chapter 7 of this thesis has been submitted as "Maximizing the benefit of aluminizing to AZ31 alloy by surface nanocrystallization for elevated resistance to wear and corrosive wear" by Meisam Nouri and D.Y.Li to *Tribology International*. The experiments were conducted by Meisam Nouri.

Some of the materials have been presented in 2013, 2014, and 2015 *AUTO21 Conference*, *19st International Conference on Wear of Materials* 2013, and *Tribology Frontiers* 2016 Conferences.

To My Mom
Everytime I think about you, it brings tears to my eyes.
I missed you so much.

Acknowledgements

First of all, many thanks to Dr. Dongyang Li for his advice, guidance, and comments. Working under his supervision helped me to improve my knowledge and expand my ability to think more deeply about materials and their properties.

I would like to thank the Chemical and Materials Engineering faculty and academic staff, technical support staff, office support staff and post-doctoral fellows and graduate students for their guidance, comments, training, help and assistance. My special thanks to my colleagues in Dr. Li's research group: Hao Lu, Bin Yu, Ning Fu, Liqiu Guo, Tiger Tang, Shengming Jin, and Guomin Hua.

My special gratitude with no particular order to my dear friends: Elizabeth Sterling Lee, Xioaguang Sun, Ziran Liu, Ata Kamyabi Gol, Pouyan Motamedi, Pouya Delshad Khatibi, Sarang Gumfekar, Kevin Hodder, Mohsen Mohammadijoo, Emad Geramian, Amir Hanifi, Mehdi Alipour, Yashar Behnamian, Taghi Amiri, Neda Sharifzadeh, and especially to Zohreh Salimi, my best friend and wife, for their support and advice.

I also would like to thank Iran Ministry of Science, Research and Technology, The University of Alberta, Auto21, NSERC, Magna International, Suncor, Shell Canada and Volant Products for their support.

I would like to express my heartfelt appreciation to my family, specially to my parents for their endless and unconditional support and love. I am not and will not be able to compensate for all the things they have done for me.

And, this is the first day of rest of my life to start learning about things that I do not know about: Almost everything!

The heart has worked so hard in this road
Yet at the end it seems like it has accomplished nothing

Many sources of light shined on my heart

Yet I don't feel the slightest bit enlightened

- Avicenna.

Contents

List of Figures

List of Tables

Chapter 1

Introduction

1.1 Motivation

With continuously increased global fuel demand, elevated fuel prices, fast dropping of crude oil reserves, and environmental issues, the automobile industry is making great efforts to develop lighter vehicles for fuel economy and less environmental pollution. Light weighting of vehicles with a 5-10% reduction in consumption of fuel for every 10% reduction in weight is an effective way of improving energy efficiency [22]. The new regulations such as Corporate Average Fuel Economy (CAFE) 2025 require many countries worldwide to decrease vehicles emissions through increasing the average number of kilometres per litter of fuel [1] (see Figs 1.1 and 1.2). Almost all automotive manufacturers are now designing 3-5% annual mass reduction as a strategic requirement for their new product development [1]. Over the period from 1977 to 2004, as illustrated in Fig 1.3, the distribution of materials used in the average light duty vehicle shifted to a greater portion for lightweight materials. The graphs show an increase in the use of lightweight materials such as aluminum and magnesium.

Magnesium is the lightest structural metal which is available for vehicle uses. The density of magnesium is 1.74 gcm^{-3} which enables it to reduce the weight of vehicle components by up to 70% relative to steels [2] (see Fig 1.4). In addition to its lightness, magnesium has other useful properties such as high strength-to-weight ratio, vibration

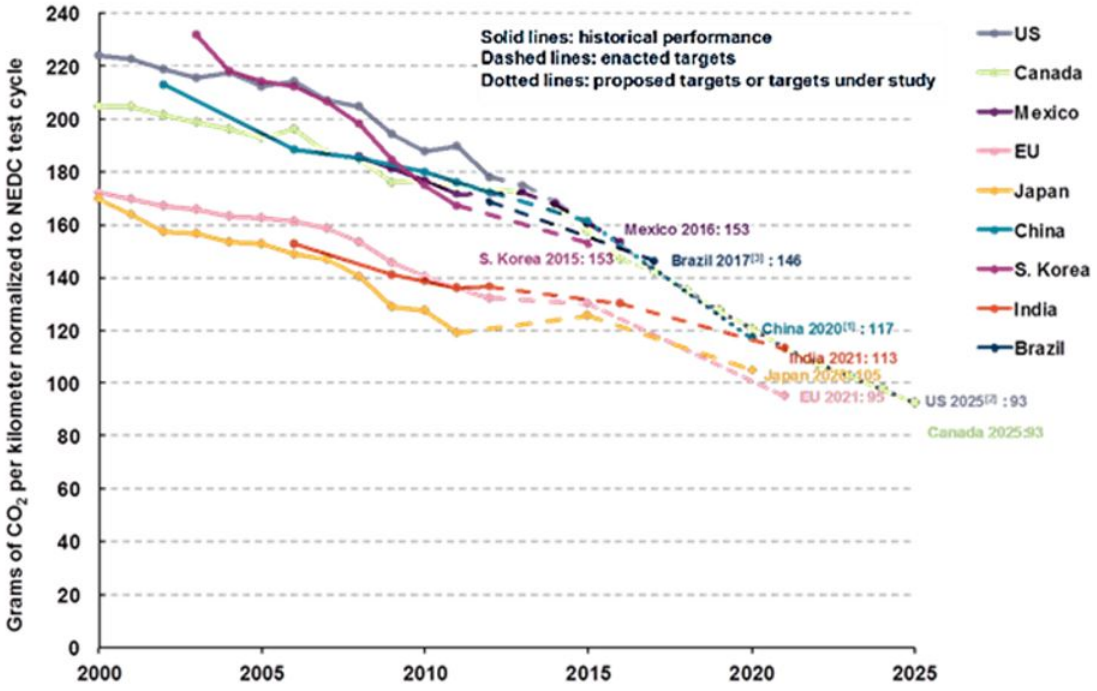

Figure 1.1: 2025 Corporate Average Fuel Economy (CAFE) regulations on emissions for vehicles. The data is from [1].

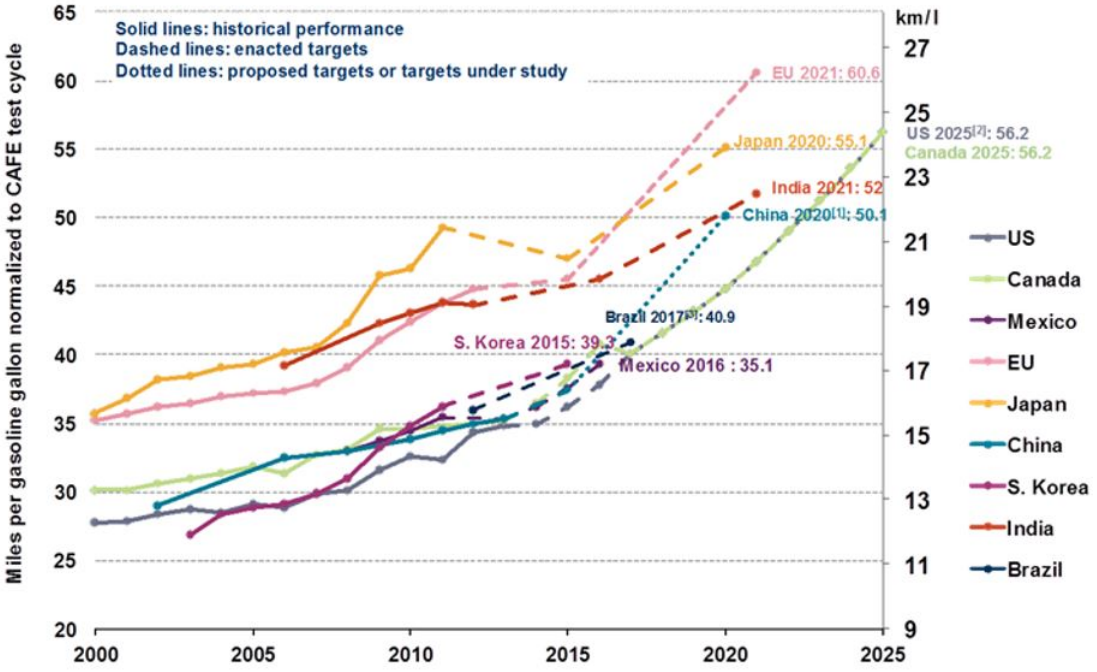

Figure 1.2: 2025 Corporate Average Fuel Economy (CAFE) regulations on fuel consupmtion for vehicles. The data is from [1].

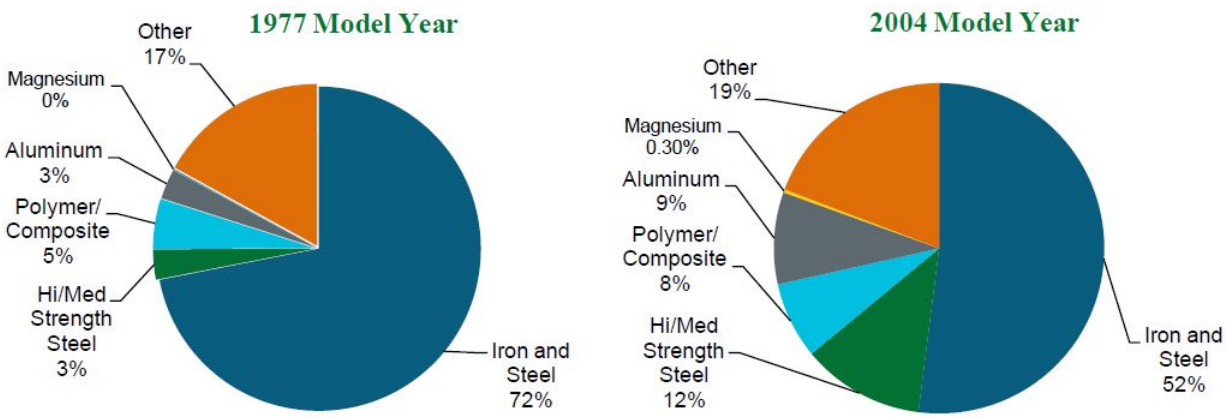

Figure 1.3: Distribution of Weight of Materials in Typical Family Vehicle. The data is from [2].

damping, machinability, good casting, high thermal conductivity, high dimensional stability, and low toxicity in humans which make it more interesting for a wide range of such as automotive, aerospace, and electronics [4, 23, 24, 25, 26, 27]. Because of these properties, automotive makers have focused on the use of magnesium alloys in vehicle components since early 1990's. Since then magnesium parts have been utilized successfully in cars powertrains, interiors, chassis, and body parts [5, 28]. Fig 1.5 shows some current and future uses of magnesium alloys in automotive and also the required properties for each Mg alloys to be used in each of interior, powertrains, body and chassis categories. Some automotive components produced by various automotive manufacturers are presented in Figs 1.6, 1.7, 1.8, and 1.9. In addition, Mg alloys are also emerging as a promising candidate for biodegradable metallic implants in cardiovascular and musculoskeletal applications, since their mechanical properties are closer to those of bone than those of other biomedical alloys [29].

Since the beginning of this millennium, Mg alloys have made inroads into applications in various industries including automotive components and their favourable aforementioned properties accelerate their usages [23]. Lightweighting strategy using magnesium is in competition with other light structural materials, i.e., aluminum and plastics [5].

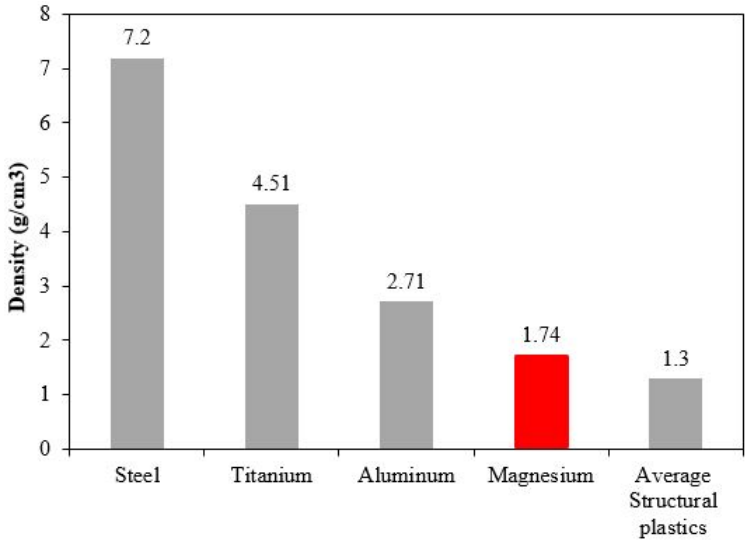

Figure 1.4: Density of magnesium versus the other structural materials.

The full potential of Mg as a structural material has not been revealed yet because of some obstacles and issues on the way. From a material engineering point of view, magnesium alloys are still suffering from poor strength, ductility, wear, corrosion resistance etc. [23, 30, 31]. There is a need for a fundamental understanding of the impacts of second phases, surface structure and texture on corrosion rate. Also, another barrier to greater implementation of Mg alloys is their low corrosion resistance [2, 32]. In addition, there are rare research works on studying tribological behaviour of Mg alloys. In some applications such as steering wheels in which the component is under wear situation or metallic implants in which tribocorrosion properties are important [33], there is a demand to enhance wear, erosion and other tribological properties of Mg alloys.

1.2 Objectives and Outline

One of the most popular Mg alloys that are used in automotive industry is the group of Mg-Al alloys. The group alloys have high strength and corrosion resistance and could be available in both cast and wrought forms. However, to expand their utilization in the industry, their corrosion and wear resistance need to be improved.

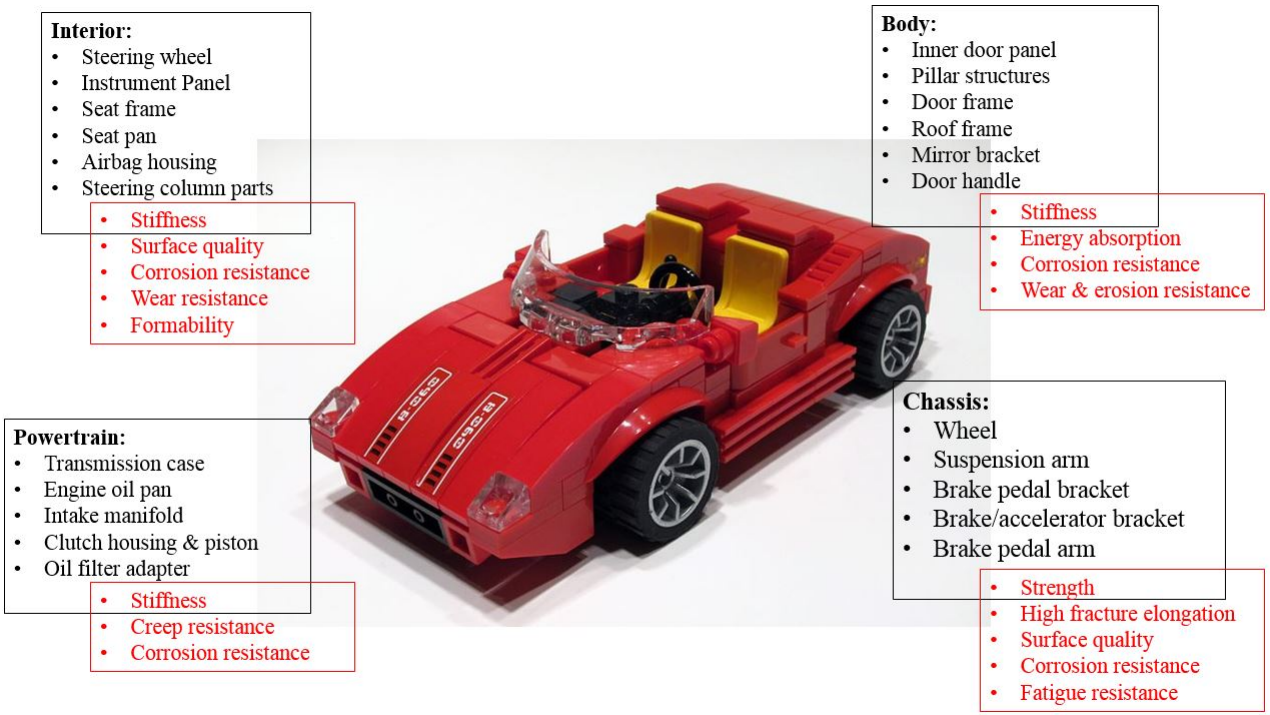

Figure 1.5: Golbal magnesium alloys applications in vehicles and essential demands on future magnesium alloys components [3, 4]. Image is reprinted from https://www.flickr.com/photos/45376442@N03/5501057607/.

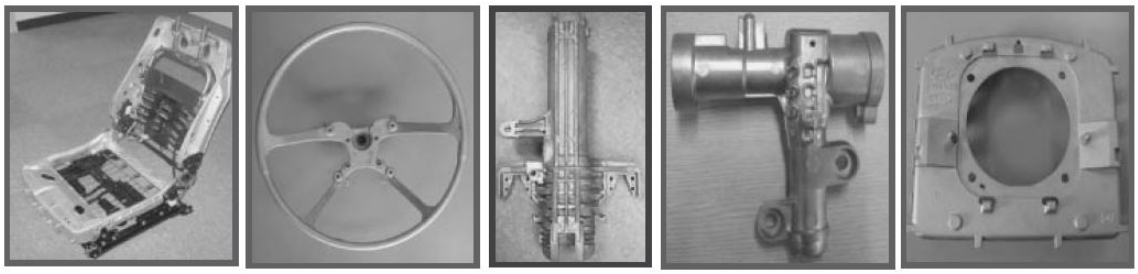

Figure 1.6: Magnesium interior parts used in Hyundai and Kia Motors Corporation. From left to right: Seat frame, steering wheel core, steering column housing, lock body, and driver air-bag housing. The utilization was reported by Kim and Han [5].

Figure 1.7: Alfa Romeo Meridian-MPI seat frame made from AM60 magnesium alloy. The utilization was reported by Kainer [6].

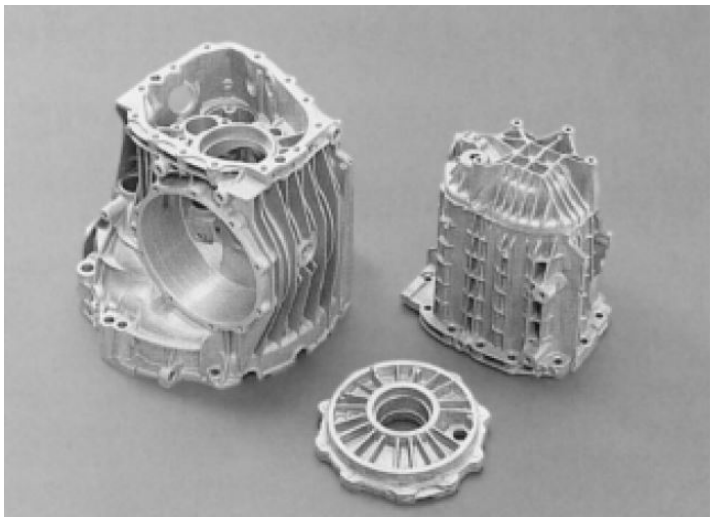

Figure 1.8: Volkswagen gearbox housing made from AZ91D magnesium alloy. The utilization was reported by Kainer [6].

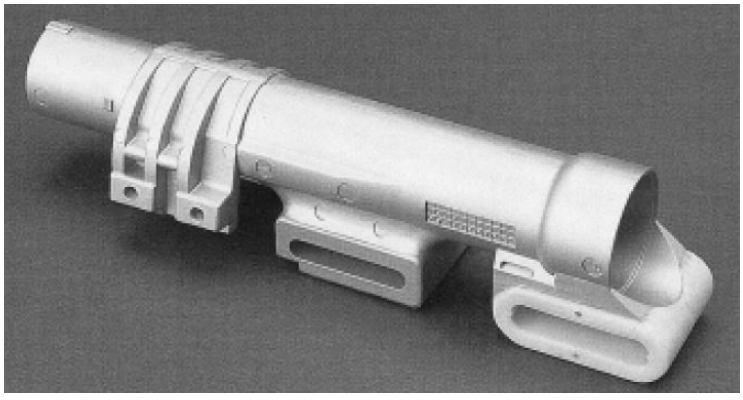

Figure 1.9: Audi/Zitzmann steering column holder and bracket made from AZ91D magnesium alloy. The utilization was reported by Kainer [6].

There have been plenty of efforts by researchers to improve the corrosion resistance of Mg-Al alloys. Some people have tried addition of rare-earth (RE) elements to the alloys to improve their corrosion properties. However, the results reported by the researchers are not always consistent and the effect of rare earth elements on the corrosion properties of Mg-Al alloys is not fully clear yet. Some other people have used surface treatment techniques such as pack cementation to improve the corrosion properties but there is still a need to find more effective, efficient, and industrially applicable surface treatment techniques.

On the other side, there are very limited research works about the tribological properties and wear resistance of Mg-Al alloys and there is a large room for research in this field. Addition of rare earth elements may enhance wear resistance of the alloys but this needs to be proved by experiments and the possible supporting mechanisms need to be identified. Also, surface treatment techniques, e.g., pack cementation treatment could be beneficial to Mg-Al alloys under friction conditions.

As its objective, this thesis is trying to answer the following questions:

1. What are the effects of rare earth addition on corrosion properties of Mg-Al alloys? What mechanisms are responsible for those effects?

2. Are rare earth elements beneficial to the wear resistance of Mg-Al alloys? If so, what is/are the mechanism(s) for the improvement?

3. How do Mg-Al alloys behave when they encounter simultaneous corrosion and wear (synergy of corrosion and wear)? Do rare earth elements make them better in that situation?

4. How do rare earth elements affect properties of the protective surface film formed on the Mg-Al alloys?

5. Can pack cementation treatment be used effectively to improve wear and corrosion resistance of Mg-Al alloys?

This thesis consists of eight chapters focusing on addressing the above-mentioned questions. After this chapter which states the motivation and objectives of the research, a literature review is given in chapter two which presents relevant fundamentals about the corrosion mechanism of Mg and its alloys, galvanic corrosion and the effects of second phase. It also provides information on current studies on the structure of the surface oxide film on magnesium alloys. Wear mechanisms for magnesium and its alloys are also discussed in chapter 2.

Chapter 3 reports a study on beneficial effects of yttrium, one of the most popular rare earth elements, on wear and corrosion properties of Mg-3%Al alloy. It shows how minor Y may enhance corrosion resistance of the alloy through homogenizing the microstructure and reducing the micro-galvanic effect. It also shows how Mg-3%Al alloy could benefit from the addition of yttrium for higher resistance to wear and corrosive wear situations.

Chapter 4 reports a study on AZ31 alloy, a commercial Mg alloy used in automobile industry. In this study, AZ31 alloy is used as the base alloy and effects of yttrium on wear, corrosion and corrosive wear of this alloy are investigated. AZ31 contains 3 wt% of Al and 1 wt% of Zn and is used as a structural alloy in manufacturing vehicles. The presence of Zn results in an increase in the strength of the alloy and the AZ alloys can have high mechanical strength.

The corrosion resistance of magnesium alloys is influenced by its surface oxide film. Chapter 5 reports a study on the role that yttrium can play in affecting properties of the surface film on Mg-Al alloy. This chapter presents experimental studies on surface film using various analytical and mechanical techniques and explains how yttrium enhances the failure resistance of the surface oxide film and what is the mechanism for this improvement.

Corrosion and wear both are surface failure processes. Thus, an effective approach is to enhance surface resistance through surface modification. Chapter 6 reports results of a preliminary study on Al-Y mixture powder pack cementation of AZ31 alloy.

The study shows improvement in wear and corrosion properties of the alloy modified with surface treatment. In addition, chapter 7 introduces a novel surface treatment technique for magnesium alloys which is beneficial for both wear and corrosion properties. The technique is a combination of aluminum powder pack cementation followed by surface nanocrystallization treatment. The results of wear and corrosion testing show significant improvement in wear, corrosion and corrosive resistance of the substrate alloy.

Finally, chapter 8 summarizes the results and concludes the thesis. Additionally, it proposes some ideas for future work.

Chapter 2

Literature Review

2.1 Corrosion of magnesium and its alloys

2.1.1 General corrosion in Mg alloys

Magnesium is one of the active metals having low electrod potentials. A list of the standard single-electrode potentials or the electromotive force series is illustrated in Table 2.1. The table ranks the metals in respect to their inherent reactivity and tendency to corrode. Those metals located at the top of the table are the most active one and contain the highest values of negative electrochemical potential. The metals at the bottom are considered as noble metals which have the greatest amount of positive electrochemical potential. As presented by the table, at room temperature magnesium has a standard electrode potential of -2.37 V_{nhe} for a piece of bare magnesium metal which is in contact with a solution containing magnesium divalent ions [7, 34, 35]. In a dilute salt solution, the corrosion potential of Mg is around -1.7 V_{nhe} (See Table 2.2). The difference between this actual corrosion potential and theoretical standard potential of magnesium is attributed to the formation of a surface film containing MgO or $Mg(OH)_2$. This surface film more or less protects magnesium from corrosion attack [9].

In order to understand corrosion of magnesium alloys, a review of dissolution of pure magnesium is helpful. In an aqueous environment, magnesium dissolves according the following overall reaction with the formation of magnesium hydroxide and

Table 2.1: The standard electromotive force (emf) serise of metals [7].

	Electrode	Electrode Reaction	Standard Electron Potential (V_{nhe})
More Active	Li, Li^+	$Li^+ + e^- \rightarrow Li$	-3.02
	K, K^+	$K^+ + e^- \rightarrow K$	-2.92
	Na, Na^+	$Na^+ + e^- \rightarrow Na$	-2.71
	Mg, Mg^{+2}	$Mg^{+2} + e^- \rightarrow Mg$	-2.37
	Al, Al^{+3}	$Al^{+3} + e^- \rightarrow Al$	-1.66
	Zn, Zn^{+2}	$Zn^{+2} + e^- \rightarrow Zn$	-0.76
	Cr, Cr^{+3}	$Cr^{+3} + e^- \rightarrow Cr$	-0.74
	Fe, Fe^{+2}	$Fe^{+2} + e^- \rightarrow Fe$	-0.44
	Co, Co^{+2}	$Co^{+2} + e^- \rightarrow Co$	-0.28
	Ni, Ni^{+2}	$Ni^{+2} + e^- \rightarrow Ni$	-0.25
	Sn, Sn^{+2}	$Sn^{+2} + e^- \rightarrow Sn$	-0.14
	Pb, Pb^{+2}	$Pb^{+2} + e^- \rightarrow Pb$	-0.13
	H_2, H^+	$2H^+ + e^- \rightarrow H_2$	0.00
	Cu, Cu^{+2}	$Cu^{+2} + e^- \rightarrow Cu$	0.34
	Ag, Ag^+	$Ag^+ + e^- \rightarrow Ag$	0.80
	Pt, Pt^{+2}	$Pt^{+2} + e^- \rightarrow Pt$	1.20
More Noble	Au, Au^{+3}	$Au^{+3} + e^- \rightarrow Au$	1.42

Table 2.2: Corrosion potential of some metals and engineering alloys in 3-6% NaCl solution. [7].

Metal or Alloy	Corrosion Potential (V_{nhe})
Mg	-1.73
Mg alloys	-1.67
Zn	-1.05
Al (99.99%)	-0.85
Al 12% Si	-0.83
Mild steel	-0.78
Cast iron	-0.73
Sn	-0.50
Stainless steel 316 (active state)	-0.43
Cu	-0.22
Ni	-0.14
Stainless steel 316 (passive state)	-0.13
Ag	-0.05
Au	0.18

hydrogen [9, 35]:

$$Mg + 2H_2O \rightarrow Mg(OH)_2 + H_2 \uparrow \tag{2.1}$$

The overall reaction could include the following partial reactions [9, 36]:

$$\text{Anodic reaction:} Mg \rightarrow Mg^{+2} + 2e^- \tag{2.2}$$

$$\text{Cathodic reaction:} 2H_2O + 2e^- \rightarrow H_2 + 2OH^- \tag{2.3}$$

$$\text{Product formation:} Mg^{+2} + 2OH^- \rightarrow Mg(OH)_2 \tag{2.4}$$

The reduction process of hydrogen ions and the hydrogen overvoltage of the cathodic phase is of significant importance to corrosion of magnesium. Corrosion can proceed quickly if sites for hydrogen discharge are easily available [9, 35]. In the case of magnesium alloys, the overall corrosion reaction seems to be similar to pure magnesium. For example, Song et al. claimed that during dissolution of Mg-Al-Zn alloys, Mg was still the main component dissolved into solution [9].

2.1.2 Galvanic corrosion in Mg alloys

Due to its low standard potential (-2.37 V_{nhe}, see Table 2.1), magnesium is very reactive and consequently very susceptible to anodic reaction to a great number of engineering metals and alloys. Cathodes can also be internal as second phases or impurities which have more noble corrosion potential compared to the magnesium matrix. In the other words, there are two forms of galvanic corrosion happening in magnesium:

1. Macrogalvanic Corrosion: Galvanic corrosion due to external contact of magnesium or magnesium alloys with other alloys

2. Microgalvanic Corrosion: Galvanic corrosion due to presence of more cathodic phases or impurities in magnesium alloy

Fig 2.1 illustrates these two types of corrosion, schematically. In both types, the anodic reaction is reaction (2.2) which is divalent corrosion of magnesium. The cathodic reaction which is hydrogen ion reduction (reaction (2.3)) happens on the surface of more noble alloy or the surface of more noble phase. The degree to which magnesium is vulnerable to galvanic corrosion is predicted by considering the relative position of two metals in emf series (Table 2.1) and the open circuit potential (OCP) of every phase in the considered solution and testing conditions [8, 37]. Another factor that affects the galvanic corrosion is hydrogen over-potential on the cathode site. Some metals, such as iron, nickel, and copper could perform more efficiently in accepting and reducing hydrogen ions. This makes them have lower hydrogen over-potentials and consequently, promotes more severe galvanic corrosion of magnesium. On the other hand, aluminum, zinc, tin, and some other metals have higher hydrogen over-potentials and are less effective in hydrogen evolution on the their surface. Therefore, they provoke less severe corrosion of magnesium [8, 9, 37, 38]. Fig 2.2 was obtained from coupling AZ91D magnesium alloy with various dissimilar alloys in salt spray which is helpful in understanding of the relative sensitivity of galvanic corrosion of magnesium alloys [8].

Generally galvanic corrosion of magnesium alloys could be associated with some basic causes like inappropriate design and assembly of parts or poor quality of alloy and presence of contaminations. Then this type of corrosion could be prohibited by choosing compatible alloys, insulating materials, making microstructure more homogeneous, utilizing high-purity alloys, and employing fluxless protection techniques during melting of the alloy [8].

Corrosion of magnesium can be acelerated by presence of some elements which are detrimental to the corrosion resistance of magnesium and its alloys. The detri-

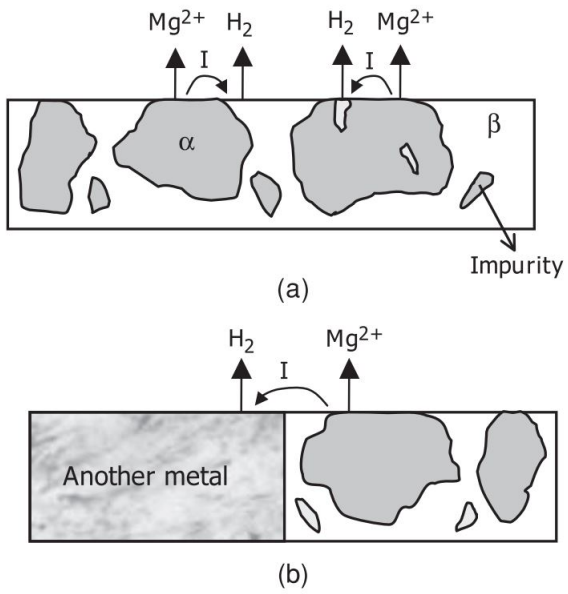

Figure 2.1: (a) Microgalvanic corrosion in magnesium alloys and (b) Macrogalvanic corrosion in magnesium alloys. The schematic was proposed by Gupta [7].

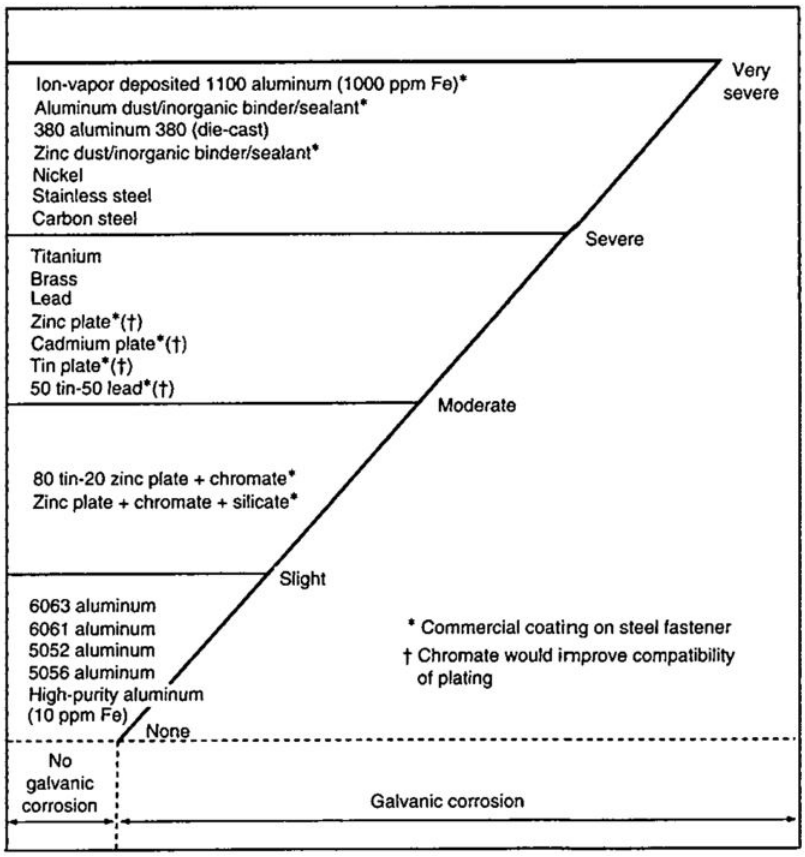

Figure 2.2: (a) An illustration for relative galvanic corrosion of AZ91D Mg alloy coupled with various other metals in salt spray environment. The data was proposed by Ghali [8].

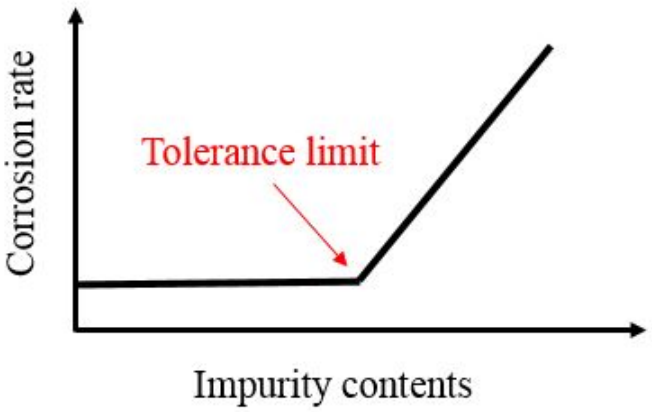

Figure 2.3: A general curve illustrating the effect of impurities concentration on corrosion rate of magnesium alloys.

mental elements are considred as impurities and are mostly those with low hydrogen over-potential. Each impurity has a tolerance limit and when the concentration of the impurity in magnesium alloys is lower than its tolerance limit (See Fig 2.3), the corrosion rate is low, whereas exceeding the tolerance limit raises the corrosion rate of magnesium alloys significantly. The tolerance limit for an impurity depends on some other factors including the manufacturing method, corrosion environment and presence of other elements. The mechanism for the tolerance limit could be rationalized by solubility of elements in magnesium. Exceeding the tolerance limit for each impurity may lead it to segregate and serve as active cathodic sites for galvanic corrosion of the matrix magnesium. Among the impurity elements, Fe, Ni, and Cu have the most detrimental effect [9, 35, 36]. Figure 2.4 presents the effect of concentration of Fe, Ni, and Cu on salt spray corrosion rate of AZ91 die cast alloy. For comparison, the corrosion performance of cold rolled carbon steel and aluminum 380 die cast alloy have been superimposed in the plot. The plot clearly shows that if the concentration of those noble impurities are lower than their tolerance limit, the corrosion performance of AZ91 is superior to the other two alloys [10].

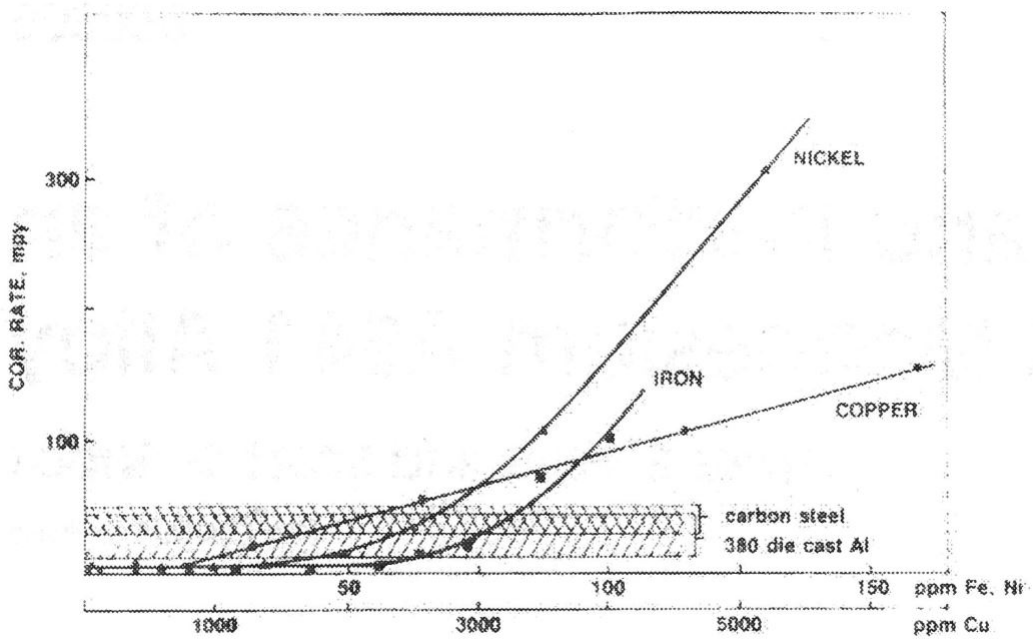

Figure 2.4: Effect of noble impurities concentrations on salt spray corrosion rate of AZ91 die cast alloy. The data was proposed by Hillis and Shook [10].

2.2 Oxide film on surface of Mg

As explained earlier, magnesium is an electrochemically active metal which reacts easily with its surrounding environment. In natural environments with low humidity, reaction of Mg with oxygen produces a stable MgO film or one consisting of MgO with minor hydrated fraction.

Pilling and Bedworth proposed a relationship between the molar volumes of a metal and its oxide and the resistance of the metal to oxidation. It is believed that the stress in an oxide scale is strongly influenced by the molar volumes of both metal and the oxide film which formed on the surface and also by the crystal structures of both metal and oxide film. According to Pilling and Bedworth, the volume change due to formation of an oxide layer on top of a metal can be expressed as:

$$R_{PB} = \frac{Volume \quad of \quad oxide}{Volume \quad of \quad metal} = \frac{Wd}{nDw} \tag{2.5}$$

Where W and w are the molecular weights of the oxide and its metal, respectively, and D and d are the densities of the oxide and its metal, respectively, and n is the number of metal atoms in its oxide molecule. For magnesium oxide (MgO) n is equal to 1.

Generally, it is believed that when R_{PB} is much greater than unity, large compressive stresses develop in the oxide scale and produce a poor oxidation resistance, cracking and spalling in the film. On the other hand, if R_{PB} is smaller than 1, tensile stress develop in the film and the insufficient oxide is available on the surface to cover the metal underneath [8, 39]. For magnesium oxide (MgO), the Pilling-Bedworth ratio of Mg is about 0.81, which supports the idea that the oxide film on the surface of magnesium is not fully protective [12, 40]. However, the surface film is still, to a certain degree, protective against corrosion in low-humidity environments.

The presence of humidity will threaten the substrate by affecting the protective film. The MgO film is permeable to water and soluble Mg species. The Pilling-Bedworth ratio for magnesium hydroxide ($Mg(OH)_2$) is about 1.77. Since there is a fairly large difference between this value and 1, the formation of ($Mg(OH)_2$) inside the oxide layer may lead to the development of cracks in the film and less protective capability of the film [8, 39].

In papers published by Nordlien and his colleagues [11, 41, 42, 43] an extensive TEM study on mictrostructure on oxide film on Mg was conducted. According to their results, when Mg was exposed to humid air, the surface hydrated and formed a thicker film with a duplex feature. The outer layer is similar to the film formed in dry air but the inner layer formed close to the metal is a hydrated layer. This new hydrated layer reduces passivity of the metal surface by allowing Mg dissolution. Immersion in water leads to the formation of a third layer on the outermost surface. This third layer has a platelet-like morphology which probably grows by precipitation of Mg^{2+} or other soluble Mg species that migrate outward from the innermost layer. Fig 2.5 shows a schematic morphology of the three-layered film formed by immersion

of Mg in water. Other people reported a two-layer structure containing hydroxide at outer and oxide at inner upon exposure to DI water. Unocic et. al. [12] conducted a transmission electron microscopy (TEM) study of aqueous film formation on ultra high purity Mg, AZ31B Mg-Al and E717 Mg-Zn alloys after exposing them to room temperature DI water for 4, 24, and 48 hours and observed a two-layered structure for the surface film (Fig 2.6). In another TEM study by Taheri et. al. [13], after immersion of pure magnesium in water for 48 hours, a two-layered structure of film was observed. A less-porous relatively thick (∼700 nm) $Mg(OH)_2$-rich outer layer resides on top of a more porous nano-crystalline thinner (50-100 nm) MgO-rich inner layer (Fig 2.7). Those different observations by different researchers may result from different testing and exposure conditions. Nevertheless, findings by other people [14, 44] propose that increasing the immersion time results in a thicker surface film and this thickening seems to be mainly produced by $Mg(OH)_2$ as illustrated in Fig 2.8 [14].

Alloying Mg with some elements affects the surface film with improved passivation capability [45]. In the case of Mg-Al alloys, their surface films are usually mixtures of magnesium and aluminum oxides [11, 35, 46, 47, 48]. Table 2.3 presents the results of an elelemental composition study by Feliu et. al. [21] of the surfaces of pure Mg and AZ31 alloy obtained by XPS after leaving samples in humidity chamber for one day. The presence of Al reduces the amounts of MgO and $Mg(OH)_2$ [49] and the surface film is enriched by aluminum oxide. This thickens the oxide film [50] with increased chemical stability of the film [21]. It is believed that the improvement in corrosion resistance of Mg-Al alloys could be attributed to the alumina component in the surface film which becomes the dominant factor in improving the passivity of the film [21]. However, the mechanism is still not well clarified.

The degree of protection provided by the natural oxide surface film is crucial to the surface stability of magnesium [14, 21, 51, 52]. Therefore, one approach for enhancing the corrosion resistance of magnesium alloys is to improve properties of the surface

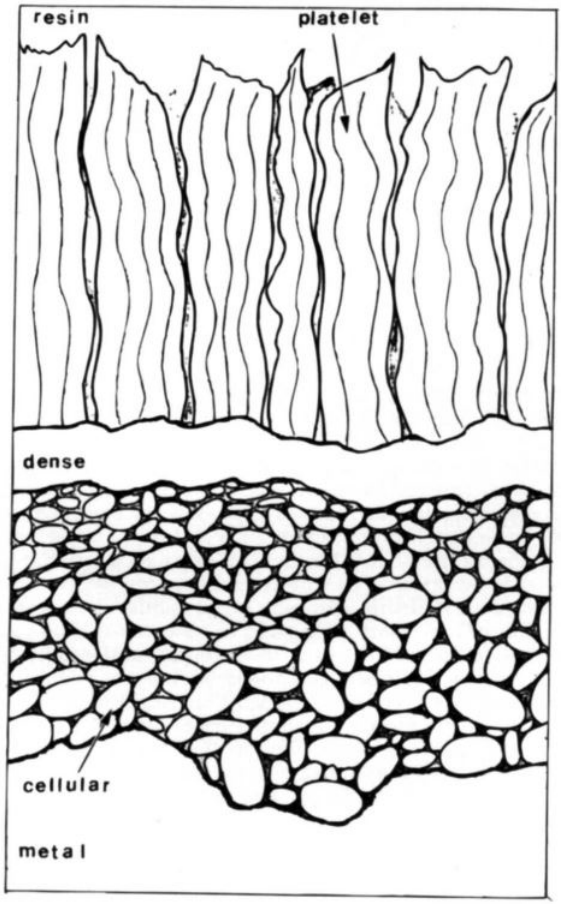

Figure 2.5: Three-layered structure film formed by immersion of Mg in water. The model was proposed by Nordlien and others [11].

Table 2.3: Chemical composition of the surfaces of pure Mg and AZ31 alloy after exposing to humid environment for one day[21].

Sample	O content (%)	Al content (%)	Mg content(%)	Al/(Mg+Al)× 100
Pure Mg	56	0	20	0
AZ31	52	2	21	9

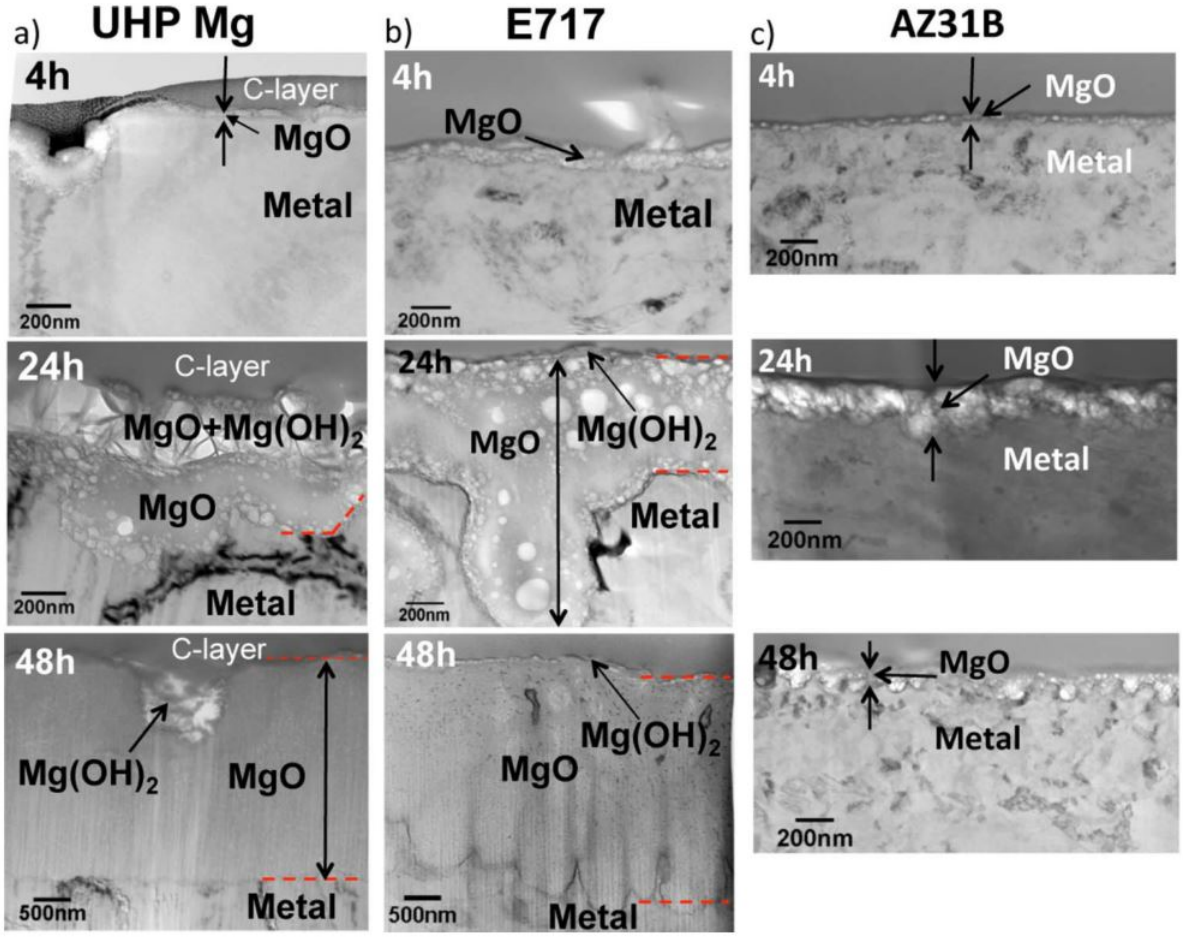

Figure 2.6: TEM film cross-sections captured by Unocic et. al. from a) UHP Mg, b) AZ31B, and c) E717 after exposure for 4, 24, and 48 h in DI water. The mcrographs were obtained by Unocic and others [12].

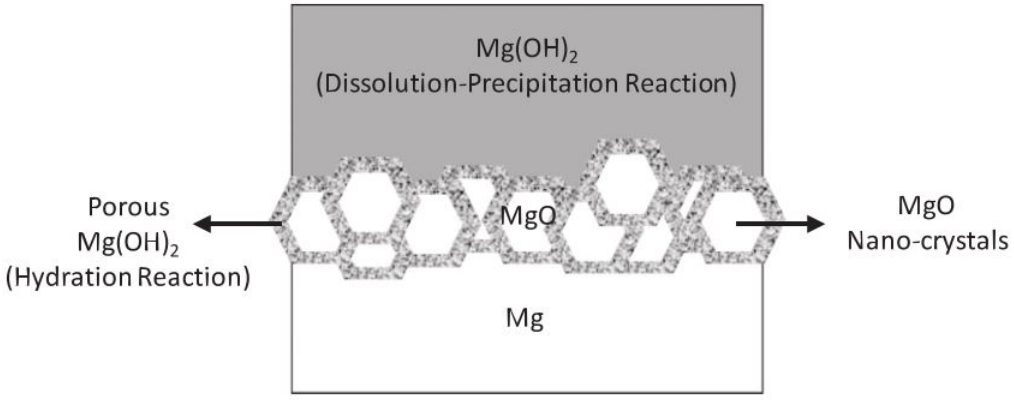

Figure 2.7: A schematic of the bi-layer structure propsed by Taheri et. al. for the surface film formed on pure Mg after immersion in water for 48 h. The schematic was proposed by Taheri et al. [13].

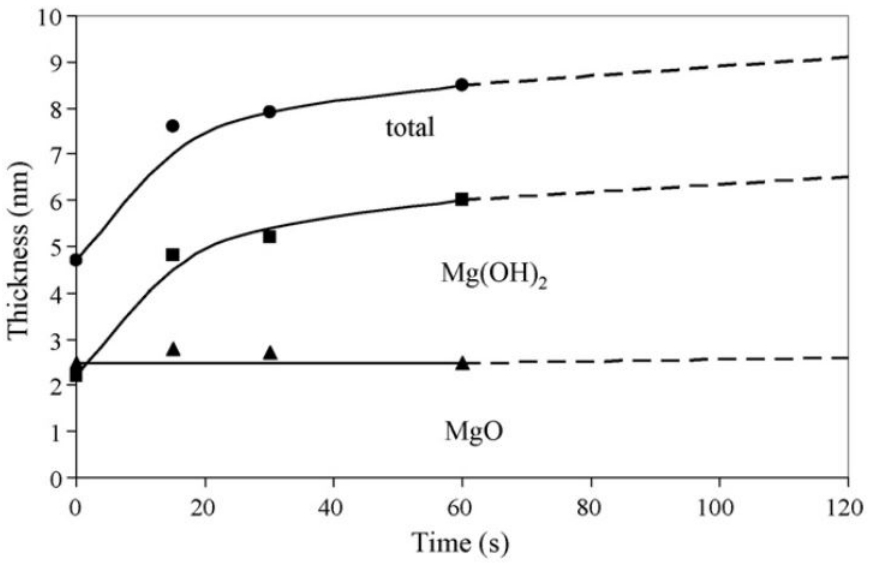

Figure 2.8: Detreminded thicknesses by XPS for surface oxide and hydroxide layer on magnesium as function of immersion time in pure water. The data was proposed by Santamaria et al. [14].

oxide films.

Rare-earth elements have demonstrated their effectiveness in improving passive films for many industrial alloys. The elements include about one-seventh of the periodic table and cover the Group IIIB elements scandium, yttrium, plus the lanthanide elements (lanthanum, cerium, praseodymium, neodymium, promethium, samarium, europium, gadolinium, terbium, dysprosium, holmium, erbium, thulium, ytterbium, and lutetium). Some researchers and engineers use the term rare earth elements only for the 15 lanthanide elements and do not consider scandium and yttrium as rare elements but the more general definition includes all of these elements as rare earth elements [53].

Rare-earth elements are very similar in their chemical properties and by that reason, they can be considered as one element. Many of their applications are based on their chemical properties and because of their similar properties, they have many similar applications. On the other hand, they have very different physical properties. For example, the melting points of the lanthanide elements vary by a factor of almost

two between lanthanum (918 °C) and lutetium (1663 °C). This difference is much larger than that found in many of the groups of the periodic table [53].

Rare-earth elements are very reactive metals, especially when they are exposed to normal atmospheric gases. The light trivalent lanthanides will oxidize upon exposure to air at room temperature and, therefore, should be stored in vacuum or under helium or argon in sealed containers. The heavy lanthanides, and scandium (Sc) and yttrium (Y) do not oxidize at room temperature; they form a protective oxide coating just as aluminum, which prevents them from oxidation. The great chemical reactivity of rare earth elements is due to the large negative free energy of formation of their oxides. This chemical reactivity is responsible for application of rare-earth metals in reducing corrosion of other metals and alloys. As explained, these elements are extremely reactive elements and form stable oxides, sulfides, hydrides, and other compounds. Thus they are difficult to prepare in a high-purity form without a great deal of effort and cost [53].

The rare earth elements are large elements so they cannot readily dissolve in solid state of the most metals. They form extensive solid solutions with each other and with zirconium and thorium. They also form extensive solid solutions in silver and gold, but these two metals do not dissolve to any extent in rare-earth elements. Rare-earth elements are considerably more electropositive than most elements and therefore they have a tendency to form compounds with the other metals [53].

Yttrium benefits mechanical properties and chemical stability of surface films on aluminum alloys [16], aluminized 1045 steel [54], 304 stainless steel [55] and Stellite 21 [15, 56]. The mechanism behind the improvement in properties of the surface film by addition of rare-earth elements is increasing the adherence of the passive films to the substrate and modifying structure and properties of the films. Fig 2.9 shows two examples of how addition of yttrium improves scratch resistance of the surface films in Stellite 21 and aluminum 6061 alloy.

Research on the effects of rare-earth elements on the surface film of Mg alloys is

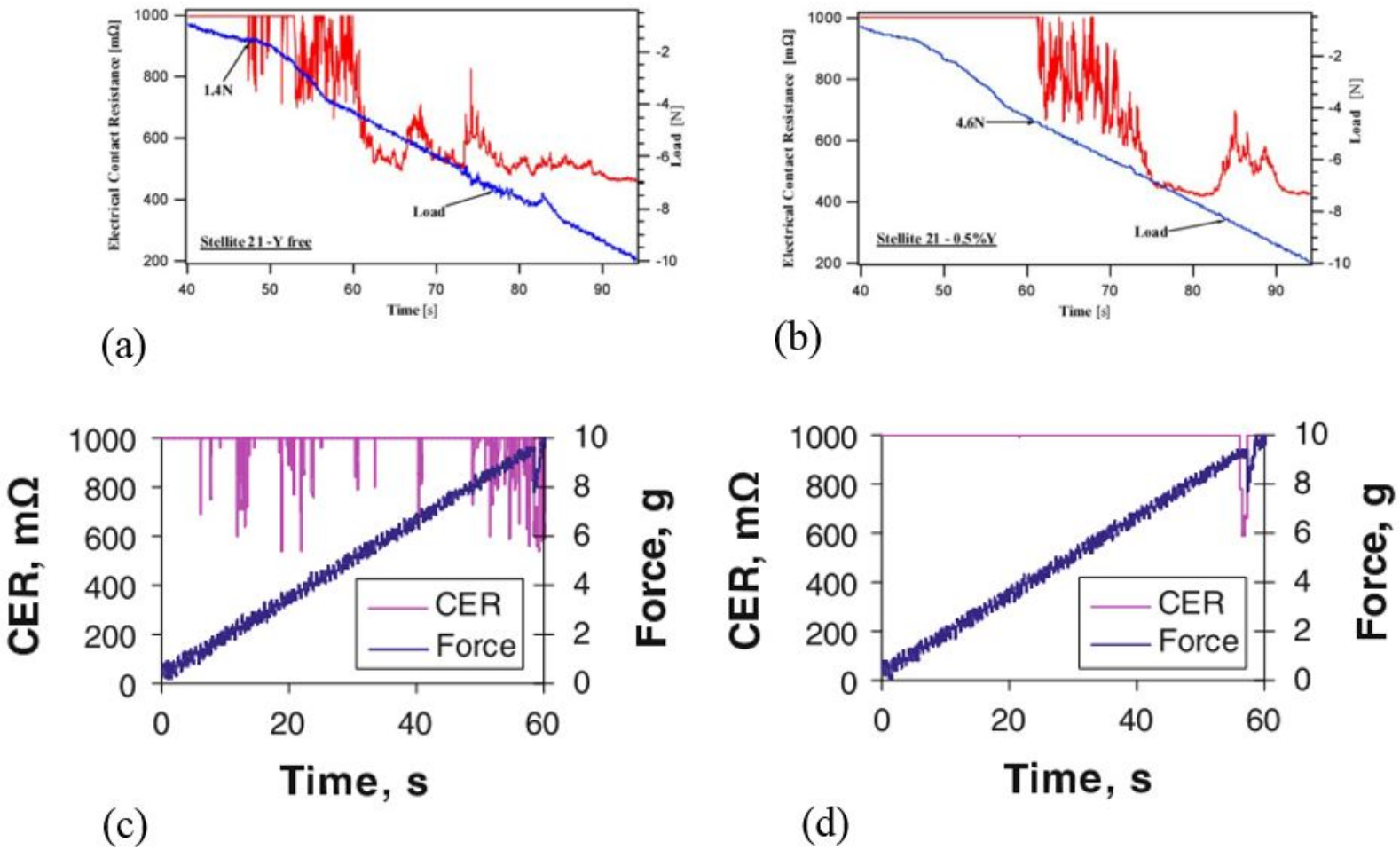

Figure 2.9: Micro-scratch test with in-situ monitoring changes in electric contact resistance for (a) Stellite-0%Y; (b) Stellite-0.5%Y; (c) Aluminum 6016-0%Y; and (d) Aluminum 6016-1.5%Y according to Dongyang Li's research group works [15, 16].

rather limited, although relevant studies can be found in the literature [31, 43, 57, 58, 59, 60, 61, 62, 63, 64, 65, 66]. Jie-xin et al. showed that addition of strontium and rare-earth elements decreases the corrosion rate in AZ91D alloy. According to their observations addition of aforementioned alloying elements results in a thinner oxide film on the surface. In addition, they reported a higher concentration for aluminum on the surface of the alloyed AZ91D samples [59]. Nordlien et. al. also reported that addition of rare-earth elements to Mg-Al alloys improved the passive properties of the passive film formed in water. They claimed a better distribution of aluminum oxide on the surface by adding rare-earth to the alloy. They also claimed a significant reduction in film hydration from the presence of RE elements although no rare-earth element was detected in the film itself [43].

The above reported studies are mainly focused on the influence of rare-earth elements on the overall oxidization and corrosion behavior with little attention given to the role that the rare-earths plays in affecting properties of the oxide film itself.

2.3 Wear mechanisms in magnesium and its alloys

Wear is defined as the removal of material from the surfaces of solids as a result of relative mechanical motion at the surface. The mechanical motion is made by the action of contacting solid, liquid, or gas. Wear is generally undesirable since it causes progressive loss of material from the primary surface, and also results in high costs for components repair and replacement parts. Wear is of particular significance to mining, agriculture and transportation industries [18, 67].

The major modes of wear are abrasive wear, adhesive wear, erosive wear, fretting and corrosive wear. It is estimated that half of all wear failures are caused by abrasive wear, about 15% by adhesive wear, and the remaining by other forms of wear [67].

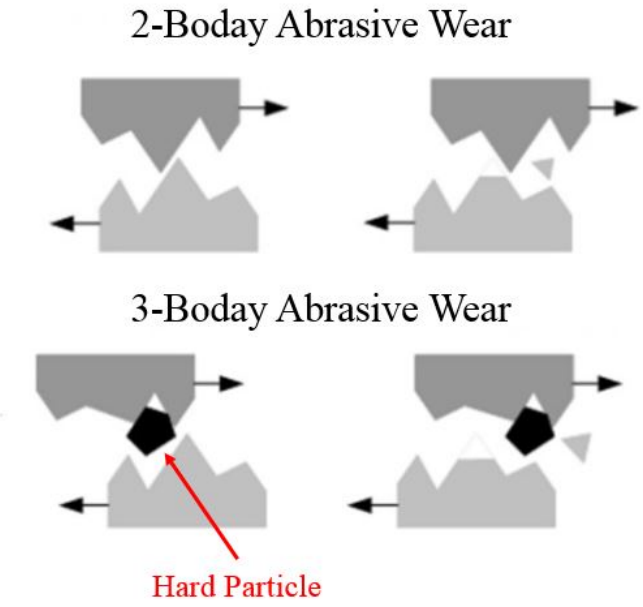

Figure 2.10: two-body and three-body abrasive wear in materials.

2.3.1 Abrasive wear

For two bodies in contact and move in opposite direction, abrasive wear is caused by plowing or cutting by asperities on two surfaces (two-body abrasion). When solid particles exist between two surfaces moving in opposite direction, the abrasion is named as three-body abrasion. Fig 2.10 illustrates these two types of abrasive wear. Approximately, the rate of wear increases linearly with increase in the normal load applied to the wear surface. The wear volume loss generally decreases with increasing hardness of the materials. To estimate the wear rate of an engineering material, Archard (1953) equation is often used which is expressed as:

$$V = K\frac{LS}{H} \tag{2.6}$$

Where:

- V: The wear volume loss
- H: Hardness of the material
- L: Normal load

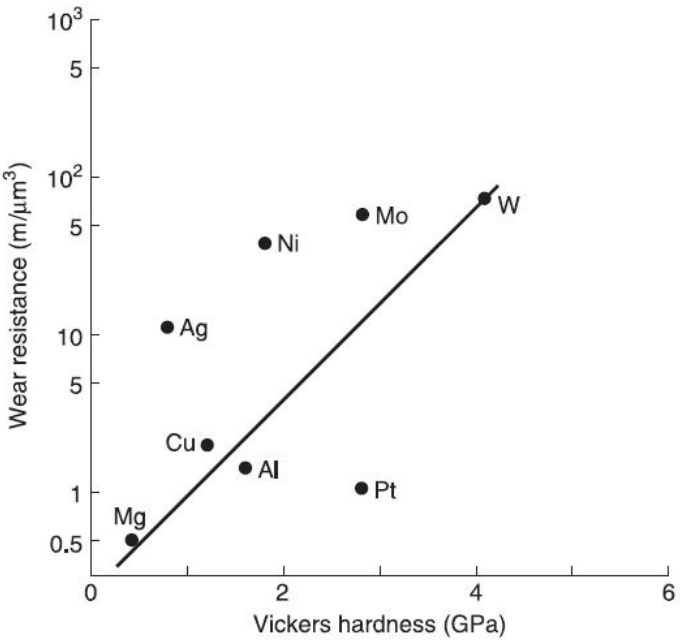

Figure 2.11: Abrasive wear resistance of pure metals under unlubricated condition as a function of Vickers hardness. The data was presented by Bhushan [17].

- S: Sliding distance, and
- K: Wear coefficient which is a dimensionless constant

Hardness is an important factor in abrasive wear and generally, when a material has a high level of hardness, it is more resistant to abrasive wear. Fig 2.11 illustrates the correlation between abrasive wear resistance of some pure metals as a function of their Vickers hardness. Pure Mg has the lowest hardness among those metals, leading to a poor resistance to abrasive wear. Because of its poor wear resistance, Mg has to be modified by alloying elements to form stronger Mg alloys.

2.3.2 Adhesive wear

During opposite sliding of two surfaces in contact, if there is a strong adhesive force between the surfaces, adhesive wear occurs. Adhesive wear involves transfer of material from the softer material to the harder one. One of the main factors in promotion of adhesive wear is compatibility of the two surface which are in contact. If the pair

	W	Mo	Cr	Co	Ni	Fe	Nb	Pt	Zr	Ti	Cu	Au	Ag	Al	Zn	Mg	Cd	Sn	Pb
In				2	3				4	3	3	4	4	1	3	4	4	4	4
Pb	2	2	1	1	1	1	1	4	4	4	1	2	3	1	1	3	3	4	
Sn	3		1	3	3	2	3	4	3	4	3	4	4	2	3	2	4		
Cd			3	3	2	2		4	4	3	3	4	4	1	4	4			
Mg		3		3	2	2	2		4	2	4	4	4	4	3				
Zn		3	4	4	4	4	2	4	2	3	4	4	4	4					
Al	4	3	4	3	4	4	4	3	3	4	4	4	4						
Ag	1	2	1	1	1	1	2	4	3	4	3	4							
Au	4	3	4	3	4	4		4	4	3	4								
Cu	2	1	1	4	4	3	2	4	4	3									
Ti	4	4	4	3	4	4	4	4	4										
Zr	3	4	3	4	3	2	4	3											
Pt	4	4	4	4	4	4	4												
Nb	4	4	4	4	4	4													
Fe	4	4	4	4	4														
Ni	4	4	4	4															
Co	4	4	4																
Cr	4	4																	
Mo	4																		

Figure 2.12: The tendencey of metallic pairs to adhere to each other. 1 represents a low tendency and thus the two metals are incompatible. 4 represents a high tendencey and thus the two metals are identical or very compatible. There is a great risk of adhesive wear for the pairs with 4 as their number. The data was proposed in Smithells Metals Reference Book [18].

have similar crystal structure and chemical properties, they tend to make solid solutions or intermetallics, leading to a larger adhesive force. Different structures of two materials in contact reduce adhesive force and thus adhesive wear. Fig 2.12 illustrates the tendency of metallic couples to adhere to each other and promote adhesive wear.

2.3.3 Corrosive wear

Corrosive wear or tribo-corrosion defines the damage that is caused by synergistic attack of corrosion and wear or wear in a corrosive environment. This type of attack occurs in various industries and may result in a notably high wear rate [18, 19] due to the fact that wear and corrosion may mutually affect each other. The material loss due to the synergy is the difference between material loss under a corrosive wear situation and that caused by each of wear and corrosion damages individually [19].

The total damage by corrosive wear may be expressed as:

$$v_t = (v_w + v_c + v_s) \tag{2.7}$$

Where:

- v_t: Total volume loss caused by corrosive wear
- v_w: Volume loss caused by wear
- v_c: Volume loss caused by corrosion, and
- v_s: Volume loss resulted by synergy of wear and corrosion

Generally, many metals and metallic alloys have a surface oxide film which more or less reduces corrosion and restricts interaction between the metal or alloy and the corrosive environment. The situation is similar to magnesium and its alloys, as explained earlier, the surface oxide film secures the alloy. When wear exists, the surface film can be peeled off from the surface, thus corrosion is accelerated. In addition, the plastic deformation introduced by wear makes the material more anodic [19].

The increase in material loss in corrosive wear may also be contributed by strained and unstrained zones which have different electrochemical potentials. These micro-electrodes could intensify corrosion by promoting micro-galvanic corrosion. Wear also muddles the corrosion environment and reduces the concentration of metallic ions in the vicinity of the worn surface. This accelerates the transfer of ions to the cathode which causes a greater rate for corrosion reaction [19].

Corrosion itself can promote wear. Corrosion worsens the surface quality of material progressively and may generate products such as porous oxides on the surface which are less strong than the original alloy. These can reduce wear resistance of the material to frictional forces. Moreover, hydrogen resulting from the corrosion

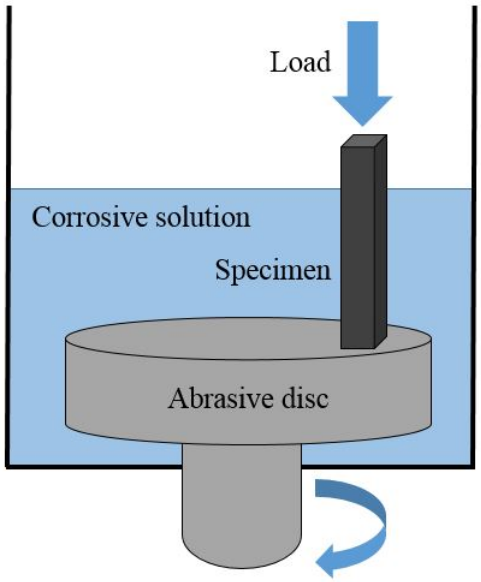

Figure 2.13: Schematice illustration of pin-on-disk corrosive wear testing.

may diffuse into the metal and result in hydrogen embrittlement phenomenon in the surface layer of the metal [19].

To evaluate the performance of a material under corrosive wear condition, it is possible to use the general wear testing systems that are used in dry condition. However, the testing environment should be the corrosive environment in which the material needs to be studied. Fig 2.13 illustrate a schematic of the pin-on-disk corrosive wear testing setup which was used for the current research [19].

Chapter 3

Improving the Performance of Mg-3%Al Alloy with Yttrium[1]

3.1 Introduction

Magnesium has attracted considerable interest from not only the transportation industry but also other technical sectors due to its low atomic weight and fair strength, which make its alloys good candidates for many applications. In addition to its mechanical strength and fatigue behaviour that are demanded for further improvement, poor wear resistance and especially low corrosion resistance of Mg alloys are also hurdles to the extensive use of Mg alloys for making a wide variety of lightweight components. Efforts have been made to improve Mg alloys by addition of other elements. Rare-earth elements (RE) are added to Mg alloys with attempts to improve their mechanical behaviour, e.g., creep resistance, and modify their corrosion resistance [68, 69, 70, 71]. If addition of REs is an effective approach for improving both mechanical properties and corrosion resistance, then these elements would help suppressing of corrosion-wear synergy and thus increase corrosive-wear resistance of magnesium alloys.

Studies reported in the literature suggest that rare-earth elements may refine the microstructure of Mg-alloys and improve their strength and creep resistance with the

[1] A version of this chapter has been published as a peer-reviewed article in Tribology International, Volume l67, 2013, Pages 154-163

formation of RE-containing second phases [68, 69, 72, 73, 74]. The positive effects of RE on the mechanical properties of Mg alloys should also benefit their wear resistance. Although reported studies are limited, such benefit has been demonstrated, e.g., by Qi et al [75] who investigated effects of RE on friction and wear. However, the effect of RE on corrosive wear of Mg alloys has not been well evaluated yet due to the fact that how RE elements affect the corrosion behaviour of Mg alloys and relevant mechanism are still not very clear.

It is known that RE can enhance the corrosion resistance of passive metallic materials through forming a more protective passive film with higher adherence to the substrate [54, 76, 77, 78]. This may not be the case for magnesium, since magnesium is an active metal and corrodes readily in some environments. However, under some circumstances, e.g., atmospheric corrosion, magnesium could be more resistant than mild steel, since magnesium oxide forms on the surface of magnesium when exposed to atmosphere at room temperature. In general, the poor corrosion resistance of many magnesium alloys could be ascribed to their low electrode potentials, internal galvanic corrosion caused by second phases or impurities, and the quasi-passive hydroxide film on magnesium which is much less stable than the passive films on passive metals such as aluminum and stainless steels. Nakatsugawa et al. [70] investigated the corrosion behavior of a few rare-earth containing magnesium alloys containing yttrium and other rare-earths and observed that rare-earth elements improved the corrosion resistance of the magnesium alloys. However, because of the above-mentioned corrosion mechanisms for corrosion of Mg alloys (i.e. anodic nature, galvanic corrosion and less stable hydroxide film), reported studies of the effect of RE on the corrosion behaviour of Mg alloys are not always consistent. The inconsistency could result from varied responses of Mg alloys to different environments or corrosive media. Kiryuu et al. [79] suggest that the improvement in corrosion behavior of Mg alloys with RE is attributed to the factor that the corrosion product is stabilized by the rare-earth elements. There could be other possible mechanisms, depending on the corrosive

Table 3.1: Compositions of Mg-Al-Y alloys made for the study.

Sample	Y content (wt%)	Al content (wt%)	Mg content(wt%)
Mg-3Al	0	3	97
Mg-3Al-0.5Y	0.5	3	96.5
Mg-3Al-1Y	1	3	96
Mg-3Al-2Y	2	3	95
Mg-3Al-3Y	3	3	94
Mg-3Al-4Y	4	3	93
Mg-3Al-5Y	5	3	92

environments, corrosion products and microstructure features of Mg alloys. Thus, clarification of the effects of RE on the corrosion behavior and wear behavior would be helpful for appropriate application of RE in Mg alloys for improved resistance to corrosion and corrosive wear.

In this study, we investigated wear, corrosion and corrosive wear behaviour of Mg-3Al alloys containing Y of different concentrations in tap water. The objective of this work is to investigate the effect of added yttrium up to 5% on hardness, wear, corrosion and corrosive wear of Mg-3Al alloy in order to clarify some unclear issues. Polarization analysis, immersion tests, pin-on-disc wear tests, macro-indentation, XRD, SEM and EDS were employed to evaluate and characterize the Y-containing Mg-3Al alloys.

3.2 Experimental Procedure

Pure Magnesium rods (99.9%), pure Aluminum granules (99.9%) and pure yttrium powder (99.9%) were melted together with different ratios in an AGI induction furnace to make alloy ingots. Ingots of seven different compositions were made and each ingot was melted at least three times in order to reduce the microstructural inhomogeneity. Table 3.1 shows compositions of the different alloys. Samples with appropriate sizes were cut from the ingots for different tests.

Microstructures of the alloys were characterized using a Vega-3 TESCAN Scanning Electron Microscope at 20Kv voltage and an EDXS oxford instrument was employed to analyze local compositions of different domains as well as to map composition

distribution (Energy Dispersive Spectroscopy). A Rikagu X-ray diffractometer with Cu Kα radiation (λ= 1:54056 A) was used to determine phases developed in the alloys.

Hardness of the alloys was measured using a hardness tester under a maximum load of 0.3 Kgf for 20 seconds. The reported hardness value for each alloy is an average of at least 6 measurements. Dry and corrosive wear sliding tests were performed at ambient temperature using a CSEM High Temperature Tribometer (pin-on-disk)in agreement with G99-05 ASTM Standard [80]. The pin used in testing was a 3 mm diameter Si_3N_4 ball and all tests were performed at a sliding speed of 1 cm/s along a circle path of 2.0 mm in diameter under a normal load of 2 N for 2000 rotations, corresponding to a sliding distance of 12.6 m. In order to keep the sample surface temperature constant during dry wear testing, an air flow was directed to the pin-sample contact area during testing. Corrosive wear tests in tap water as the corrosive medium were performed using the same pin-on-disc apparatus with an attached container. A Zeisss white light scanning confocal system was used to analyze the wear track, from which the corresponding volume loss was determined. The reported volume loss for each sample is an average of results obtained from four repeated wear tests.

The corrosion behaviour of the alloys was evaluated by performing polarization tests using an electrochemical testing apparatus (PC4-750) made by Gamry Instruments Inc. A saturated calomel electrode (SCE) was used as the reference electrode, and a platinum plate (Pt) was used as the counter electrode. The electrochemical tests were performed in tap water at room temperature. The corrosion rate and corrosion potential was determined according to Tafel extrapolation method. Each reported value is an average of at least three repeated tests. Moreover, roughness of corroded surface of samples was analyzed for helping us to understand how different contents of yttrium influence the corrosion-product surface layer. After polishing with 800 sand paper, the samples were immersed in tap water for 14 days at the room

Table 3.2: Spot Energy Dispersive Spectroscopy (EDS) analysis of Mg-3Al, Mg-3Al-1Y, Mg-3Al-3Y and Mg-3Al-5Y samples.

		Mg(at%)	Al(at%)	Y(at%)
Mg-Al	Spot 1	95.33	4.67	0
	Spot 2	70.99	29.01	0
Mg-Al-1Y	Spot 1	98.89	1.11	0
	Spot 2	52.36	30.81	16.83
Mg-Al-3Y	Spot 1	3.45	60.29	36.27
Mg-Al-5Y	Spot 1	4.75	58.40	36.84

temperature. Then the roughness of surface was analyzed using the Zeisss white light scanning confocal system.

3.3 Results and Discussion

3.3.1 Miscrostructure

Back Scattered Electron (BSE) micrographs of various alloys are shown in Fig 3.1. Fig 3.1(a) illustrates a typical microstructure of Mg-3%Al alloy without Y, which consists of the matrix and small light-grey inclusions. EDS spot analysis (Table 3.2) reveals that the matrix is Mg containing a small amount of Al. According to the binary phase diagram of Mg-3%Al [81], Al has a low solubility in Mg and $Mg_{17}Al_{12}$ phase forms when the concentration of Al exceeds its solubility in Mg. Thus, the small light-grey inclusions (e.g., spot 2 in Fig 3.1(a)) in the Mg-3%Al alloy should be the $Mg_{17}Al_{12}$ phase. X-ray diffraction analysis was made to determine what phases presented in the alloys. Fig 3.2(a) illustrates a X-ray diffraction pattern of the Mg-3%Al alloy. As shown, in addition to peaks of Mg in the spectrum, another set of peaks come from $Mg_{17}Al_{12}$.

Adding Y resulted in microstructural changes. As shown in Fig 3.1(b), with 1%Y, the alloy showed a clear matrix and fine white domains. Increasing the content of Y to 3%, the microstructure is similar but some of the white phase domains became relatively larger (Fig 3.1-c), which are mainly composed of Al and Y with an atomic

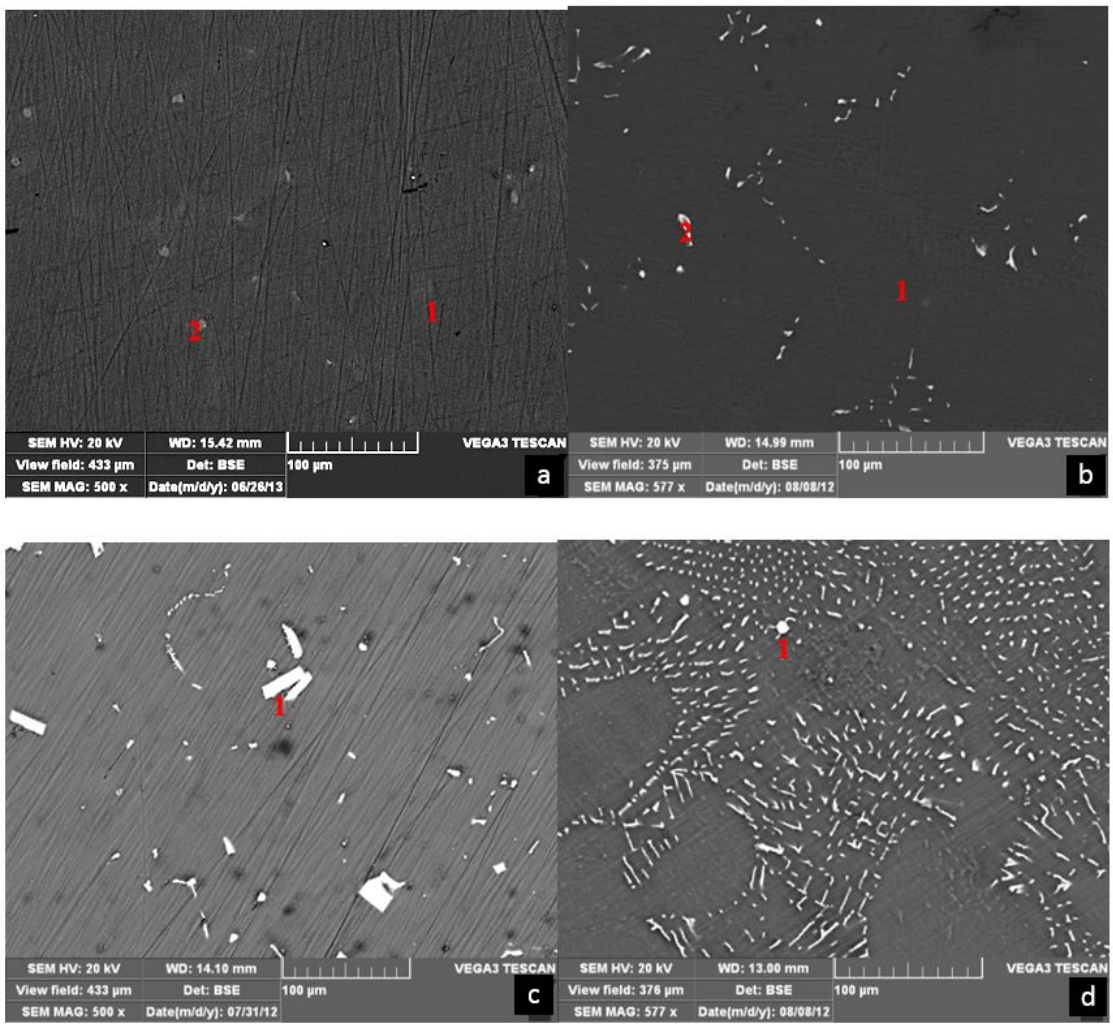

Figure 3.1: Back Scattered Electron (BSE) micrographs of: a) Mg-3%Al, b) Mg-3%Al-1%Y, c) Mg-3%Al-3%Y and d) Mg-3%Al-5%Y samples.

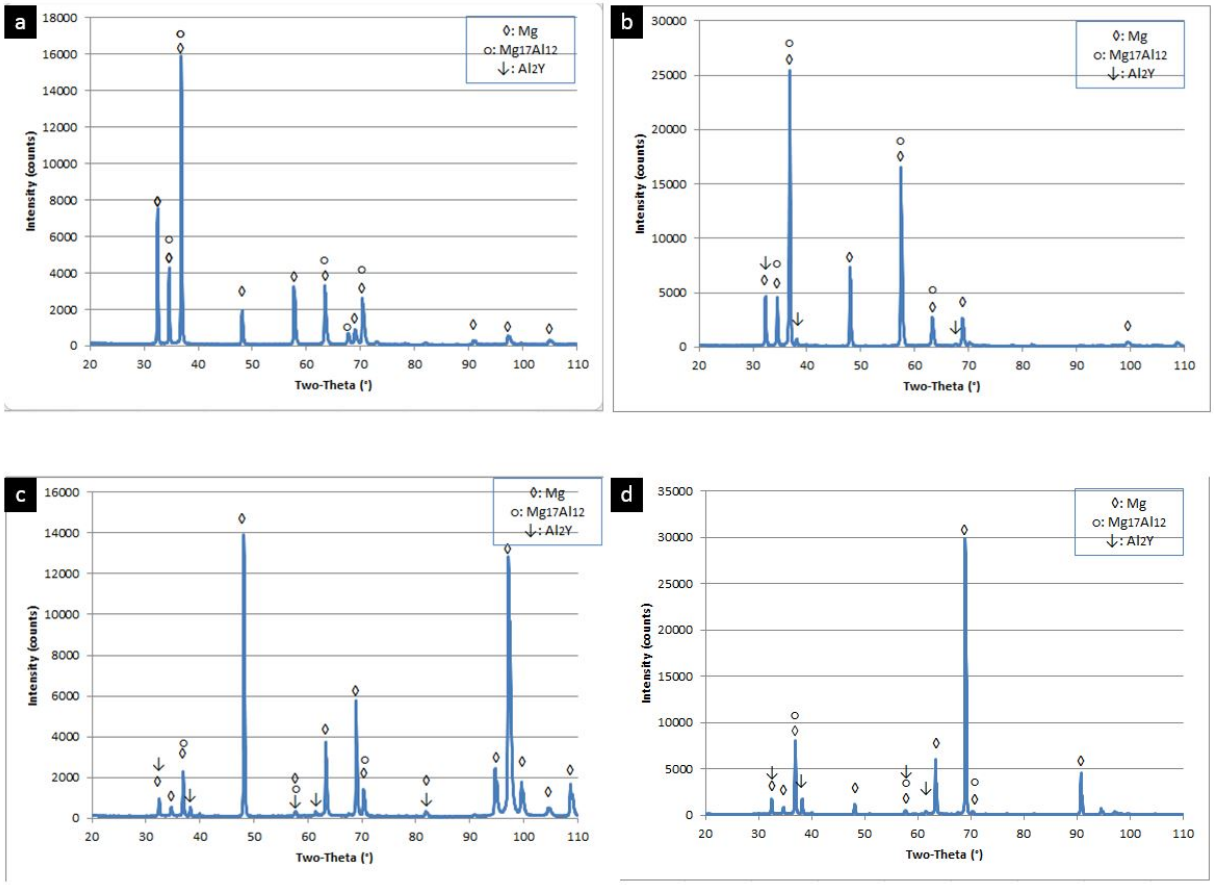

Figure 3.2: X-Ray Diffraction (XRD) analysis of: a) Mg-3%Al, b) Mg-3%Al-1%Y, c) Mg-3%Al-3%Y and d) Mg-3%Al-5%Y samples.

percent ratio approximately equal to 2:1 (see Table 3.2) and confirmed as Al_2Y by the XRD analysis. As the content of Y was further increased to 5%, the Al_2Y phase appeared mainly in the form of small needles and kept their composition unchanged as the EDS analysis indicates. The fine Al_2Y needles covered the whole area with high density (Fig 3.1-d) and there was no marked coarsening of this phase within the current composition range. Figure 3.2(b-d) illustrate XRD patterns of Mg-3Al-1Y, Mg-3%Al-3%Y and Mg-3%Al-5%Y, respectively, which show that the $Mg_{17}Al_{12}$ phase was basically eliminated by the addition of yttrium. Instead, peaks of Al_2Y are presented in XRD patterns of the alloys containing Y in addition to peaks of Mg. This type of Y-containing phase has been reported in the literature. In addition to Al_2RE [73, 82], other RE phases such as Al_3RE [83, 84] and $Al_{11}RE_3$ [74, 82, 83, 85] are also reported presenting in some Mg alloys.

The microstructure changes above imply that Y has higher affinity for Al and is able to attract Al from the Mg-Al compound and matrix. Or in other words, Al_2Y is more thermodynamically stable than $Mg_{17}Al_{12}$. It has indeed been determined that (by first-principles calculation and experimental measurement) the energy change corresponding to the formation of $Mg_{17}Al_{12}$ is in the range of -4,360 j/mol while that for the formation of Al_2Y is -52,320 j/mol (first-principles calculation) [86]. This indicates that yttrium is much more competitive to attract and react with Al from the original microstructure.

In order to determine distributions of Al and Y, compositional mapping was carried out with the Energy Dispersive Spectroscopy (EDS). Compositional maps of the alloys are illustrated in Figure 3. As shown, there are changes in the distribution of Al in samples as Y was added. In Mg-3%Al, Al is not homogeneously distributed and accumulated in some areas. As Y was added, the distribution of Al became homogeneous as Fig 3.3(b) illustrates. Yttrium is a reactive element with high affinity for Al. This could help homogenization of Al distribution accompanied with formation of dispersed fine Al_2Y phase as shown in Fig 3.1(b). The distribution of Y is also

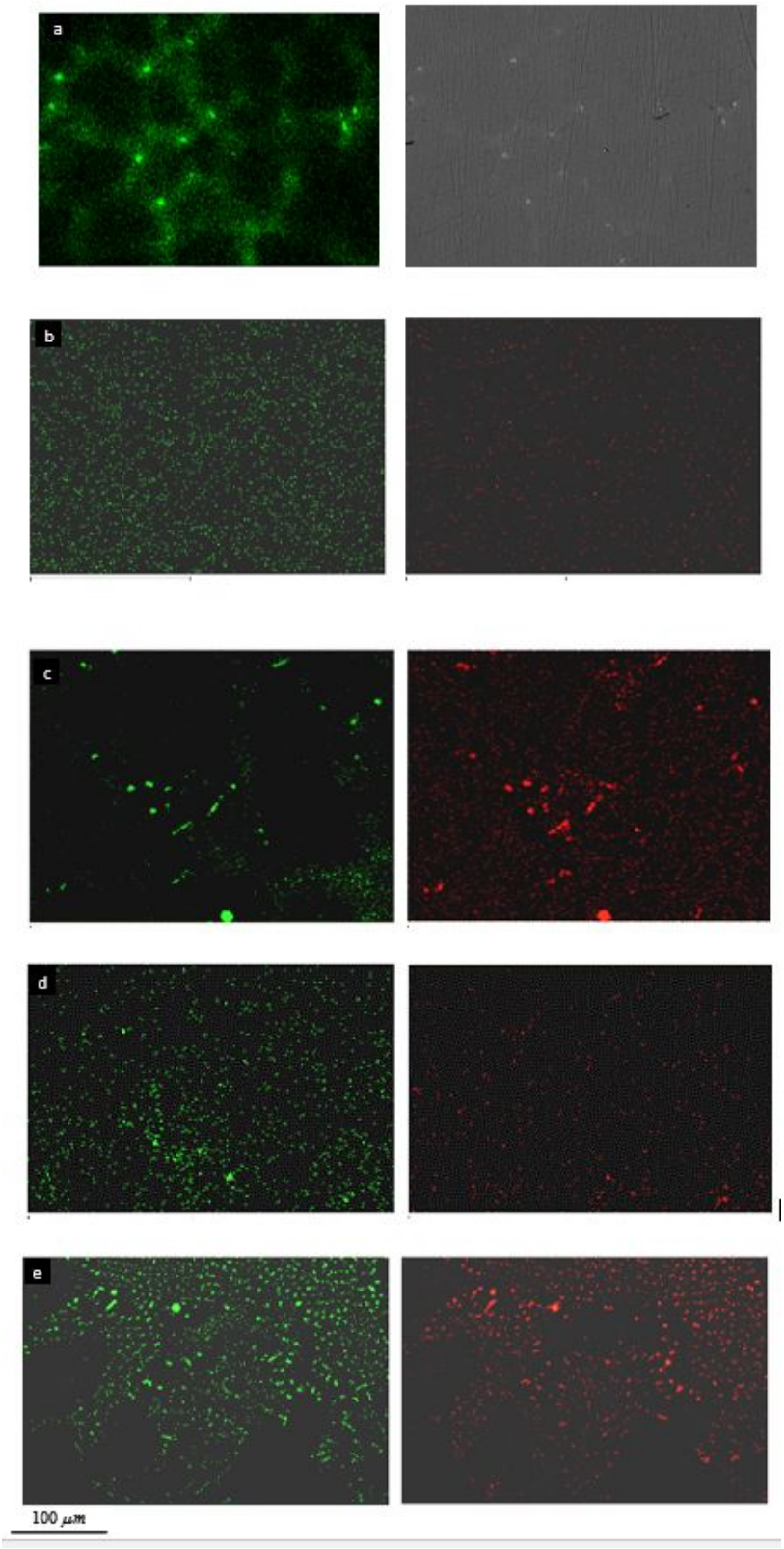

Figure 3.3: Energy Dispersive Spectroscopy (EDS) mapping of Al (green) and Y (red) in: a) Mg-3%Al, b) Mg-3%Al-0.5%Y c) Mg-3%Al-1%Y, d) Mg-3%Al-3%Y and e) Mg-3%Al-5%Y samples. Images corresponding to maps of c), d) and e) are illustrated in Fig.1 b), c) and d), respectively.

homogeneous Fig 3.1(b). The addition of RE elements may decrease the volume fraction of $Mg_{17}Al_{12}$ as well [82, 83]. As more Y was added, the Al_2Y phase grew, leading to some accumulated Al and Y areas as Fig 3.3(c) illustrates, corresponding to the morphology shown in Fig 3.1(b). However, as one may see in Fig 3.1(c) and (d), the Al_2Y phase gradually became more dispersed in the alloy when the content of Y was further increased up to 5%, which is consistent with the corresponding compositional maps shown in Fig 3.3(d) and (e).

3.3.2 Hardness and Dry Wear Resistance

Fig 3.4 shows the hardness of the Mg-Al alloy versus the content of added Y. As shown, the added yttrium made the alloy harder, which should be mainly attributed to the formation of Al_2Y phase, whose volume fraction increased with increasing Y concentration. When Y was added, the volume fraction of $Mg_{17}Al_{12}$ phase decreased and the irregular eutectic-like domains disappeared. This implies that the Al_2Y phase is more effective in strengthening the Mg-3%Al alloy than the previously present $Mg_{17}Al_{12}$ phase and the irregular eutectic-like domains. Al_2Y is harder than $Mg_{17}Al_{12}$, evidenced by micro-indentation tests. As reported in another paper [20], we measured hardness of $Mg_{17}Al_{12}$ and that of Al_2Y using a Vickers micro-hardness tester (Fisherscope H100C Microhardness Measurement System with WIN-HCU software). Result of the micro-hardness (HV0.3) testing shows that Al_2Y (460 HV) is much harder than $Mg_{17}Al_{12}$ (220 HV). The strengthening effect of RE-second phases have also been reported for other Mg alloys, e.g., AZ31 alloy [87] and Mg-2%Nd alloy [88].

Increase in hardness would consequently raise the wear resistance of the Mg alloy. Volume losses of samples with different concentrations of yttrium were measured using the pin-on-disc tester, which are presented in Fig 3.5. As shown, the volume loss caused by wear considerably decreased with increasing content of yttrium. This is consistent with the increase in hardness due to the formation of harder Al_2Y phase,

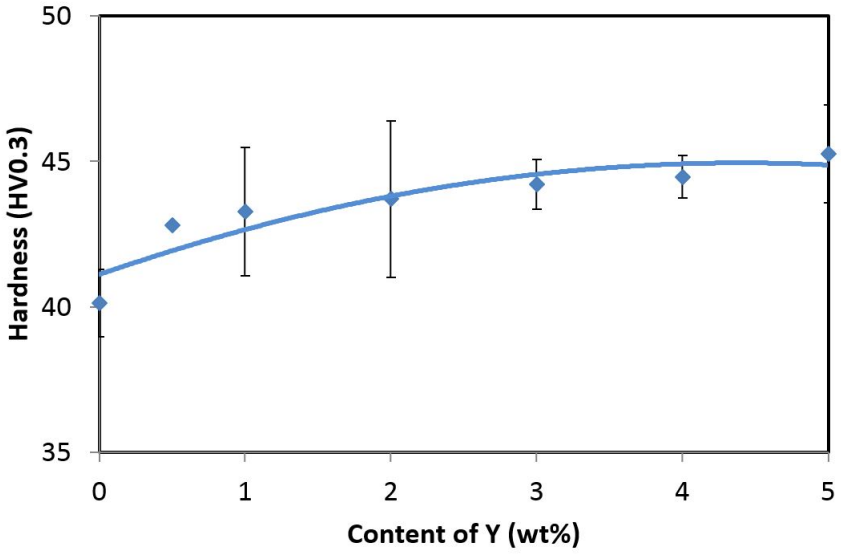

Figure 3.4: Hardness of Mg-3Al alloy versus yttrium up to 5 wt% Y, measured under a maximum load of 0.3 Kgf.

whose volume fraction increased as more yttrium was added. As shown in Fig 3.5(a), the volume loss of Mg-3%Al-5%Y is about a quarter of that of Mg-3%Al. It should be indicated that the enhanced wear resistance caused by added yttrium may also benefit from the higher thermal stability of Al_2Y phase, compared to that of $Mg_{17}Al_{12}$. As reported by Su, et al [89] $Mg_{17}Al_{12}$ phase completely dissolved during a solution heat treatment at 693 K, while Al_2Y phase has a much higher melting temperature of 1758 K. During the dry wear test, the sample surface temperature may rise, leading to material softening. The thermally stable Al_2Y phase would be much effective in resisting wear under such a testing condition. To confirm this, we performed similar wear tests with minimized surface temperature variation by blowing an air flow to the pin-sample contact area at the room temperature. Results of the tests are illustrated in Fig 3.5(b). In this case, the difference in volume loss between the base alloy and those with yttrium decreased. For instance, the volume loss of Mg-3%Al-5%Y is about half of that of Mg-3%Al now. One interesting observation is the smaller wear volume loss for Mg-3%Al-5%Y sample with no air flow than that of under the air flow. This could be a result of an accelerated formation of the oxide film due to frictional

heating which could be more or less protective and thus, could lead to a reduced wear loss, compared to the sample tested with an air flow which experienced less frictional heating.

Fig 3.6 shows micrographs of worn surfaces of the samples with different amounts of yttrium, tested with an air flow directed to the pin-sample contact area (corresponding to Fig 3.5(b). There is no significant morphological difference in wear track morphology among the samples. As illustrated, abrasive wear is the main wear mode involving considerable plastic deformation.

3.3.3 Corrosion Behaviour

Corrosive wear involves the synergy between wear and corrosion [90]. It is therefore of importance to evaluate the corrosion behaviour of the alloy under the influence of added yttrium. Fig 3.7 illustrates changes in the corrosion potential of Mg-3Al-Y versus the Y content. As shown, the corrosion potential decreased with added yttrium and became stable when the added Y exceeded 3 wt%. Corresponding corrosion currents were determined and are illustrated in Fig 3.8, which shows that the corrosion rate decreased initially when yttrium was added and reached the minimum around 2%Y and then slightly increased as more yttrium was added. It should be noted that although the data scattering is relatively large for the electrochemical measurements (each presented value is an average of at least three repeated tests), the general trends are there and consistent with results of another set of electrochemical tests performed in the same laboratory for Mg-3%Al-Y% alloys, which were fabricated using an extrusion process.

Regarding possible mechanisms responsible for the beneficial effect of a small amount of rare-earth on the corrosion resistance of Mg alloy, it is suggested that adding RE to Mg alloys may improve the passivation of the alloy via incorporation of REs in the surface film of $Mg(OH)_2$ [91] or stabilize corrosion product films to suppress further corrosion [92]. This, however, may not explain our observation during

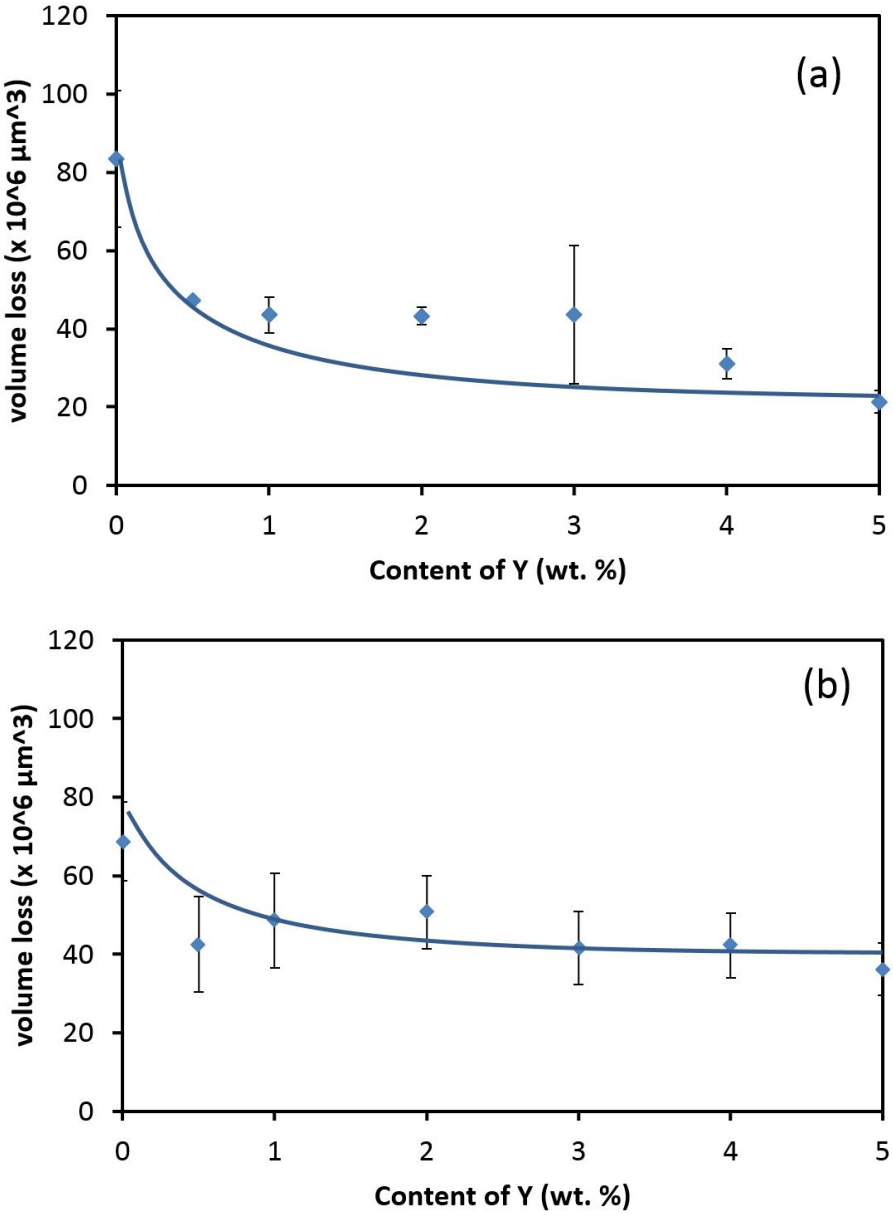

Figure 3.5: Volume losses of samples containing different amounts of yttrium up to 5 wt% Y caused by dry wear: (a) without an air flow, and (b) with an air flow to cool the pin-sample contact area during the wear tests.

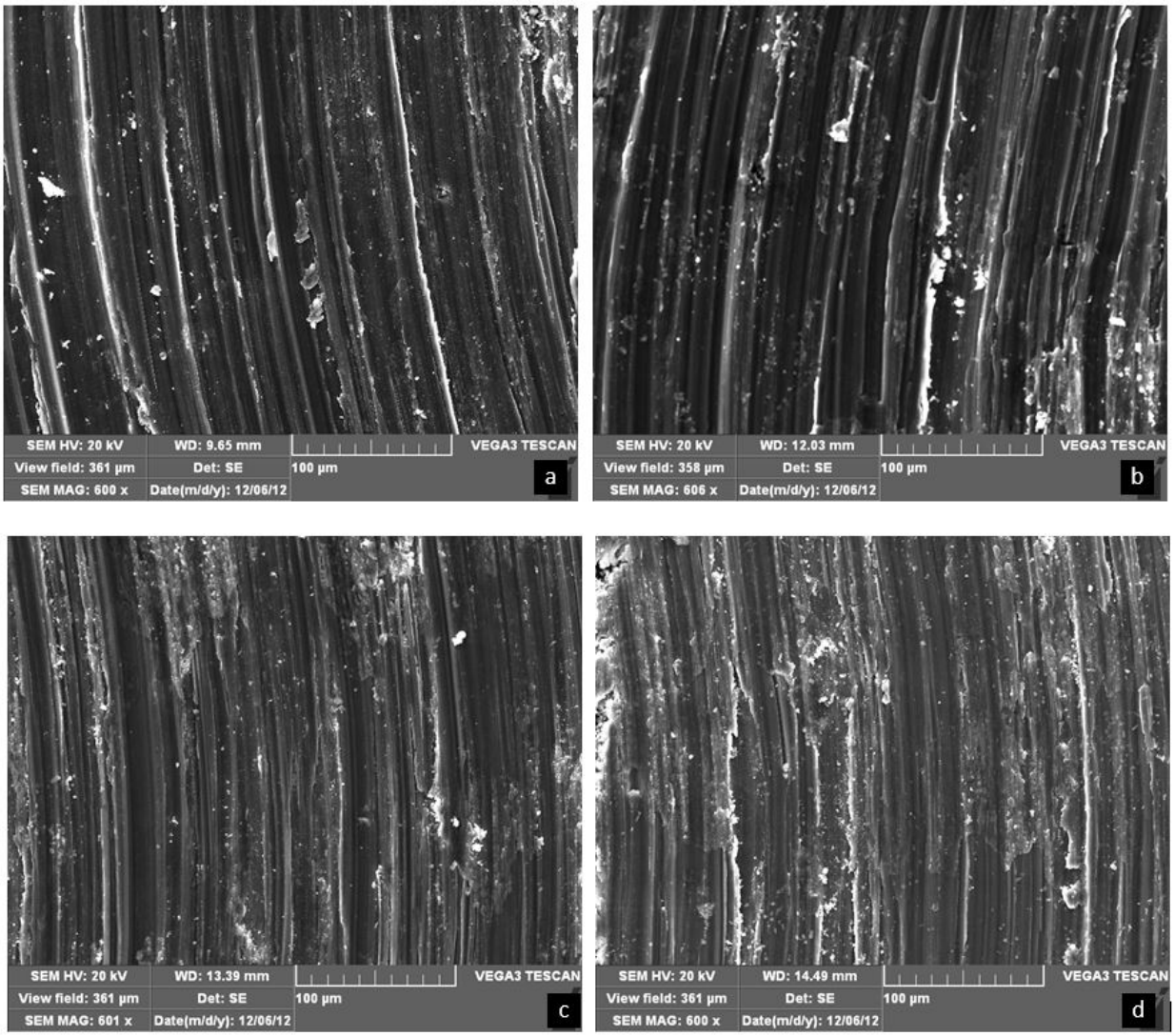

Figure 3.6: SEM images of worn surfaces: a) Mg-3%Al b) Mg-3%Al-1%Y c) Mg-3%Al-3%Y and d) Mg-3%Al-5%Y samples, experienced dry wear tests with an air flow.

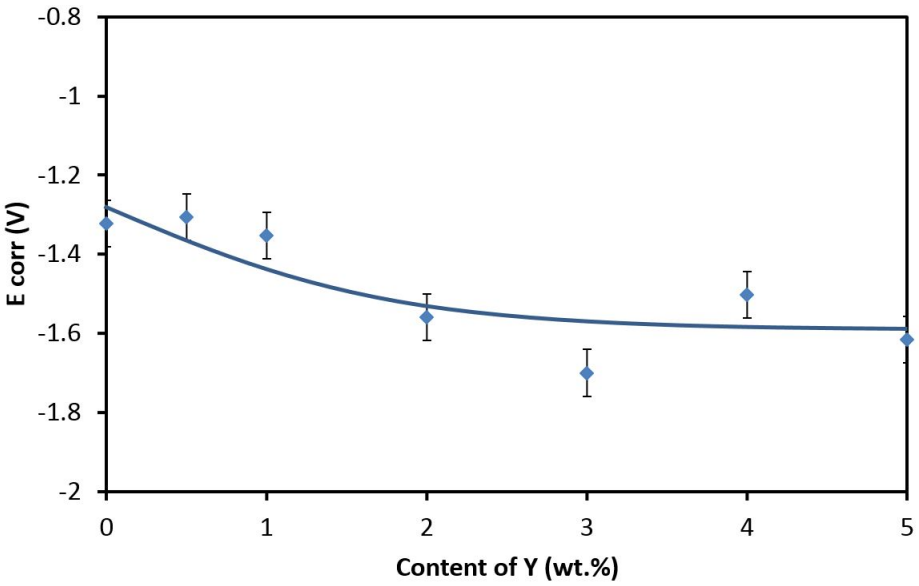

Figure 3.7: Corrosion potential (E_{corr}) of Mg-3%Al alloy containing up to 5 wt.% Y. The reference electrode was a saturated calomel electrode (SCE).

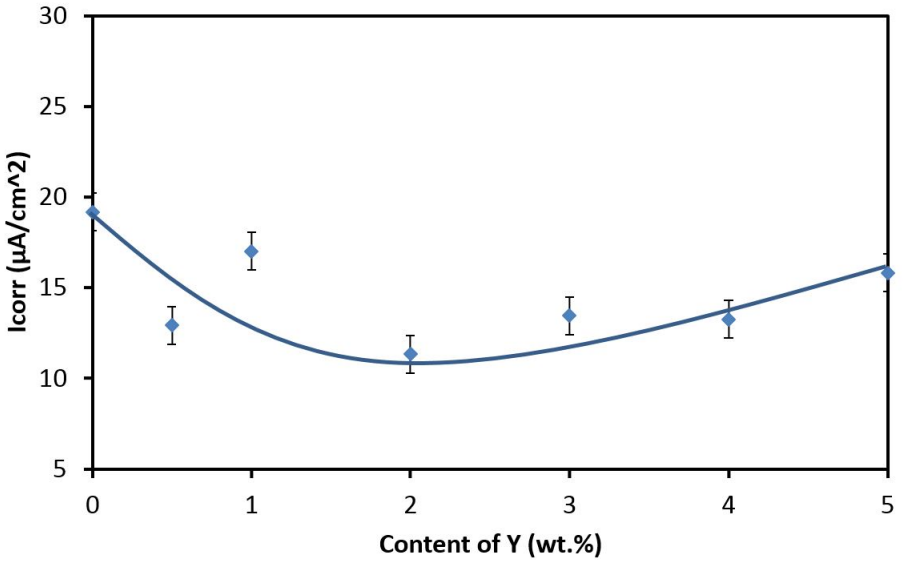

Figure 3.8: Corrosion current (I_{corr}) of Mg-3%Al alloy containing up to 5 wt.% Y.

the polarization test where the electrochemical driving force or potential was applied. Under the applied potential, the materials dissolved and there was not a developed protective passive film on the samples. As shown in Fig 3.7, the decrease in the corrosion potential by adding small amounts of active yttrium may support the argument that no effective protective oxide film was developed on the surface of the alloy, otherwise the corrosion potential could change in the opposite direction. It has also been suggested that Al-RE compounds such as Al_3RE phase may decrease the cathodic reduction rate [84]. In the Mg-Al alloy, $Mg_{17}Al_{12}$ precipitates are cathodic relative to the Mg matrix [93], which may act as micro-cathodes to cause galvanic corrosion and thus accelerate the corrosion process of the Mg matrix. Besides, the Al-rich domains in Fig 3.3(a) should also be cathodic relative to the Mg matrix, bear in mind that Al has a higher electrode potential than Mg. In the present study, the addition of yttrium eliminated or significantly decreased the $Mg_{17}Al_{12}$ phase and Al-rich domains, resulting in relatively homogenized element distributions as shown in Fig 3.3, which should consequently weaken the galvanic effect caused by the cathodic $Mg_{17}Al_{12}$ phase. It should be indicated that the Al_2Y phase may also act as a cathode to induce galvanic effects, since it was observed that during corrosion Al_2Y domains protruded and surrounding Mg matrix preferentially dissolved, indicating that Al_2Y phase is cathodic relative to the Mg matrix as well [87]. However, a small amount of added yttrium did not produce many such micro-electrodes, e.g., as Fig 3.1(b) and (c) illustrate. The alloys containing yttrium with low concentrations show relatively homogeneous element distributions such as those shown in Fig 3.3(b) and (d). Besides, the domains of Al_2Y phase are smaller than the Al-rich domains in the Mg-3%Al alloy without Y (see Fig 3.3(a)), which helps weaken the galvanic effect, since the smaller the area ratio of cathode to anode, the lower the galvanic effect [94, 95]. However, as the amount of added yttrium was increased, the volume fraction of Al_2Y phase increased, leading to the formation of high-density micro-electrodes (see Fig 3.3(d)). As a result, the galvanic corrosion could be increased, which may explain

why the corrosion rate initially decreased and then somewhat increased as the amount of added yttrium was continuously increased in the range of yttrium concentration under study.

The benefit of added yttrium on the corrosion resistance may also be seen from changes in surface roughness due to the development of oxide scale (not a protective passive film) on samples with and without added yttrium when immersed in tap water for 14 days. If there was no applied electrochemical driving force or potential, an oxide scale could develop and stay on surface. As shown in Fig 3.9, the oxide scale on the base Mg alloy without Y is very rough and thicker while those with added yttrium are much smoother. Besides, the oxide scale on the sample without Y does not fully cover the surface, since a thicker scale with the interfacial lattice mismatch generally has larger interfacial stress [96], which may result in oxide scale cracking or discontinuous growth of the oxide scale during the corrosion process.

3.3.4 Corrosive Wear Behaviour

The wear behaviour of the alloys in tap water was evaluated. Results of the tests are presented in Fig 3.10, in which the results of dry wear tests with the air flow are also presented for comparison. As shown, the volume loss of the Mg-Al alloy in the solution is lower than that under the dry wear condition (with the blown air flow). The lower wear loss in tape water should be ascribed to possible cooling and lubrication effects of water. Although during the dry wear tests, an air flow was directed to the pin-sample contact area to prevent temperature increase, the local temperature at contacting asperities could still rise, leading to enhanced local adhesion and material softening with significant plastic deformation and ploughing tracks as shown in Fig 3.6. Such local frictional heating effect could be largely suppressed when worn in water, which may also act as a lubricant. Fig 3.11 presents SEM images of worn surfaces of the samples experienced wear tests in tap water. As illustrated, much less ploughing and plastic deformation were observed on the worn surfaces.

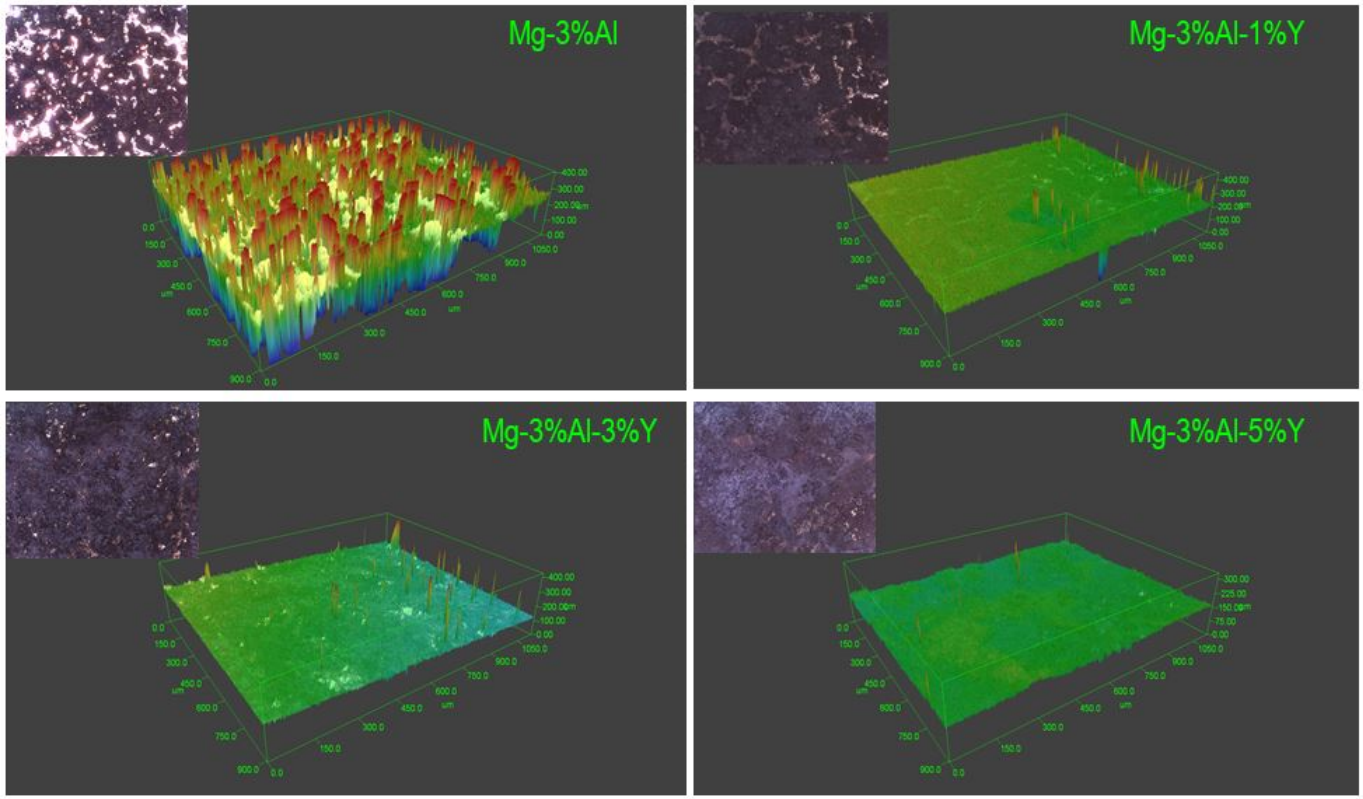

Figure 3.9: Oxide scale roughness of samples versus the yttrium concentration. The oxide developed when the samples were immersed in tap water for 14 days at the room temperature.

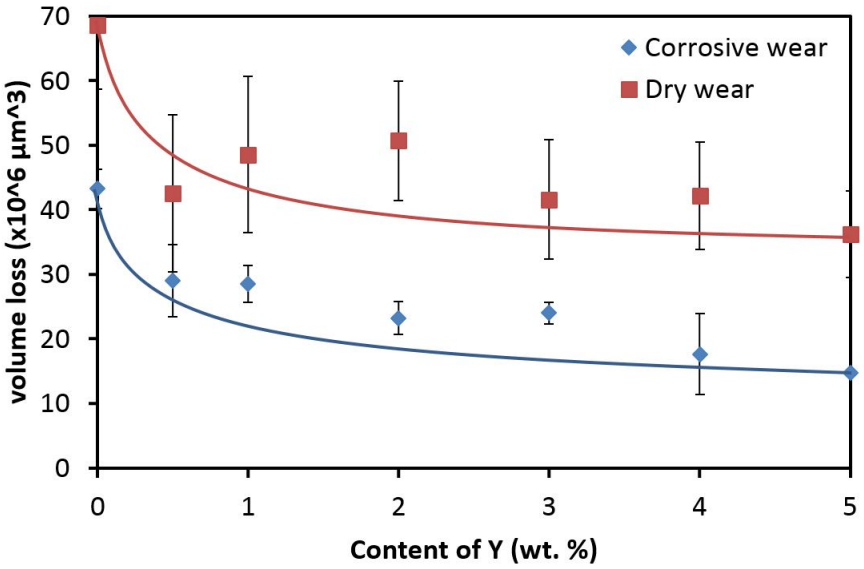

Figure 3.10: Corrosive wear testing results of Mg-3%Al alloy containing up to 5 weight% Y in tap water.

As shown in Fig 3.10, the rate of the volume loss decreased as yttrium was added. The volume loss appeared to be relatively saturated as the Y concentration was continuously increased within the range of Y content under study. With the knowledge of the corrosion behaviour of the alloys in tap water, the variations in volume loss with respect to the added yttrium can be explained. The decrease in the volume loss with added yttrium is attributed to two factors: 1) increased hardness due to the produced harder Al_2Y phase, and 2) improved corrosion behaviour due to the elimination of coarser cathodes of eutectic-like Al-rich domains and $Mg_{17}Al_{12}$ phase. However, the hardening effect of added yttrium could be mainly responsible for the improvement in the resistance to wear in tap water, since the curves of wear loss versus Y content under the two conditions (in air and in water) are similar and only the magnitudes of wear loss are different. Water is not a strong corrosive medium, which can cause corrosion of Mg alloys but may play a minor role when the mechanical action dominates the damage process. Nevertheless, corrosion was still visible. As shown in Fig 3.11, one may see many oxide fragments on worn surface of the Mg-3Al sample without yttrium while the oxide fragments are much fewer on samples with added yttrium es-

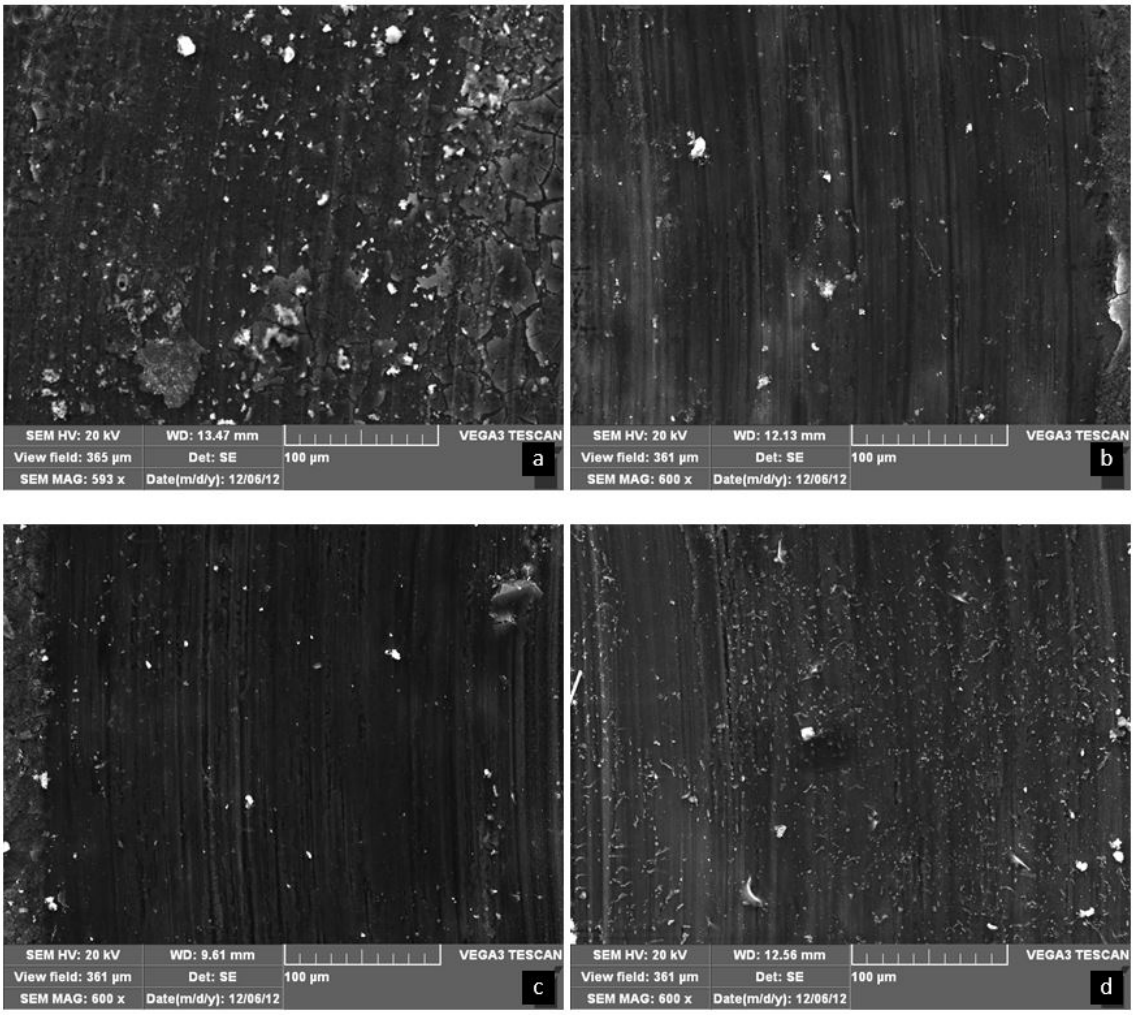

Figure 3.11: Scanning electron microscopy of the worn surfaces of: a) Mg-3%Al b) Mg-3%Al-1%Y c) Mg-3%Al-3%Y and d) Mg-3%Al-5%Y samples. Wear testing was performed in tap water.

pecially those with 1%Y and 3%Y. This is an indication that the added yttrium more or less helped suppress corrosion and thus wear-corrosion synergy, although such an effect may not be profound during the wear tests in tap water.

3.4 Conclusions

Effects of yttrium on dry wear, corrosion and corrosive wear of as-cast Mg-3%Al alloy in tap water were studied. Based on the results, the following conclusions are drawn:

1. A small amount of yttrium helped homogenize as-cast Mg-3%Al alloy, leading to decomposition of $Mg_{17}Al_{12}$ phase and vanishing of Al-rich domains, with more homogeneous element distributions. As the amount of added yttrium increased, Al_2Y phase became visible and its volume fraction increased, accompanied with increases in hardness and corresponding dry wear resistance.

2. A small amount of yttrium enhanced the corrosion resistance of Mg-3%Al in tap water and the corrosion current reached the minimum in the range of 2%Y. The benefit of added yttrium decreased as the amount of added yttrium was further increased.

3. The added yttrium reduced wear of the Mg alloy in tap water with reduced oxide fragments, indicating that yttrium helped suppress corrosion-wear synergy. However, it appears that the increase in the corrosive wear resistance of the Mg alloy with yttrium addition was mainly attributed to the increase in hardness and the corrosion may only play a minor role during corrosive wear in this medium.

Chapter 4

The Effect of Yttrium on the Performance of AZ31 Alloy[1]

4.1 Introduction

Among magnesium alloys, AZ series alloys containing 3-9 %Al and up to 1% Zn are one of the most widely used series due to their relatively good strength, ductility and corrosion resistance at room temperature [97]. Aluminum enhances strength, castability, and corrosion resistance of these alloys. Commercial Mg-Al alloys usually do not exceed 10 wt% Al to avoid a brittle structure. To improve fluidity and room temperature strength of Mg-Al alloys, a few percentage of zinc, usually 1 wt%, is added [8]. In comparison to the Mg-Al binary system, the addition of Zn does not generate any new phases in the microstructure if the the ratio of Al to Zn is greater than 3:1. Therefore, in the ternary system of Mg-Al-Zn alloys it is expected to see the same phases as in the Mg-Al system with some modifications in their stoichiometry. For example, zinc substitutes aluminium in β-$Mg_{17}Al_{12}$ phase and creates a ternary intermetallic compound of $Mg_{17}Al_{11.5}Zn_{0.5}$ or $Mg_{17}(Al,Zn)_{12}$ [98]. The addition of zinc to the Mg-Al system decreases the solid solubility of Al in the matrix of magnesium and increases the amount of the precipitates formed. More precipitation makes some enhancement in the strength of the alloy [99, 100, 101, 102].

[1] A version of this chapter has been published as a peer-reviewed article in Wear, Volume 302, 2013, Pages 1624-1632

The intrinsically low strength and poor corrosion resistance of Mg are two main drawbacks to the expansion of the applications of Mg-Al-Zn alloys. [27, 31] and continuous efforts are being made to improve their mechanical properties and corrosion resistance [103, 104]. Since during operation many industrial compounds are in dynamic contact in various environments, the wear resistance especially corrosive wear behaviour is also an important parameter for materials selection. However, the corrosive wear behaviour of Mg alloys is less well known. For many industrial processes, corrosive wear is a frequent surface failure mode, which could trigger failure of the entire system. It is therefore important to investigate and understand the corrosive wear behaviour of Mg alloys in order to forecast and prevent their failure in service.

Rare earth elements, such as Y, Ce, Nd, have been proven effective in improving the mechanical properties and corrosion resistance [103, 105]. However, the effect of Y in the Mg-Al-Zn alloys for enhancing corrosive wear resistance is unclear. In the Mg-Al-Zn alloys, yttrium has a high affinity for aluminum to form Al_2Y phase, which has low density (3.93 $gcm^{-}3$). Compared to $Mg_{17}Al_{12}$ phase, Al_2Y has a higher melting temperature, higher Young's modulus, higher hardness, and lower coefficient of thermal expansion [106]. The formation of more thermodynamically competitive Al_2Y (i.e. corresponding to a larger decrease in Gibbs free energy) suppresses the precipitation of $Mg_{17}Al_{12}$. Clarification of the effect of yttrium on the corrosive wear behaviour of Mg-Al-Zn alloys is of significance not only for industrial applications but also for scientific understanding.

In this study, Mg-3%Al-1%Zn alloys containing small amounts of yttrium (0, 0.5-4 wt%) were prepared using an induction furnace. Dry sliding wear, corrosion and corrosive wear tests were performed to evaluate the effect of yttrium on the corrosive wear resistances of Mg-Al-Zn alloys and related properties.

4.2 Experimental Procedure

Pure magnesium (99.9 wt%), pure aluminum (99.9 wt%), pure zinc (99.9 wt%) and pure yttrium (99.99 wt%) were used as raw materials. Ingots of Mg-3Al-1Zn (wt%) with different contents of Y (i.e., 0 wt%, 0.5 wt%, 1 wt%, 2 wt%, 3 wt% and 4 wt%) were melted in an middle-frequency induction furnace.

Hardness was tested with a Vickers hardness tester with a contact load of 0.3 N for 20 s. Microhardness of different domains or phases was measured using a Vickers microhardness tester (Fisherscope H100C Microhardness Measurement System with WIN-HCU software). The phase composition was analyzed by X-ray diffraction (XRD) with Cu Kα radiation at a scan rate of 2°/min within the angle range from 30 to 120.

Microstructures of samples were examined with an optical microscope (OM) and a scanning electron microscope (SEM, VEGA 3) equipped with an energy-dispersive spectroscopy (EDS). Specimens for microstructure observation were sectioned, polished and etched using 2% Nital.

The corrosion resistance was evaluated based on the Tafel curves obtained from electrochemistry measurements in a 3.5 wt% NaCl solution. Before the corrosion test, each specimen connecting to a metal wire was mounted using epoxy resin with a surface area of 1 cm^2 exposed to the testing solution. The target surface of the mounted specimen was ground with silicon carbide papers up to 800-grit, and cleaned with acetone. A saturated calomel electrode (SCE) was used as the reference electrode and a platinum plate with area of 1 cm^2 was used as the counter electrode. The corrosion current density was determined using the Tafel extrapolation method.

Wear and corrosive wear tests were performed using a pin-on-disc tribometer (CSEM Instruments, Peseux, Switzerland) in agreement with G99-05 ASTM Standard [80]. In this work, the pin was a ball made of silicon nitride (Si_3N_4) with a diameter of 3 mm. During a wear test, the pin was pressed onto a rotating specimen

under an applied load. Both the dry wear and corrosive wear tests were carried out under a load of 2 N over a sliding distance of 12.57 m at a sliding speed of 1 cm/s. The wear loss was measured using an Axio CSM 700 confocal microscope (Carl Zeiss). The wear rate was calculated as the volume loss per unit sliding distance in mm^3/m.

4.3 Results and Discussion

4.3.1 Microstructure and Hardness

XRD patterns of Mg-3%Al-1%Zn alloys containing different amounts of yttrium are illustrated in Fig 4.1. As shown, Mg-3%Al-1%Zn alloy consists of two phases: Mg matrix and $Mg_{17}Al_{12}$ phase. With the addition of yttrium, some new peaks appear, which come from the Al_2Y phase. Based on the peak intensity, one may see that the fraction of Al_2Y increased with increasing yttrium, and the formation of $Mg_{17}Al_{12}$ looked to be somewhat suppressed.

Fig 4.2 shows optical micrographs of Mg-3%Al-1%Zn alloys with different amounts of yttrium. Mg-3%Al-1%Zn alloy contains Mg and $Mg_{17}Al_{12}$ precipitates, which are distributed mainly at grain boundaries forming either a continuous network (marked by white arrows) or presented with a granular morphology (marked by white arrows with a round tail) as shown in Fig 4.2(a). After adding a small amount of yttrium, the amount of continuous $Mg_{17}Al_{12}$ phase decreased and almost disappeared when the addition of yttrium is more than 1 wt%. The majority of $Mg_{17}Al_{12}$ phase existed with a granular morphology dispersed in the Mg matrix. A small amount of rectangular or granular precipitates (pointed by white arrows with a cubic tail) also existed in the matrix, which is considered as Al_2Y as explained later. There is a significant increase in the amount and size of Al_2Y when adding 2 wt% yttrium. A spot of Al_2Y also existed, as shown in Fig 4.2(e). The Al_2Y dominated the precipitate when content of yttrium was increased to 4 wt%.

The morphology and compositions of different phases in the samples were further

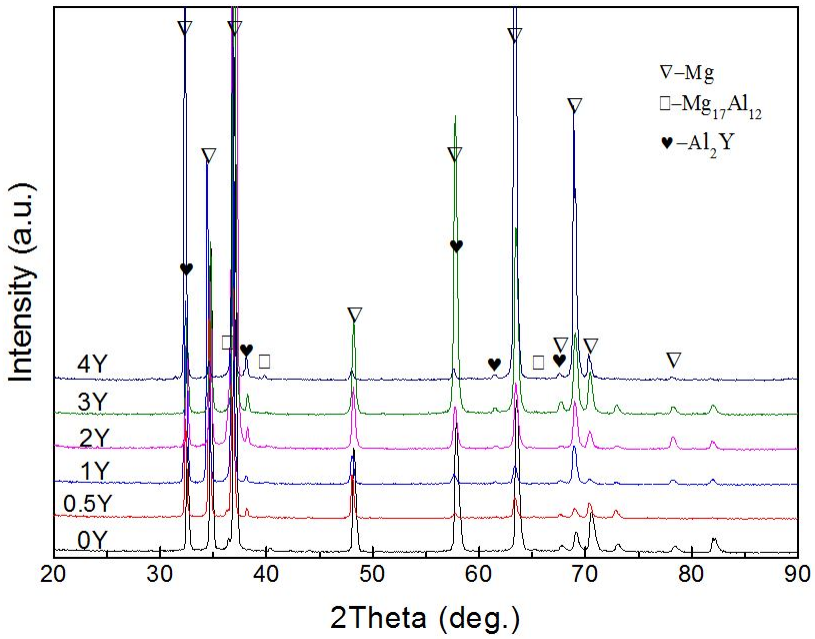

Figure 4.1: XRD patterns of Mg-3%Al-1%Zn alloys with different amounts of yttrium.

confirmed by SEM and EDS. As shown in Fig 4.3 and Table 4.1 for Mg-3%Al-1%Zn-(4%Y) alloys, spot A and B are $Mg_{17}Al_{12}$ phase with different morphologies. There is also fine Mg+$Mg_{17}Al_{12}$ eutectic (marked as α+β) mainly distributed around $Mg_{17}Al_{12}$ precipitates. According to the EDS results of spots C and D, both rectangular and acicular precipitates are Al_2Y. The EDS result of area E, which is selected from the matrix, showed there is no yttrium dissolved in the matrix.

It is evident that $Mg_{17}Al_{12}$ phase formed in a network dendritic structure in Mg-3%Al-1%Zn alloy when there is no yttrium. The $Mg_{17}Al_{12}$ phase at grain boundaries developed from the eutectic reaction. No phase containing Zn was detected. In comparison with binary Mg-Al, new phases usually do not appear in commercial ternary alloys with zinc (like AZ31) when the Al to Zn ratio is larger than 3:1 [98]. With the effect of yttrium on microstructure refinement, the $Mg_{17}Al_{12}$ network disappeared with a decrease in the volume fraction of $Mg_{17}Al_{12}$ as shown in Fig 4.2. The decrease in the amount of $Mg_{17}Al_{12}$ and increase in Al_2Y precipitates are attributed to the higher affinity of Y than that of Mg to Al [107], which is related to their electroneg-

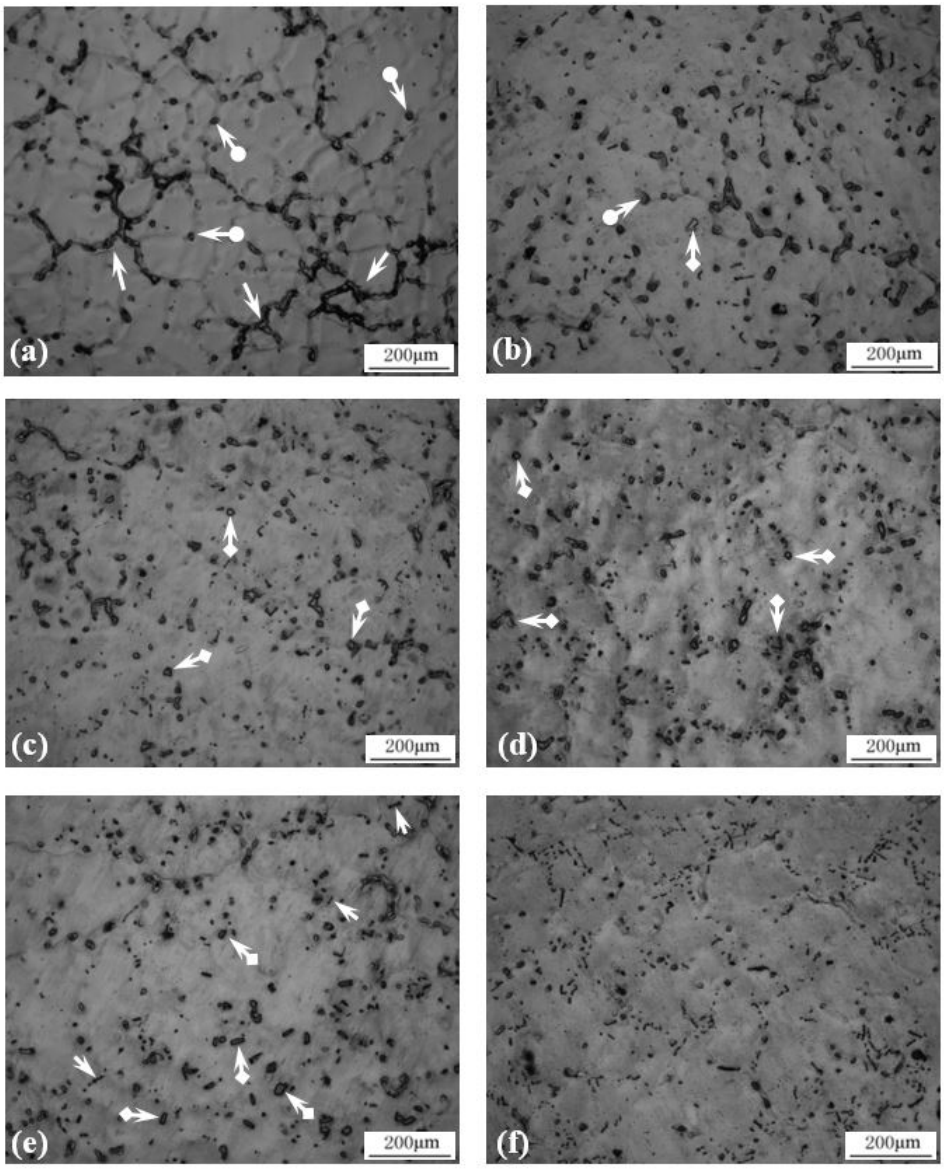

Figure 4.2: Optical micrographs of Mg-3%Al-1%Zn alloys with different amounts of yttrium: a) 0, b) 0.5, c) 1, d) 2, e) 3, and f) 4 wt%.

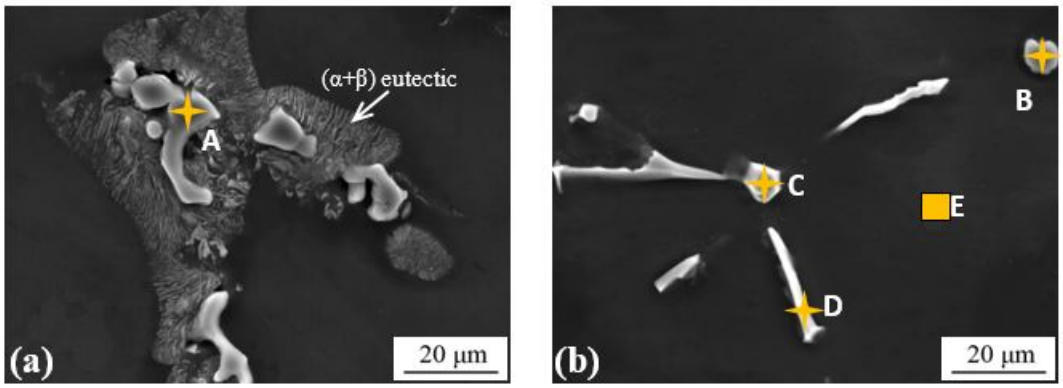

Figure 4.3: SEM images of different phases in a) Mg-3%Al-1%Zn, and b) Mg-3%Al-1%Zn-4%Y.

Table 4.1: Elemental compositions in different areas of Mg-3%Al-1%Zn alloys from Fig 4.3

	Elemental compositions (at.%)			
Area	Mg-K	Al-K	Zn-K	Y-L
A	65.15	31.19	3.66	-
B	62.77	31.64	5.6	-
C	6.6	60.94	0.34	32.13
D	39.58	42.21	0.19	19.01
E	98.78	0.97	0.25	-

ativity values. The larger the electronegativity difference between two elements, the more is their tendency to form stable compounds. The electronegativity values of Mg, Al, and Y are 1.31, 1.61 and 1.22, respectively, from which it can be inferred that the tendency of Y to react with Al to form a stable compound with Al is higher than that of Mg with Al [108].

Hardness of different samples and microhardness of different phases are shown in Fig 4.4. The hardness of samples increased with increasing yttrium content and reached a maximum value of 62 HV when the yttrium content is 2 wt%. The hardness then decreased when more than 2 wt% Y was added. The initial increase in hardness is directly related to the microstructural refinement causing by yttrium, which also introduced harder and well dispersed Al_2Y precipitates. However, with further increase of the amount of yttrium, more acicular Al_2Y are present, whose strengthen-

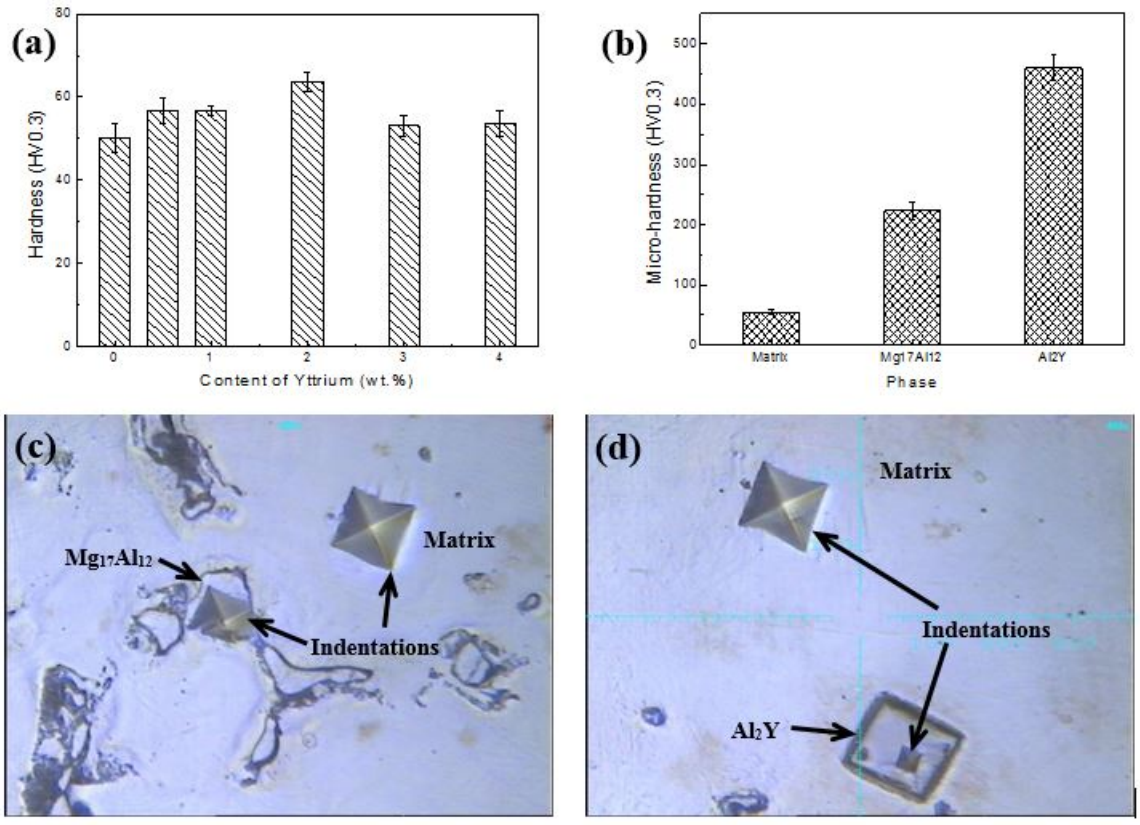

Figure 4.4: Hardness of Mg-3%Al-1%Zn alloys with yttrium; a) hardness, b) micro-hardness, c) and d) indents on different phases.

ing effect is not as strong as that of granular or rectangular Al_2Y precipitates, since under applied stress an acicular precipitate (e.g., see the precipitate marked by "D" in Fig 4.3(b)) may generate larger stress concentration than a granular or rectangular precipitate, reducing the resistance to external stresses or mechanical loads.

4.3.2 Dry Sliding Wear

Wear rates of Mg-3%Al-1%Zn alloys with different yttrium contents during dry sliding wear under a load of 2 N are shown in Fig 4.5. The wear rate decreased with increasing yttrium and reached a minimum value at 2 wt% yttrium, which was 44.4 % smaller comparing to the Y-free sample. There was a slight increase in wear rate when more than 2 wt% yttrium was added. In general, the wear resistance is proportional to the hardness of material [76]. The improvement in wear resistance is attributed to

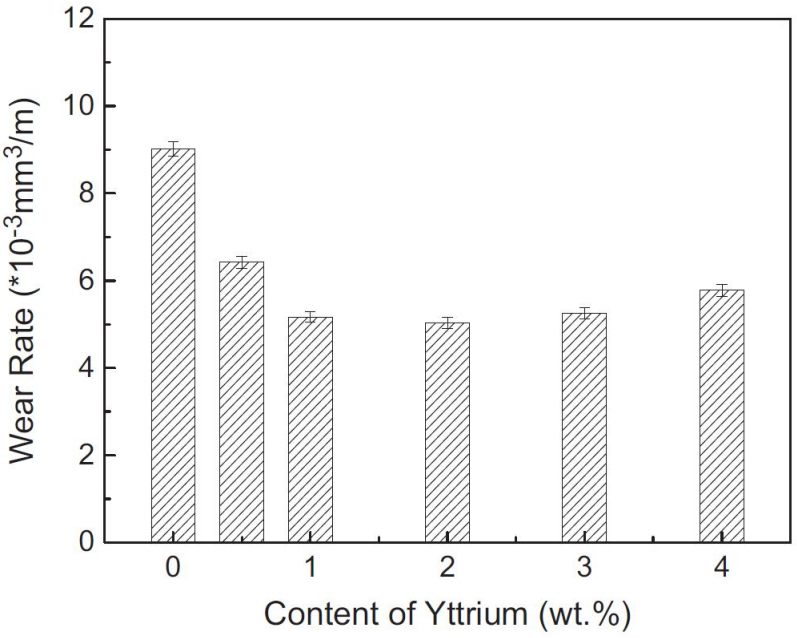

Figure 4.5: Dry sliding wear rates of Mg-3%Al-1%Zn alloys with different amounts of yttrium.

the enhancement of hardness by the harder Al_2Y precipitates and the microstructure refinement as yttrium was added.

Worn surfaces of samples after sliding wear tests are illustrated in Fig 4.6. As shown, there are ridges and grooves along the sliding direction. These are characteristics of abrasive wear, in which hard debris plough or cut into the sample, causing wear by the removal of small fragments or ribbon-like chips of material, which is confirmed by the morphology of debris shown in Fig 4.7. When adding less than 2 wt% yttrium, the amount of ridge decreased and grooves became shallow. These results correspond to an increase in the wear resistance resulting from the raised hardness. Further increase of yttrium resulted in a decrease in hardness. As indicated earlier, the acicular Al_2Y precipitates formed at higher yttrium concentrations, due to their higher stress concentration, could make micro-cracking easier with lowered resistance to wear.

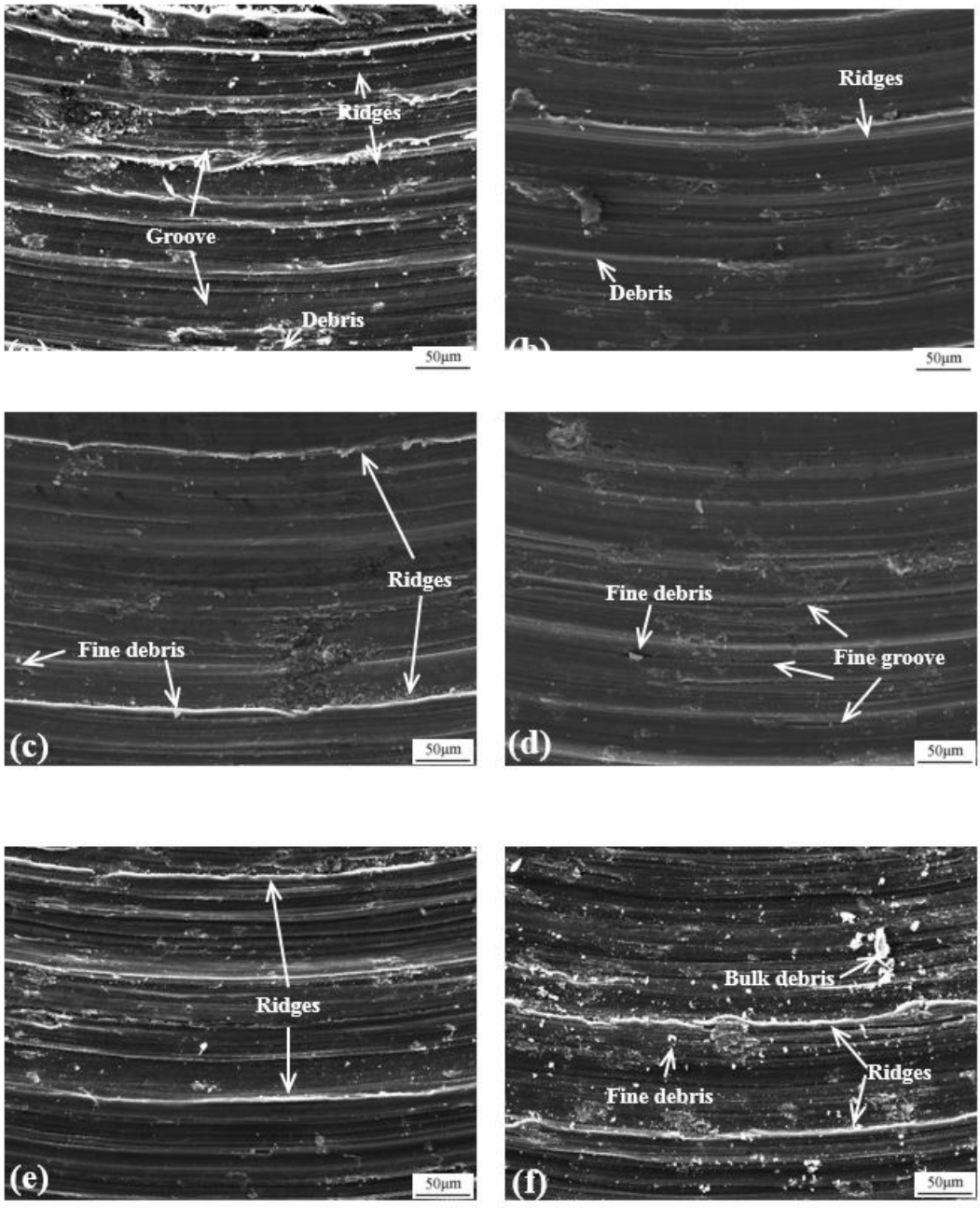

Figure 4.6: SEM micrographs of worn surfaces of Mg-3%Al-1Zn alloys with different amounts of yttrium: a) 0, b) 0.5, c) 1, d) 2, e) 3, and f) 4 wt%.

Figure 4.7: SEM micrographs of debris from the worn surface of Mg-3%Al-1%Zn alloy.

Table 4.2: Tafel fitting results (corrosion potential and current density) for the polarization curves of Mg-3%Al-1%Zn alloys with different yttrium

Y content (wt%)	0	0.5	1	2	3	4
E_{corr} (V)	-1.545	-1.529	-1.516	-1.516	-1.591	-1.677
i_{corr} (μAcm^{-2})	71	17.8	12.64	16.32	18.45	13.8

4.3.3 Corrosion Behaviour

Fig 4.8 shows the potentiodynamic Tafel polarization curves of Mg-3%Al-1%Zn alloys with different contents of yttrium in a 3.5 wt% NaCl solution. Corrosion potentials and current densities were calculated from the polarization testing results, which are given in Table 4.2. With the addition of yttrium, the corrosion potential rose and reached a maximum value with 1-2 wt% yttrium. Further increase of yttrium lowered the corrosion potential. The corrosion current density decreased sharply with the addition of yttrium, and Mg-3%Al-1%Zn alloy with 1 wt% yttrium showed the lowest corrosion current density.

The $Mg_{17}Al_{12}$ phase was more stable than the Mg matrix in NaCl solutions, since the free corrosion potential of this phase is positive relative to that of Mg in the solutions [109]. Thus the $Mg_{17}Al_{12}$ phase acted as a galvanic cathode to accelerate the corrosion reaction of the Mg matrix. When yttrium was added, it reduced the

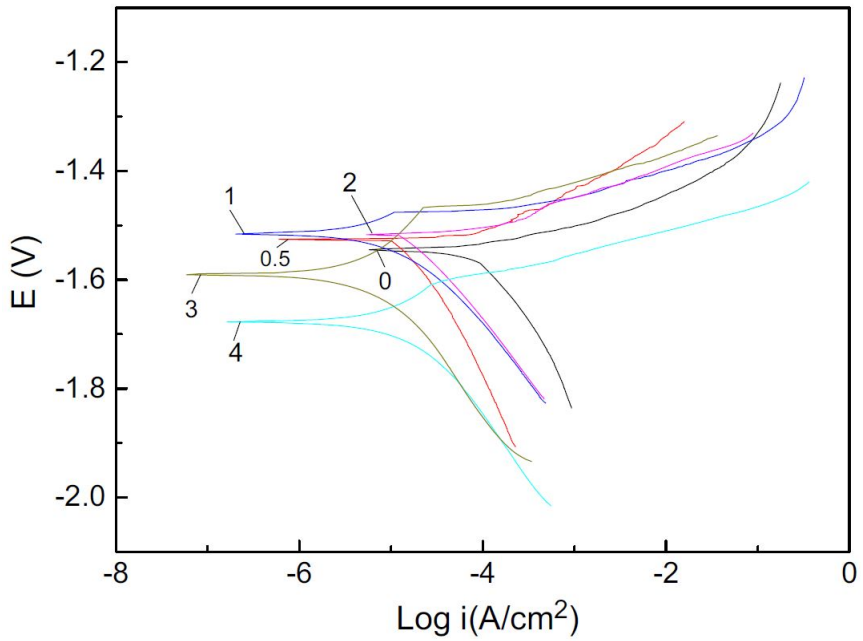

Figure 4.8: Tafel polarization curves of Mg-3%Al-1%Zn alloys with different yttrium in 3.5 wt% NaCl solution.

fraction of $Mg_{17}Al_{12}$ and reacted with Al to form fine Al_2Y precipitates. It should be indicated that Al_2Y is also cathodic relative to Mg and it was observed that during corrosion, the Mg matrix dissolved leaving Al_2Y precipitates protruding as shown in Fig 4.9 illustrates. However, although Al_2Y is cathodic, the galvanic effect of the dispersed Al_2Y precipitates may not be as strong as the network of $Mg_{17}Al_{12}$ particles as shown in Fig 4.2(a), since the smaller the area ratio of cathode to anode, the lower the galvanic effect. Addition of yttrium can refine the microstructure and this could weaken corrosion in the material [110]. Excessive yttrium would produce a larger fraction of Al_2Y precipitates which in turn is unfavourable for corrosion properties and could accelerate galvanic corrosion.

4.3.4 Corrosive Wear

Sliding wear of Mg-3%Al-1%Zn alloys with different amounts of yttrium in the 3.5 wt% NaCl solution was evaluated and the corrosive wear rates are presented in Fig 4.10. Compared to dry sliding, the 3.5 wt% NaCl solution decreased the wear rate for

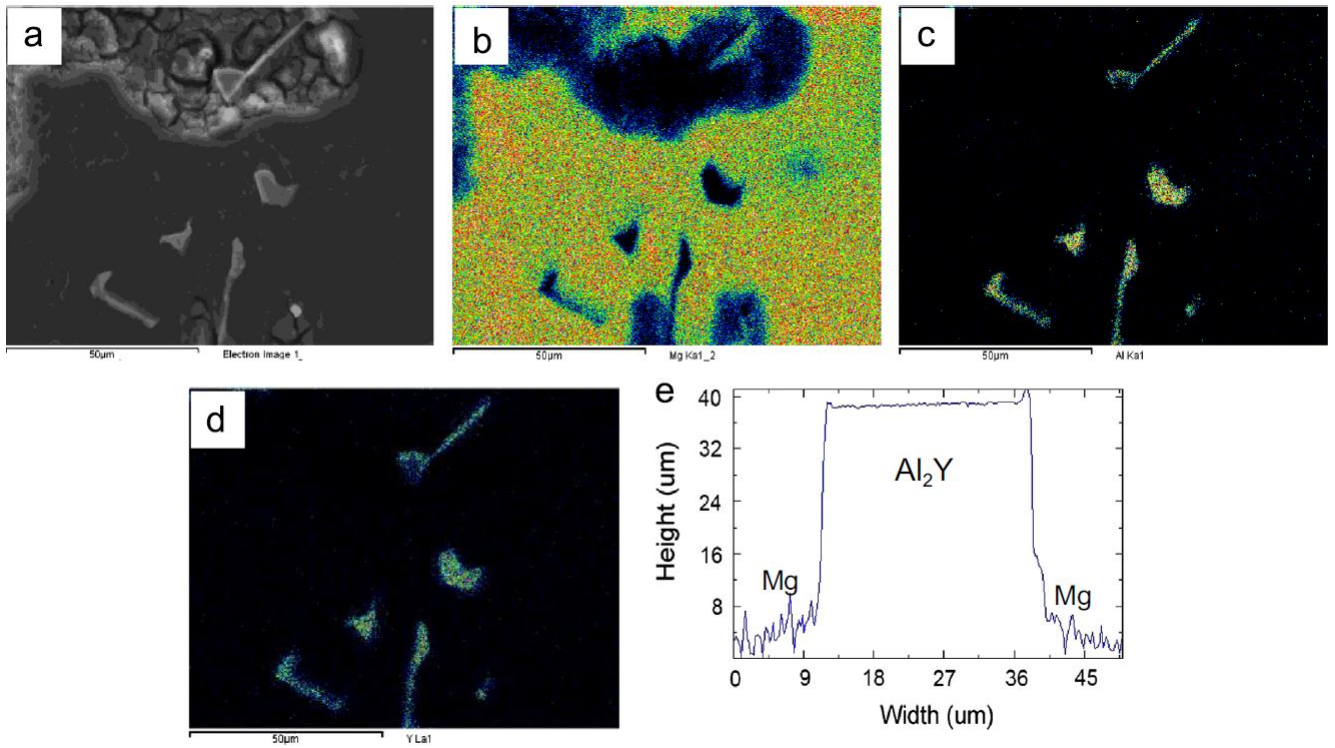

Figure 4.9: EDS element maps and corresponding image. (a) Image of the field for analysis, (b) Mg distribution, (c) Al distribution, (d) Y distribution and (e) a typical profile of a protruded Al_2Y precipitate after corrosion test, which indicates that Al_2Y is cathodic relative to the Mg matrix.

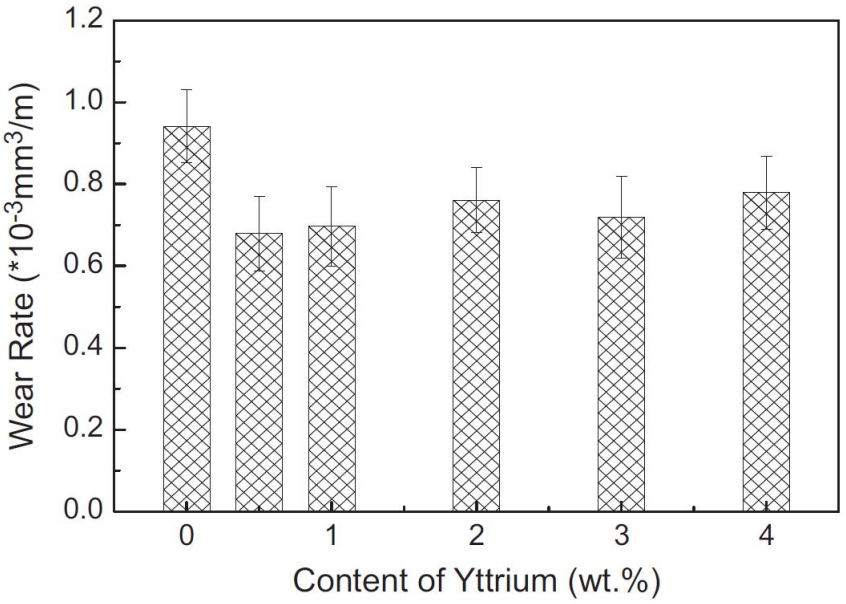

Figure 4.10: Variations in corrosive wear rate of Mg-3%Al-1%Zn alloy with the amount of yttrium in the 3.5% NaCl solution.

all the samples. Such decrease in wear damage should be caused by the lubrication effect of the solution, which could also minimize frictional heat that might soften the material. In addition, the wear debris could be removed easily by the liquid and thus could not effectively act as abrasive to accelerate wear. The wear rate decreased with addition of yttrium. This improvement should be attributed to the fact that the Y addition increased both hardness and corrosion resistance, which suppressed the synergy of corrosion and wear in the NaCl solution. The minimum wear rate appeared at 0.5 wt% yttrium. The corrosive wear rate decreased by 29%, compared to that of the base alloy without yttrium. The benefit of Y addition decreased when more yttrium was added, since excessive Y consumed more aluminum in the matrix, making the Mg matrix more anodic and thus leading to a decease in corrosion resistance. Excessive Y addition also unfavoured the mechanical strength as more acicular Al_2Y precipitates developed, which may introduce higher stress concentrations under external stresses as discussed earlier.

Fig 4.11 illustrates the SEM micrographs of worn surfaces of the samples after

sliding test in the 3.5 wt% NaCl solution. The worn surface of all samples showed lots of grooves, but they are shallower than those after dry wear. Cracks are observed at the wear scars which may come from corrosion products or harder and more brittle compounds such as $Mg_{17}Al_{12}$ phase. This implies that $Mg_{17}Al_{12}$ might become susceptible to cracking under the synergistic attack of wear and corrosion. The cracked $Mg_{17}Al_{12}$ phase could be easily removed, resulting in a lower corrosive wear resistance.

Remark

As mentioned in introduction part of the current chapter, in industrial applications of Mg-%3Al in the automotive industry, usually 1 wt% of zinc is added to the alloy to improve fluidity and mechanical strength. Comparing Fig 3.4 and Fig 4.4 , one may find that Mg-3%Al-1%Zn alloy has a higher hardness than Mg-3%Al alloy which reflects the effect of Zn on the hardness. Presence of Zn and Y in Mg-%3Al alloy results in a larger values for hardness which in turn could be beneficial for wear and corrosive wear properties.

4.4 Conclusions

In this chapter, Mg-3%Al-1%Zn alloys containing different amounts of yttrium (0-4 wt%) were prepared using an induction furnace. Sliding wear, corrosion and corrosive wear resistances of as-cast alloys were evaluated. The results showed that addition of yttrium to AZ31 alloy formed Al_2Y precipitates and minimized the precipitation of $Mg_{17}Al_{12}$ phase with a refined microstructure. The formation of uniformly distributed finer and harder Al_2Y precipitates increased hardness of the Mg-Al alloy and the hardness reached a maximum at 2 wt% Y. Excessive Y addition lowered the strengthening effect due to the formation of more acicular Al_2Y precipitates. The addition of yttrium to Mg-3%Al-1%Zn alloy also improved corrosion resistance of the alloy. The combination of improved strength and corrosion resistance resulting from the Y addition increased the corrosive wear resistance of the material.

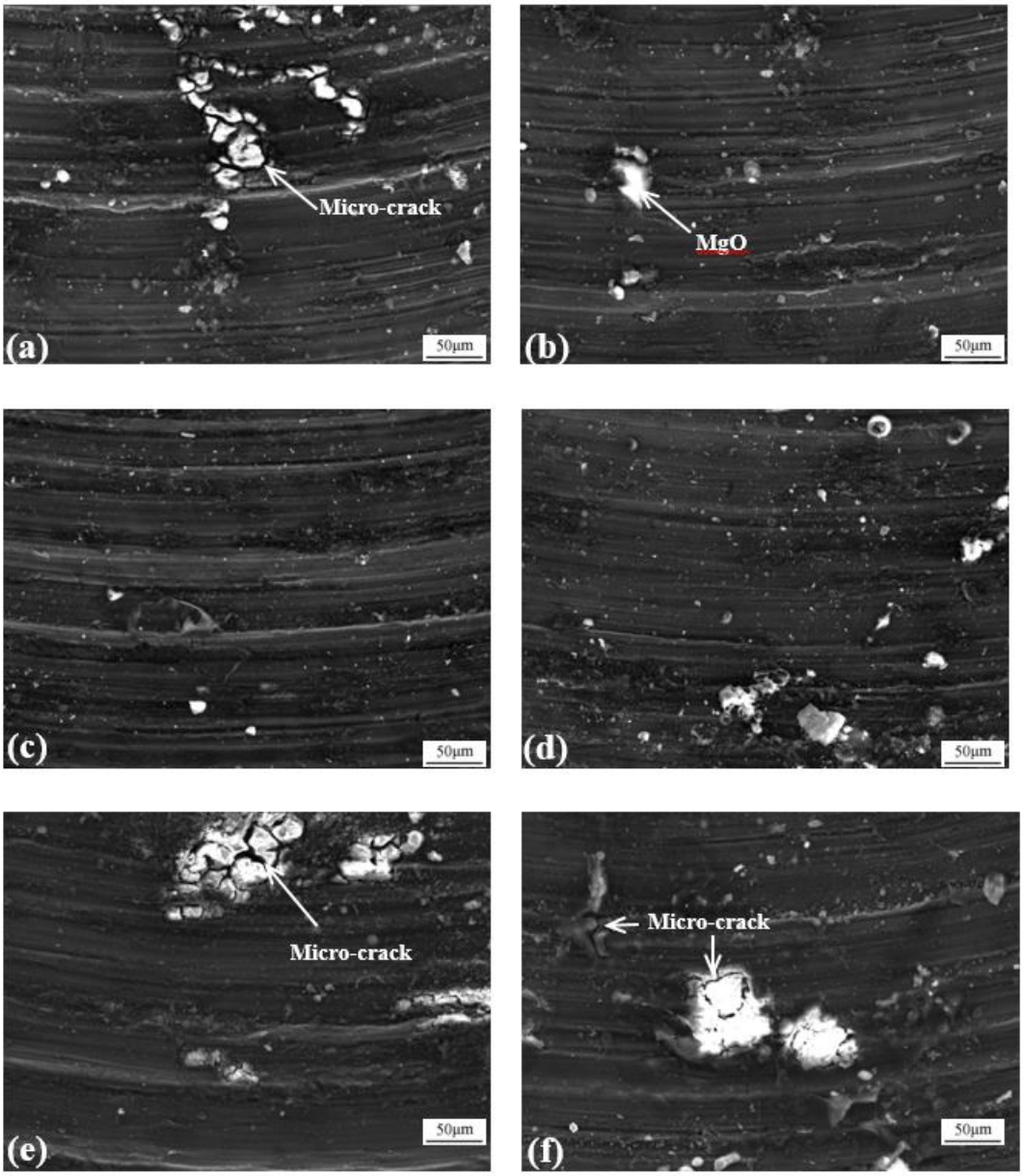

Figure 4.11: SEM micrographs of worn surfaces of Mg-3%Al-1%Zn alloys with different amounts of yttrium sliding in the 3.5% NaCl solution: (a) 0; (b) 0.5 wt%; (c)1 wt%; (d) 2 wt%; (e)3 wt%; (f)4 wt%.

Chapter 5

The Effect of Yttrium on Failure Resistance of the Surface Oxide Film[1]

5.1 Introduction

As discussed in previous chapters, yttrium can modify mictrostructure of Mg alloys, leading to improvements in their wear, corrosion and corrosive wear properties. This chapter focuses on effects of Y on the oxide film which forms on the surface of Mg alloys. When exposed to air and other environments, surfaces of Mg and its alloys are covered by films which are composed of oxides, hydroxides or other oxidized products of Mg [49, 111]. In natural environments with low humidity, reaction of Mg with oxygen produces a stable MgO film or one consisting of MgO with minor hydrated fraction. Since the Pilling-Bedworth ratio of Mg is less than unity (about 0.80), a fully protective film may not develop on Mg [12, 40]. However, the surface film is still, to a certain degree, protective against corrosion in low-humidity environments. Upon exposure to high humidity or an aqueous environment, the surface film has an increased fraction of $Mg(OH)_2$, forming a less corrosion-resistant film that is a mixture of MgO and $Mg(OH)_2$ [12, 13, 14, 41, 42, 44, 46, 112, 113, 114]. Alloying Mg with some elements affects the surface film and improves its passivation capability [45]. In

[1] A version of this chapter has been published as a peer-reviewed article in Thin Solid Films, Volume 615, 2016, Pages 29-37

the case of Mg-Al alloys, their surface films are usually mixtures of magnesium and aluminum oxides [11, 35, 47, 48, 115] and the presence of Al reduces the amounts of MgO and $Mg(OH)_2$ [49] and thickens the oxide film [50] with increased chemical stability of the film [21].

The degree of protection provided by the natural oxide surface film is crucial to the surface stability of magnesium [14, 21, 51, 52]. One of the approaches for enhancing the corrosion resistance of magnesium alloys is to improve their surface oxide films. Rare-earth elements have demonstrated their effectiveness in improving passive films for many industrial alloys. For instance, yttrium benefits mechanical properties and chemical stability of surface films on aluminized 1045 steel [54], 304 stainless steel [55] and Stellite 21 [15, 56] through increasing the adherence of passive films to the substrate and modifying the structure and properties of the films. However, research on effects of rare-earth elements on the surface film of Mg alloys is rather limited, although relevant studies can be found in the literature [31, 43, 57, 58, 59, 60, 61, 62, 63, 64, 65, 66]. These reported studies are mainly focused on the influence of rare-earth elements on the overall oxidization and corrosion behavior with little attention given to the role that the rare-earths plays in affecting properties of the oxide film. Insufficient knowledge about the role of rare-earth could lead to omission of the important approach for enhancing the corrosion resistance of Mg alloys through tailoring the surface film. A strong and adherent surface film benefits not only the resistance to corrosion but also those involving mechanical actions such as scratching or corrosive wear.

In our previous works [87, 116] the authors studied effects of yttrium, one of important rare-earth elements, on overall corrosion and corrosive wear of Mg-3%Al and Mg-3%Al-1%Zn (wt.%) alloys. However, it is unclear whether or not the added rare-earth could benefit the surface oxide film, which influences the resistance of the material to corrosion. The objective of this study is to investigate how yttrium influences the corresponding properties of the surface oxide film formed on the Mg-3%Al

Table 5.1: Compositions of Mg-Al-Y alloys under study.

Sample	Y content (wt%)	Al content (wt%)	Mg content(wt%)
Mg-3%Al	0	3	97
Mg-3%Al-1%Y	1	3	96
Mg-3%Al-3%Y	3	3	94
Mg-3%Al-5%Y	5	3	92

(wt.%) alloy, including mechanical properties, electron work function - a measure of the surface stability, and adherence to the substrate, which affect the protectiveness of the surface film against corrosion.

5.2 Experimental Procedure

Pure magnesium rods (99.9%), aluminum granules (99.9%) and yttrium powder (99.9%) were mixed in appropriate ratios and melted in an AGI induction furnace to make alloy ingots. Ingots of four different compositions were made and each ingot was re-melted five times in order to reduce the microstructural inhomogeneity. Table 5.1 shows nominal compositions of the different alloys. Samples (20 mm x 10 mm x 5 mm) were cut from each ingot and ground using SiC sand papers up to 1200 grit. The polishing was performed without water in order to prevent reaction of the surface layer with water. The polished samples were divided into 2 groups: samples of group 1 were exposed to air and those of group 2 were immersed in distilled water for 2 minutes after polishing and then dried in air.

The resistance of the surface film to scratching was evaluated using a Universal Micro-Tribometer (Bruker, Campbell, USA) with a tungsten carbide micro-blade as shown in Fig 5.1. During the scratching test, the normal load was increased linearly from 0.5 to 2 N within 240 s and the tip was moved at a velocity of 5 μms^{-1}. In situ changes in electrical contact resistance (ECR) versus the applied normal load were recorded. When the applied normal load reached a critical value at which the surface film was broken down or failed, the electrical contact resistance dropped rapidly.

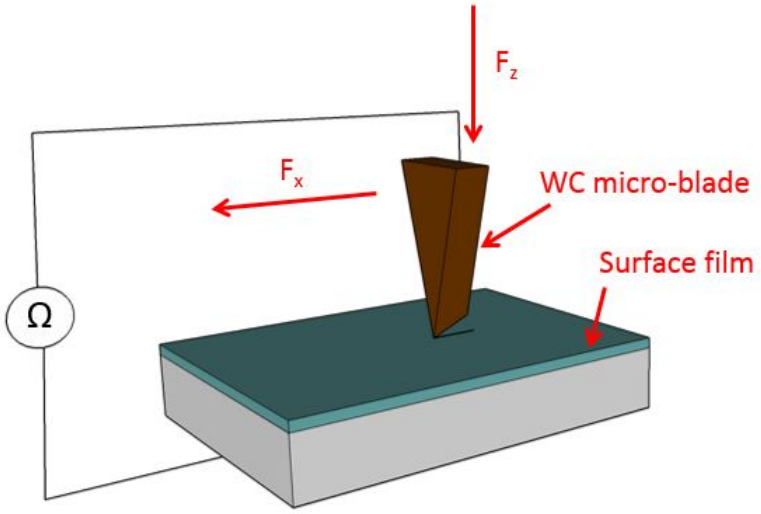

Figure 5.1: A schematic of a surface film scratched by a tungsten cabide micro-blade.

This critical load at the drop of ECR is a measure of the resistance of a surface film to scratching, affected by the adherence of the surface film to substrate and its mechanical properties as well.

Mechanical properties of surface films were evaluated using a Tribo-Scope (Hysitron, Minneapolis, USA), a combination of a nano-mechanical probe and an atomic force microscope. During the test, a normal load was applied to a diamond Vickers tip on the sample surface, which was increased linearly from 0 to 100 μN and released back to 0 μN. Load-depth curves of 5 different spots on the surface of each sample were measured.

A Scanning Kelvin Probe (KP Technology Ltd, UK) was used to measure the electron work function (EWF) of surfaces of the samples with different amounts of added Y. Measurements were performed by applying a DC potential, termed the backing potential (Vb), to the sample and detecting the output signal via an amplifier connected to the tip electrode. A data acquisition system was used to measure the average peak to peak height (Vptp) over a number of cycles as a function of Vb. The fractional change in capacity and then EWF was calculated. The EWF tests were

carried out at least on three different locations on the surface of each sample.

The composition of surface films was analyzed using the secondary ion mass spectroscopy (SIMS). Depth profiles were obtained using a Time Of Flight (TOF)-SIMS IV instrument (ION-TOF GmbH). The pressure of analysis chamber containing the samples was lower than 5 x 10^{-7} Pa before the SIMS depth profiling experiment. During depth profiling, Bi^+ ions were used as the analytical source, operated at 25 kV; Cs^+ ions were used as the sputtering source, operated at 1 kV, with an ion current of 45-90 nA. By alternating these two ion beams on samples, depth profiles were obtained. Craters having a size of 200 x 200 μm^2 were generated by sputtering, while acquisition areas of profiles were 40x40 μm^2 in centers of the craters. The depths of the craters were measured with an Alpha-200 profiler. The determined intensities of different ion fragments were normalized relative to the intensity of Al fragments. In addition, a 3D composition analysis was carried out for the Mg-3%Al-5%Y (wt.%) sample in order to demonstrate the distribution of components from the top surface into the bulk over a distance of 3.7 μm. The 3D mapping covered a surface of 120 μm x 120 μm.

5.3 Results and Discussion

5.3.1 Properties of the Surface Film Formed in Air

Indentation tests were performed on the surface layer of Mg-3%Al (wt.%) samples with different Y contents. The load-displacement curves of samples containing 0%Y, 1%Y, 3%Y, and 5%Y, respectively, are shown in Fig 5.2. From an indentation curve, maximum load, maximum penetration, and the mechanical behavior of a material can be determined and evaluated [117]. As illustrated, the addition of yttrium considerably strengthened the surface oxide film with much smaller indention depth, compared to that on the Y-free sample. Under a small maximum load of 100 μm, the tip penetration was shallow within a few nanometers so that the obtained force-depth

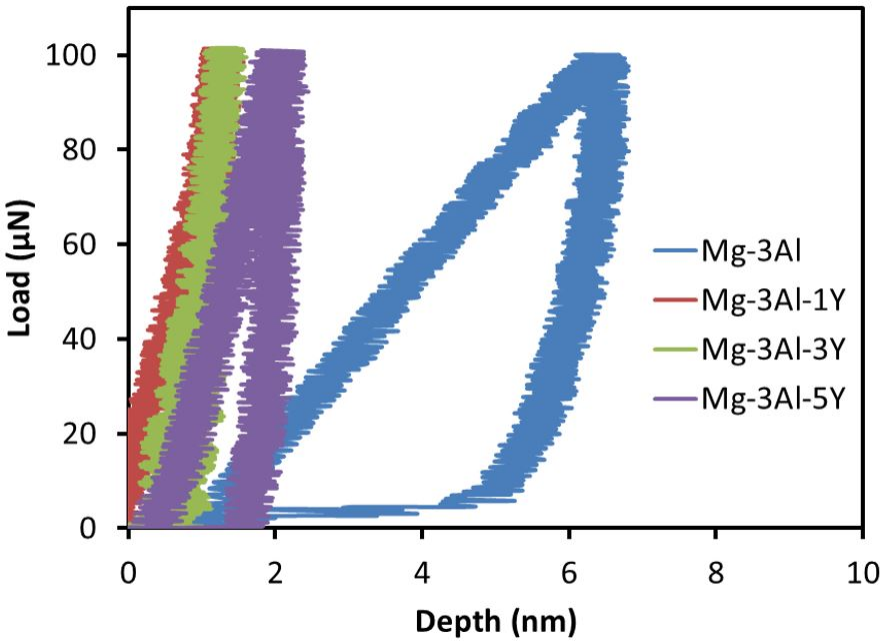

Figure 5.2: Nano-indentation loaddepth curves of Mg-3%Al (wt.%) samples exposed to air.

curve reflects the resistance of the surface film to external stress or its mechanical strength. Studies [11, 42, 118, 119] show that thickness of the oxide film on Mg-Al alloys exposed to air is in the range of 10^0-10^1 nm. Unless the film is extremely thin, the current indentation load was adequately selected. If the film is very thin and its properties evaluated by nano-indentation could be influenced by the substrate, the drawn conclusion should still stand, since such influence can be minimized or eliminated based on the following reason.

The indentation depth is a measure of the mechanical strength or the resistance to indentation, which include both elastic and plastic deformations, depending on the load level. Under a fixed load, the smaller the indentation depth, the mechanically stronger is the oxide film. Thus, the mechanical strength of a thin film can be evaluated by measuring the penetration depth under an appropriate load level from an indentation curve obtained even at a higher load level. For instance, the indentation curves shown in Fig 5.2 were obtained under the maximum load of 100 μN. In order

to exclude possible influence from the substrate if the surface films are very thin, one may measure the indentation depth at a lower load level, e.g., 30 μN, from the curves obtained at 100 μN, from which the corresponding indentation depths of, e.g., Mg-3%Al-3%Y (wt.%) and Mg-3%Al (wt.%) are only 0.8 nm and 2.5 nm, respectively. In this case, the influence from the substrate should be markedly minimized.

For comparison purpose, the indentation depths determined from the nano-indentation curves show a strong effect of Y on the resistance of the surface film to indentation. As above-demonstrated, from the indentation curves one may see that under 30 μN, the indentation depth of Mg-3%Al-3%Y is 0.8 nm, which is only 1/3 of that of Mg-3%Al, indicating that the oxide film on the Y-containing samples is much stronger than that on the Y-free sample.

The adherence of a surface film to its substrate is an important parameter in evaluating the resistance of a surface film to detachment from its substrate. If a surface film has higher adherence to the substrate, it is more protective. Fig 5.3 illustrates changes in ECR (Electrical Contact Resistance) of different Mg-Al samples as the applied normal compressive load was gradually increased from 0.5 to 2N. When the surface non-conductive oxide film was damaged or scratched off and the tip touched the metallic substrate, the electrical contact resistance rapidly decreased, although a certain layer of the substrate could contain oxide inclusions if oxygen inward diffusion and reaction with the metallic elements in the substrate occurred. As shown, adding Y increased the critical load at the ECR drop. In other words, with added Y to Mg-3%Al (wt.%) alloy, the surface film was scratched off under larger loads, indicating that Y improves the bonding between the surface film and the substrate. However, for the sample containing 5%Y (wt.%), the surface film did not show consistent performance with large variations in the critical load during the scratch tests. This may imply lower integrity or reliability of the surface film on the sample with the higher concentration of yttrium.

Electron work function (EWF) is the minimum energy required to move an elec-

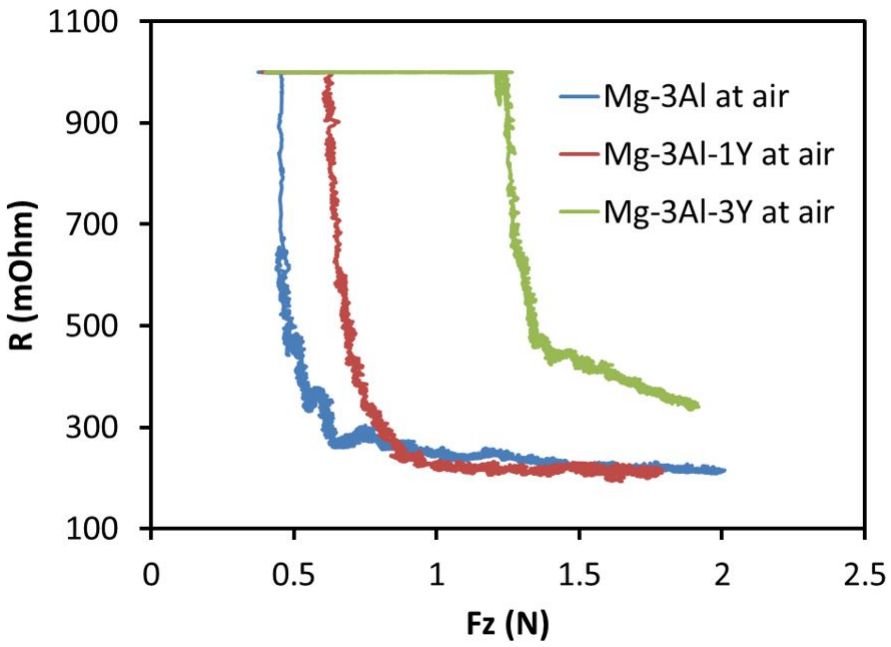

Figure 5.3: Changes in the electrical contact resistance of Mg-3%Al (wt.%) samples with different amounts of Y with respect to the normal load (Fz). The samples were exposed to air after preparation. No curve is presented for sample Mg-3%Al-5%Y (wt.%), since obtained.

tron inside a metal at the Fermi level to the surface of the metal without kinetic energy [120]. EWF of a surface oxide film as a barrier is a measure of its resistance to the escape of electrons from substrate which may participate in corrosion reactions when the surface is exposed to a corrosive environment. Thus, EWF is a parameter reflecting the surface stability or the protective role of the surface film against electrochemical attacks. The greater the electron work function, the more stable is the surface film and hence a higher resistance to corrosion reactions [116, 121]. Fig 5.4 shows EWFs of Mg-3%Al (wt.%) alloy containing different amounts of yttrium. As seen from the figure, the addition of yttrium to the alloy shifted EWF to higher values and made the surface film more stable against losing electrons, which consequently lowered the tendency of the material to participate in electrochemical or corrosion reactions.

Fig 5.5 illustrates intensities of different components in the surface films of Mg-

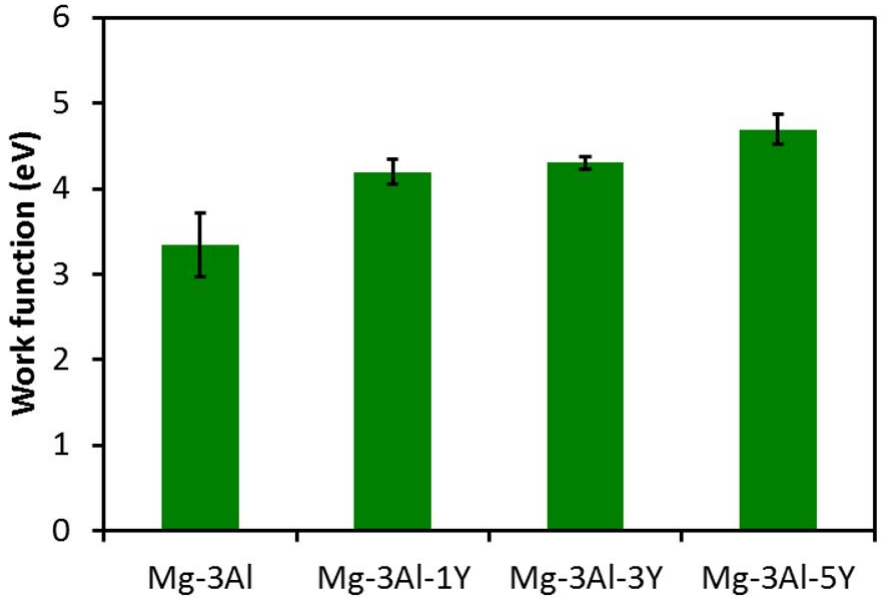

Figure 5.4: Electron work functions (EWF) of Mg-3Al (wt.%) samples containing Y up to wt. 5%.

3%Al (wt.%) samples containing 0%Y, 1%Y, 3%Y and 5%Y versus the distance from the top surface to the inside, obtained from the TOF-SIMS depth profiling analysis. The results show that the films contain MgO and $Mg(OH)_2$ and their intensities increased with an increase in the amount of added Y. However, the ratio of OH to O was influenced by the yttrium addition. It should be indicated that the ratio of OH/O should include other possible oxides, including not only magnesium oxides but also aluminum and yttrium oxides. The ratio was determined based on intensities of various relevant components. As shown, the ratio of OH/O generally decreased with increasing the Y content. Besides, Y raised the intensity of AlO component, implying that Y promoted oxidation of Al in the Mg-3%Al (wt.%) alloy. Yttrium also increased the intensity of YO although it was minor and only observed in the sample containing 5%Y.

It should be pointed out that Fig 5.5 shows intensity distributions of various O- and OH- components over a few micrometers; this does not mean that the surface

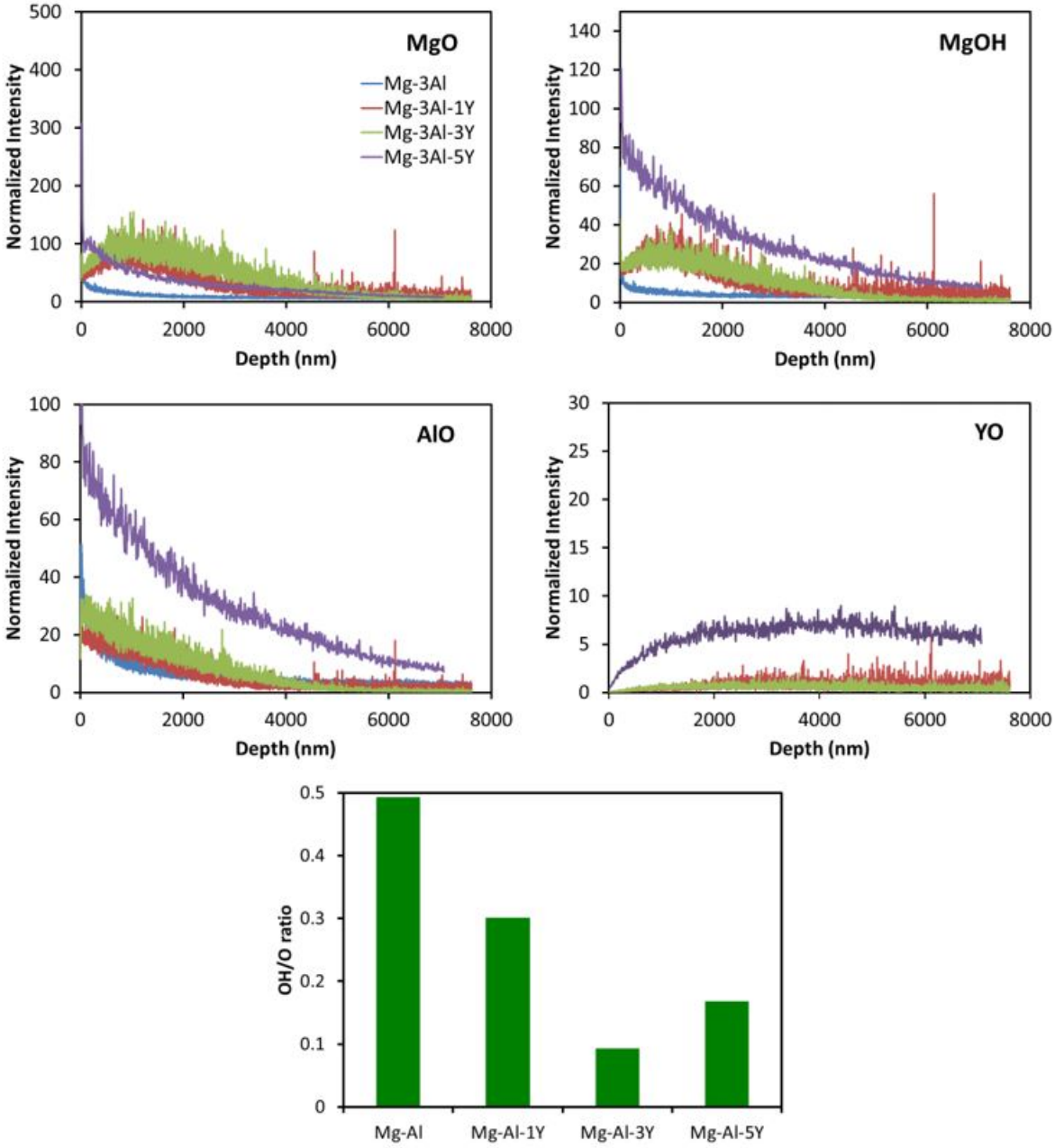

Figure 5.5: Results of TOF-SIMS analysis for Mg-3%Al-Y (wt.%) samples exposed to air: MgO, MgOH, AlO, YO, and OH/O ratio.

films have such large thickness. Yttrium is an oxygen-active element, which can promote oxygen inward diffusion or inward oxide growth [121], which could be the reason why the oxygen signal was detected over a large depth from the top surface to the bulk. In general, the oxide films on passive alloys, such as stainless steel and Al alloys, are very thin (thickness: 1-2 nm). Oxide films on non-passive materials (e.g., Mg alloys) are relatively thicker. Chiu Chen [118] investigated the oxide growth on Mg alloys using X-ray Photoelectron Spectroscopy and demonstrated that the thickness of oxide films on Mg-3Al (wt.%) alloys in ambient environment was around 4 nm. A study by Sebastin et al. [119] showed that the thickness of oxide films on magnesium and Mg-Al alloys is between 3 and 7 nm. Nordlien et al. [11, 42] demonstrated that the thickness of oxide film on pure Mg formed immediately after exposure to air was 20-50 nm, and that of oxide film on Mg-Al alloys was 20-40 nm. It is expected that the thickness of oxide films on the Mg-Al samples should be in the range of 10^0-10^1 nm. Due to the high affinity of yttrium for oxygen, Y could increase the oxide thickness but it is unlikely that Y can increase the thickness by orders of magnitude.

Comparing Figs 5.3 and 5.4 with Fig 5.5, one may see that a lower OH/O ratio appears to be beneficial to the strength and failure resistance of the surface film. As reported later, first-principles calculations demonstrate that MgO is stronger than $Mg(OH)_2$. This explains why a lower OH/O ratio corresponds to a stronger oxide film. Besides, Al_2O_3 and Y_2O_3 should also help strengthen the oxide film. More discussion regarding this issue is given in the next section. As for why yttrium increased the OH/O ratio, the high affinity of yttrium for oxygen, which may enhance oxygen inward diffusion or oxide growth, could promote forming oxides, leading to a stronger surface film which contains more MgO, less MgOH and other minor oxide components i.e. AlO and YO. However, further studies are needed in order to fully explain the role that yttrium plays in affecting the OH/O ratio. In the following section, the affinities of Mg model samples with and without dissolved Y atoms for MgO and

$Mg(OH)_2$ were analysed, respectively, using first-principles technique in order to look into the effect of Y on $Mg(OH)_2$/MgO, which should dominate the OH/O ratio, based on thermodynamics.

As regards the beneficial effect of yttrium on the resistance of the surface film to scratching, which reflects stronger interfacial bonding between the film and the substrate, this may be partially ascribed to the oxide pegging effect. Yttrium has a large atomic size and it preferably stays at grain boundaries in order to minimize the strain energy. This oxygen-active element may promote oxygen in-ward diffusion and form oxide pegs particularly at grain boundaries, thus resulting in strong adherence to the substrate. The oxide pegging phenomenon is more profound when oxide films are formed at elevated temperatures [122]. Rare-earth elements generally have more electron orbitals and actively react with surrounding substances, which may result in stronger interfacial bonding not only at grain boundaries but also other sites in contact with the oxide film.

Fig 5.6 illustrates representative 3D TOF-SIMS mapping of oxygen content in a Mg-3%Al-5%Y (wt.%) sample. The 3D map covers an area of 120 μm x 120 μm with a depth of 3.7 μm from top surface of the sample. The bright yellow zone represents high intensity of oxygen while the darker zone represents lower oxygen intensities. Inward oxygen diffusion appears to be profound. Compare the range that oxygen spans in samples with different Y contents (see Fig 5.5), the sample with 5%Y show larger oxygen penetration depth. A larger oxygen penetration depth could be beneficial to the oxide film adherence to the substrate.

However, although yttrium was beneficial, excessive yttrium reduced its positive effect on the oxide film properties, evidenced by the poor performance of Mg-Al-5%Y (wt.%) observed during nano-indentation and scratch tests. Many studies also demonstrate that only a small amount of yttrium benefits passive films on various alloys [14, 112, 115]. The reason for degradation of the oxide film by excessive yttrium has not been fully understood yet. According to previous studies [116], adding 5%Y

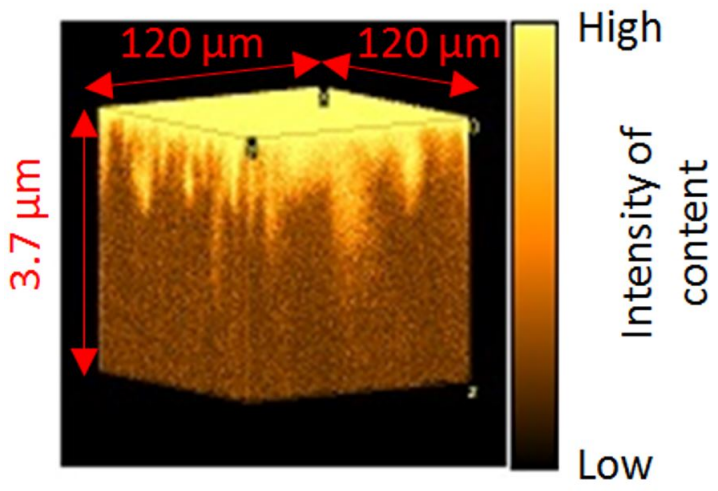

Figure 5.6: Representative 3D TOF-SIMS mapping of oxygen content in a Mg-3%Al-5%Y (wt.%) sample, which was exposed to air.

to Mg-3%Al (wt.%) resulted in densely distributed Al_2Y phase domains. The Al_2Y domains may have weaker bonding with the oxide film, thus reducing adherence of the oxide film and the resistance to scratching. This hypothesis has been computationally analyzed with first-principles calculations in the following section.

5.3.2 Surface Film Formed in Water

Effects of yttrium on the mechanical behavior of surface films on samples immersed in water are similar to those of films formed in air (see Fig 5.7). The scratch resistance of the surface film also increased with the yttrium addition as Fig 5.8 illustrates. The film on Mg-3%Al-3%Y (wt.%) was not damaged in the load range up to 2N. Thus, its ECR did not drop and only a straight orange line is shown in Fig 5.8. Corresponding electron work function increased with the yttrium addition as well (Fig 5.9), but the increase is smaller, compared to those of samples exposed to air (Fig 5.4).

Results of TOF-SIMS analysis for water-immersed samples (see Fig 5.10) are similar to those for the samples exposed to air. Intensities of MgO, MgOH and AlO all increased with increased yttrium content. The Y addition also lowered the OH/O ratio for surface films developed on the samples immersed in water. With respect to

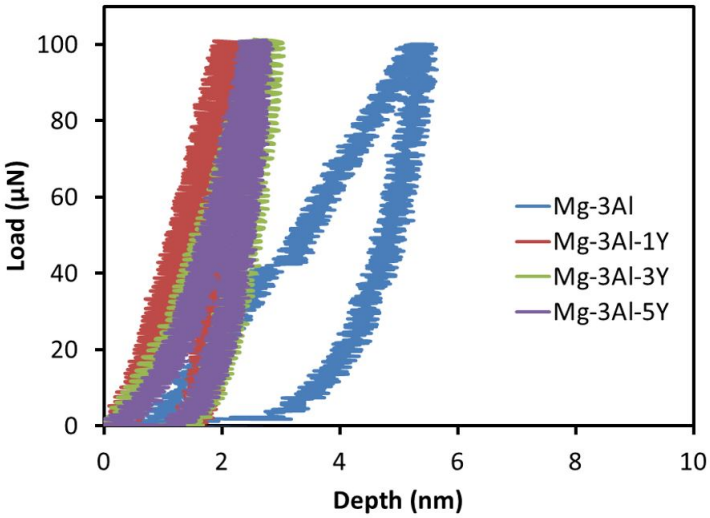

Figure 5.7: Nano-indentation loaddepth curves of water-immersed Mg-3%Al (wt.%) samples containing different amounts of Y.

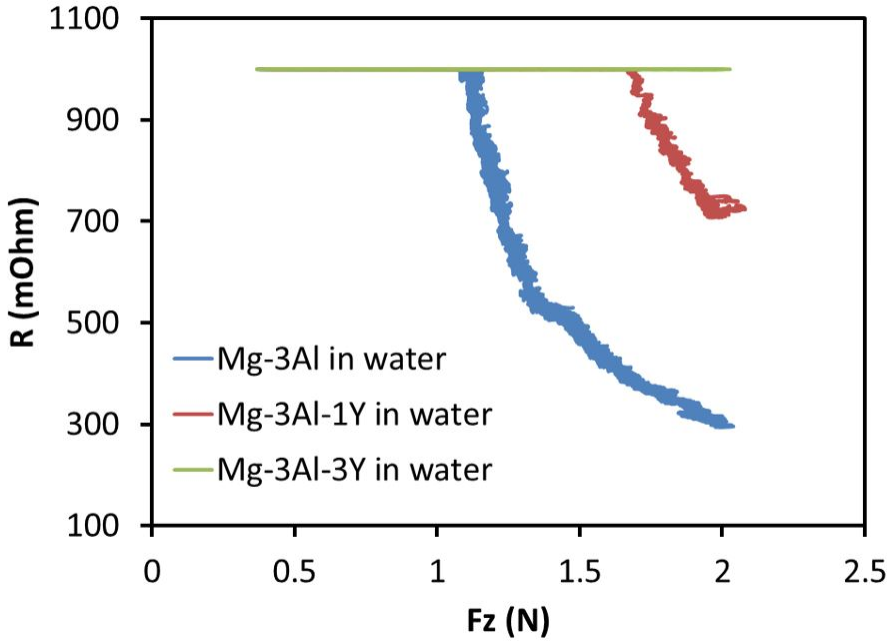

Figure 5.8: Changes in the electrical contact resistances of water-immersed Mg-3%Al (wt.%) samples containing different amounts of Y with respect to the normal load. The film on Mg-3%Al-3%Y (wt.%) was not damaged or scrated off in the load range up to 2N.Thus, its ECR did not drop and only a straight orange line is shown.

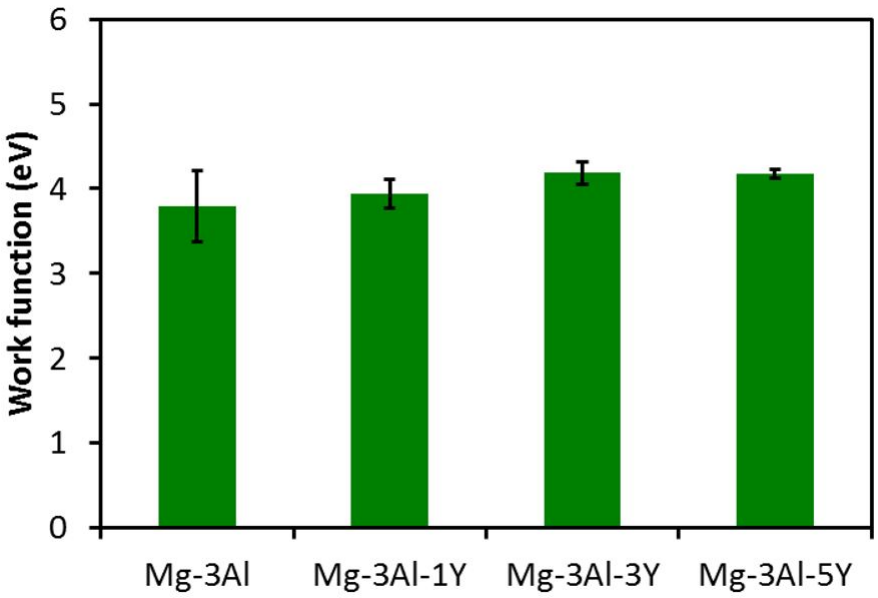

Figure 5.9: Electron work functions (EWF) of water-immersed Mg-3%Al-Y (wt.%) samples.

YO component, no meaningful signals were detected for the water-immersed samples. However, the effect of Y in reducing OH/O ratio is consistent with the observations by others, showing the beneficial effect of rare-earth elements on passivation of Mg-Al alloys with decreased degree of hydration [43].

The reduced OH/O ratio improved the strength and adherence of the film. The increase in the mechanical strength is ascribed to the fact that hardness of MgO (5.5 Mohs scale) is two-fold higher than that of $Mg(OH)_2$ (2.5 Mohs scale)[123]. Intrinsic mechanical properties of MgO such as elastic modulus and shear modulus are also superior to those of $Mg(OH)_2$ as demonstrated by first-principle calculations reported in the next section. Besides, since the density of MgO (3.6 gcm^{-3}) is greater than that of $Mg(OH)_2$ (2.37 gcm^{-3}), hydrolysis of the cubic magnesium oxide (MgO) to form hexagonal magnesium hydroxide ($Mg(OH)_2$) results in local volumetric changes, thus likely promoting formation of defects and rendering the oxide scale more micro-porous [124].

In addition, based on the TOF-SIMS analysis, Y appeared to promote the for-

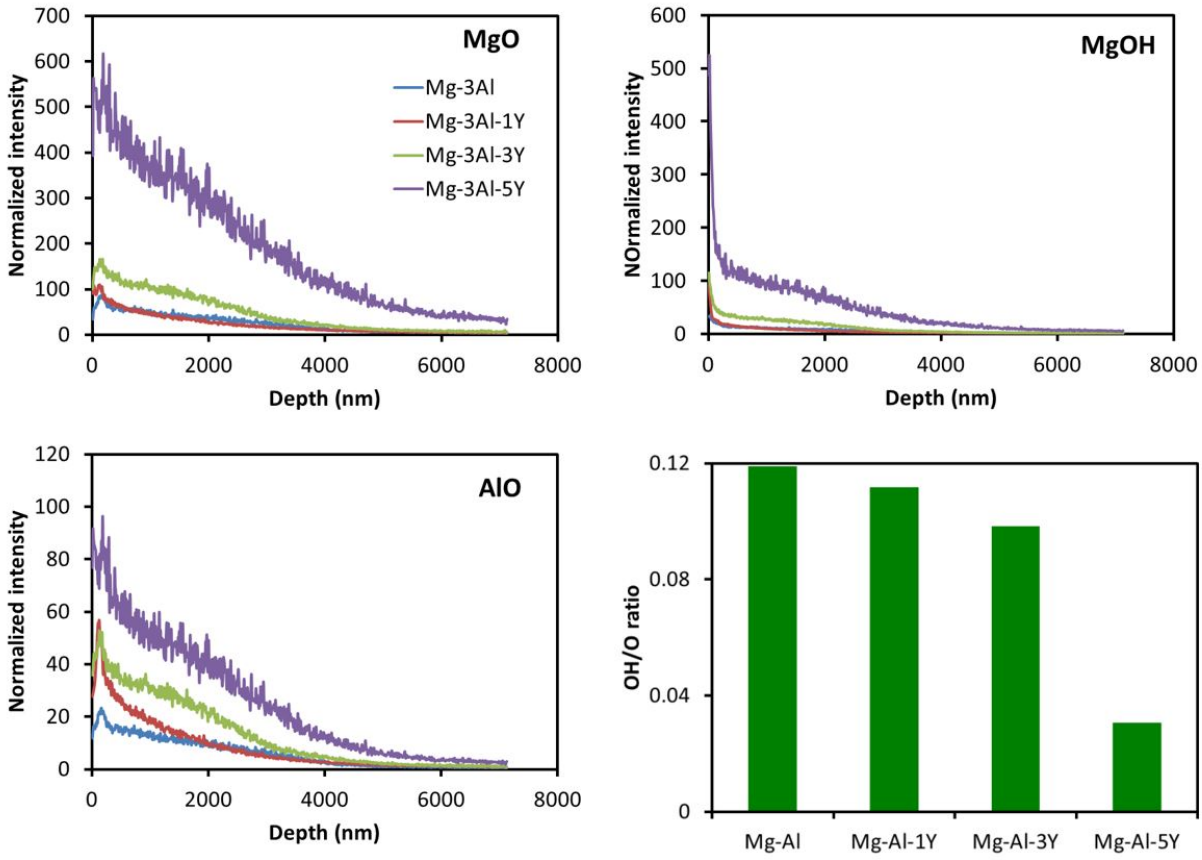

Figure 5.10: Results of TOF-SIMS analysis for water-immersed Mg-3%Al-Y (wt.%) samples: MgO, MgOH, AlO, and OH/O ratio.

mation of Al oxide (see Figs 5.5 and 5.10) and introduce some yttrium oxide, which should further strengthen the surface oxide film although the decrease in the ratio of Mg hydroxide to Mg oxide may play a major role due to the fact that the surface is dominated by magnesium components. The above-mentioned factors may explain why the films with lower OH/O ratios are much more elastic and harder. As for why the OH/O ratio can be lowered by yttrium, a possible mechanism is analyzed and discussed in next section.

5.4 First-Principles Calculations of Elastic Properties, OH/O Ratio and Interfacial Bonding

5.4.1 Elastic Properties of MgO and $Mg(OH)_2$ Components

First-principles calculations were employed to calculate elastic constants of MgO and $Mg(OH)_2$, two major components present in the surface films. All energy calculations were performed using the density functional theory implemented in the Vienna Ab initio Simulation Package [125, 126, 127] with projector-augmented wave (PAW) potential [128]. The generalized gradient approximation with the exchange-correlation functional of Perdew, Burke and Ernzerhof [129] was employed. Convergence tests indicated that 350 eV was a sufficient cutoff for PAW potential to achieve high precision in our system. K-points sampling using Monkhorst-Pack [130] for bulk structure optimization and using Gamma for supercell calculations. We found that a finer k-mesh was necessary for calculating the elastic constants. The electronic self-consistency was chosen as 10^{-5} eV per supercell for all the calculations.

Elastic constants can be used to evaluate the mechanical stability of a crystal. The elastic constants were calculated from the energy variation introduced by applying very small strains to the equilibrium lattice. For a given strain, all internal atomic coordinates were fully relaxed while keeping the deformed lattice fixed. The elastic energy, ΔE, of a crystal is expressed as [131]:

$$\Delta E \approx \frac{\Delta V_0}{2} \sum_{i,j=1}^{6} C_{ij} e_i e_j \tag{5.1}$$

where ΔV_0 is the volume of a undistorted crystal unit cell, the vector e=(e_1, e_2, e_3, e_4, e_5, e_6) represents the applied strain, and the coefficients $C_{i,j}$ are the elements in the elastic-constants matrix. ΔE and ΔV_0 were fitted with a quadratic polynomial to obtain the relevant elastic constants. A cubic crystal has three independent elastic constants, C_{11}, C_{12},... and C_{44}. For other crystals, such as hexagonal and orthorhombic, details can be found in previous studies [132].

If the elastic constants are determined, other mechanical quantities, such as bulk modulus (B), shear modulus (G), Youngs modulus (E) and Poisson ratio (ν), can be calculated using the Voigt approximation:

$$B = \frac{1}{9}(C_{11} + C_{12} + C_{33}) + \frac{2}{9}(C_{12} + C_{13} + C_{23}) \tag{5.2}$$

$$B = \frac{1}{15}(C_{11} + C_{22} + C_{33} - C_{12} - C_{13} - C_{23}) + \frac{1}{5}(C_{44} + C_{55} + C_{66}) \tag{5.3}$$

and from that:

$$E = \frac{9BG}{3B+G} \tag{5.4}$$

$$\nu = \frac{3B-2G}{2(3B+G)} \tag{5.5}$$

The bulk modulus represents the resistance of the material to uniform compression, the shear modulus represents the strength to resist plastic deformation, whereas a high (low) B/G value is associated with ductility (or brittleness) [133].

Based on cubic unit cell in MgO and triangle unit cell of $Mg(OH)_2$ (Fig 5.11), elastic constants of both MgO and $Mg(OH)_2$ were calculated. Results of the calculations are presented in Table 5.2, which show that MgO has a greater Youngs modulus,

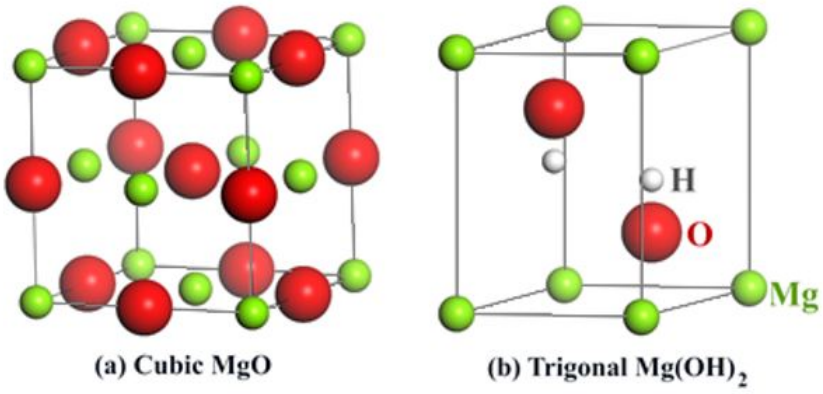

Figure 5.11: Unit cells for a) MgO and b) $Mg(OH)_2$.

Table 5.2: Bulk modulus (B), shear modulus (G), Youngs modulus (E) and Poisson ratio (ν) calculated for MgO and $Mg(OH)_2$ components.

	B (GPa)	G (GPa)	E (GPa)	ν	B/G
MgO	150.3	127.2	297.6	0.17	1.18
$Mg(OH)_2$	77.7	48.2	119.8	0.24	1.61

corresponding to stronger atomic bonding, than $Mg(OH)_2$. This confirms the experimental observation that the surface film on samples containing Y becomes stronger with a reduction in the OH/O ratio, showing higher resistances to indentation and scratching as Figs 5.2, 5.3, 5.7 and 5.8 illustrate.

5.4.2 Effects of Y on the interfacial bonding and OH/O ratio

As observed, the yttrium addition resulted in a decreased OH/O ratio, leading to improved surface films with higher adherence to the substrate. In order to understand the mechanisms for the OH/O ratio reduction and improvement in the film adherence to the substrate caused by yttrium, we analyzed affinities of Mg with and without dissolved Y atoms for MgO and $Mg(OH)_2$ components, respectively. The affinity is reflected by the Griffith work, which can be used to evaluate the binding strength and stability of interfaces. For instance, the Griffith work or energy to destroy an interface between MgO and Mg can be expressed as [134]:

Table 5.3: Calculated Griffith work for various systems.

	$MgO_{(}111)/Mg_{(}0001)$	$MgO_{(}111)/Mg_{(}0001)$ (Y)
Griffith work	2.762	2.974
	$Mg(OH)_{2\ (}001)/Mg_{(}0001)$	$Mg(OH)_{2\ (}001)/Mg_{(}0001)$ (Y)
Griffith work	2.422	2.596

$$W = -\frac{1}{S}(E_{(MgO/Mg)} - E_{(MgO/Vacuum)} - E_{(Mg-Vacuum)}) \tag{5.6}$$

where E(MgO/Mg) is the energy of the MgO/Mg supercell, E(MgO/Vacuum) and E(Mg/Vacuum) are energies of the film and Mg portions, respectively, after they are separated. S is the area of interface of the supercell. In the present calculation, the film and the substrate are oriented in such a way that the interfacial mismatch is the minimum, corresponding to the minimum interfacial strain. Fig 5.12 illustrates the constructed supercells in which 5 layers (two are Mg layers) of atoms close to the surface are fully relaxed, while other atoms are fixed. The same treatment was applied to the $Mg(OH)_2$-Mg system. Results of the calculation are presented in Table 5.3. As shown, the MgO-Mg interface has a higher Griffith work or energy than that of the $Mg(OH)_2$-Mg interface, which explains why the Y solute enhances the films adherence to the substrate when the OH/O ratio is decreased, in addition to the earlier-mentioned oxide pegging effect.

Regarding the reason why the Y addition reduced the OH/O ratio, as noted the Y solute increases the Griffith work of the MgO-Mg interface by 0.212 Jm^{-2} and that of $Mg(OH)_2$-Mg interface by 0.174 Jm^{-2}. The larger increase in the Griffith energy of the MgO-Mg interface by the Y solute, compared to that of $Mg(OH)_2$-Mg interface, is also an indication that the yttrium addition is more favourable for the formation of MgO. This may explain why the OH/O ratio is decreased by the Y addition.

One more issue that needs to be clarified is why excessive yttrium addition deteriorated the interfacial bonding. It was noticed that when the Y concentration increased, a second phase, Al_2Y, formed [116]. This phase may influence the inter-

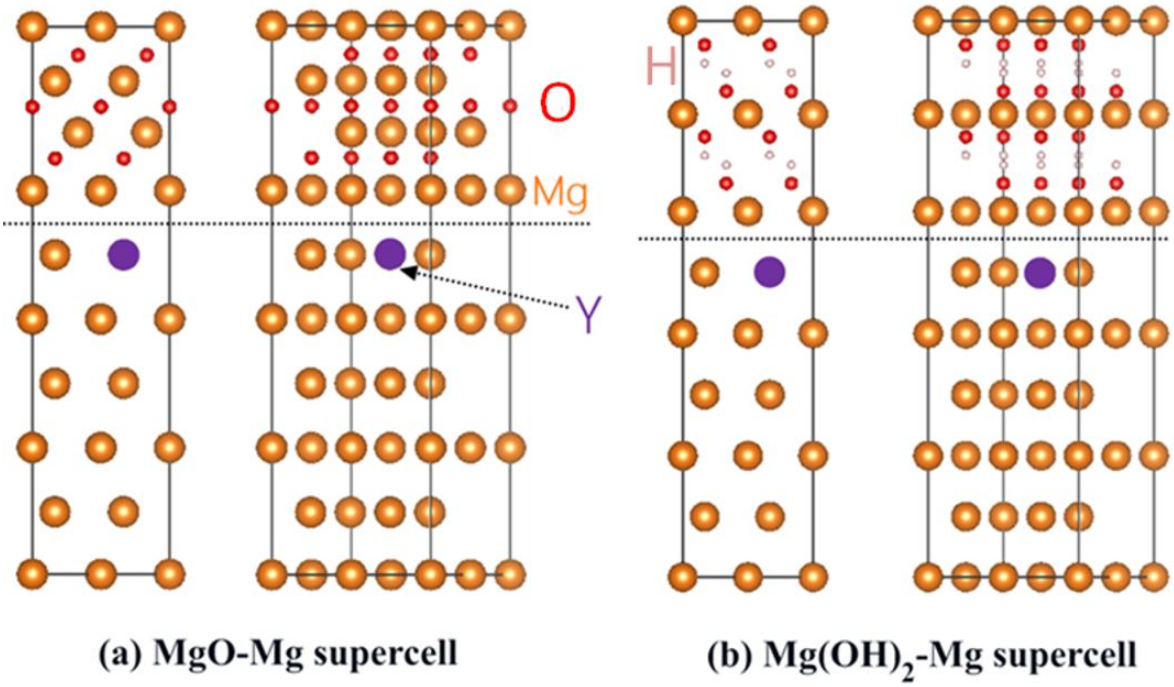

Figure 5.12: Supercells for calculating the Griffith work for MgO-Mg and $Mg(OH)_2$-Mg interfaces in presence of yttrium solute.

facial bonding, since the lattice mismatch between the films and Al_2Y is quite large, which may weaken the interfacial bonding. As shown in Table 5.4, for a one-to-one cell configuration, the mismatch between MgO(100) and Al_2Y(100) reaches 46%. For a two-to-one cell configuration, the mismatch is about 7%, which is still larger than that of MgO(110)-Mg(0001) interface (equal to 5.9%). Thus, when more Y was added to Mg-3%Al (wt.%) alloy, the surface coverage of formed Al_2Y domains increased and this would weaken the overall interfacial bonding, leading to a lower resistance to scratching.

Remark

According to the results presented in Chapter 3, Chapter 4, and Chapter 5, yttrium can improve both bulk properties and surface film properties of Mg-Al alloy against wear and corrosion.

Yttrium increases hardness, wear resistance, and corrosive wear resistance of the

Table 5.4: Interfacial lattice mismatch between the surface films and Al_2Y.

	Lattice mismatch	
Ineterface of MgO/Al_2Y	One-to-one cell mismatch	Two-to-one cell mismatch
MgO(100) Al_2Y(100)	46%	7%
MgO(111) Al_2Y(111)	46%	7%
MgO(110) Al_2Y(110)	46%	7%
MgO(110) Mg(0001)	5.9%	

bulk alloy. A few percentage of Y can also enhance corrosion resistance of the alloy by decreasing micro-galvanic cells in the microstructure.

Strength and adherence of the surface film to the alloy can be improved by addition of yttrium. These enhancements can suppress corrosion and provide some degree of protection against wear and corrosive wear.

5.5 Conclusions

The surface oxide film on Mg alloys plays an important role in resisting corrosion. Effects of yttrium addition on the strength and adherence of the oxide film on Mg-3%Al (wt.%) alloy developed in both ambient and aqueous environments were investigated experimentally and computationally. It was demonstrated that the yttrium addition reduced the OH/O ratio, which should be dominated by the ratio of $Mg(OH)_2$ to MgO in the surface oxide film, rendering it stronger and more stable. In addition to the improvement in the properties, yttrium also enhanced the adherence of the film to the substrate. However, adding too much yttrium (more than 3%) weakened the beneficial effects of Y on the surface oxide film with reduced adherence. Mechanisms responsible for the changes were analyzed and discussed.

Chapter 6

Y-incorporated Aluminization for Improved Tribological Properties

6.1 Introduction

One of the effective and inexpensive techniques is the application of a protective coating to achieve higher resistance to corrosion and other surface attacks on Mg alloys. Some protective coatings on Mg alloys have been investigated, such as chemical conversion coating, anodizing, and organic coating. Gray and Luan have reviewed techniques used for making coatings on Mg alloys [135]. One of the surface techniques, which receives considerable attention, is diffusion coating or surface modification by diffusing one or more protective elements into the substrate at elevated temperatures. Such modified surface layer has a few main advantages:

1. No interfacial debonding problem exists since there is not a distinguishable interface between the modified layer and the substrate.

2. Properties of the surface layer are adjustable through compositional control.

3. The process is flexible for integrating various properties not only wear and corrosion resistances but also physical properties, e.g., thermal and electrical conductivity, for specific applications.

More information about diffusion coatings on magnesium alloys can be found in

review articles, e.g., reference [30]. Among various diffusion treatment processes, aluminum pack cementation or aluminizing is an attractive one due to its lower cost and easy processing. Various attempts have also been made to improve the effectiveness of aluminizing against wear and corrosion. One of the approaches is to incorporate rare-earth elements into aluminized layers for enhanced passivation capability and durability [136, 137, 138, 139, 140, 141, 142].

The objective of this preliminary chapter is to investigate the effect of aluminizing with incorporated yttrium on corrosion, wear, and corrosive wear of AZ31 Mg alloy.

6.2 Experimental Procedure

Pure Magnesium rods (99.9%), pure Aluminum granules (99.9%) and pure Zinc powder (99.9%) with a weight ratio of %96, %3 and %1 were mixed and melted in an AGI induction furnace to make AZ31 alloy. To make the alloy homogenised, the ingot was re-melted four times (the ingot was turned over before each re-melting). Small disk-shape pieces were cut from the ingot, ground using SiC papers of up to 1200 mesh and cleaned in alcohol. The final step of polishing was performed on a dry-based mode in order to prevent reaction of the surface with water. The prepared disks were then aluminized. Pure Al powder (99.9%), Al_2O_3 powder to prevent sintering of the mixed powders, and NH_4Cl powder as activator were mixed and used for the aluminizing treatment. Pure yttrium (99.9%) powder was added to some of the Al-Al_2O_3-NH_4Cl mixtures for evaluating its influence on the performance of the aluminized surfaces. Table 6.1 shows different compositions of powder mixtures used for aluminizing AZ31 samples. The AZ31 disks were embedded in the powder mixtures in alumina crucibles, respectively, placed in an AIP vacuum furnace and heated at 420 °C for 10 hours. After cooling down in the furnace, the treated samples were pulled out from the furnace and cleaned by light brushing.

Hardness of the samples was measured using a ZHR8150BK Rockwell hardness tester (Zwick) under a load of 15Kgf using a quarter inch tungsten carbide ball. Each

Table 6.1: Different pack mixtures used in aluminizing of AZ31 sasmples.

Pack mixture	Al (wt%)	Al_2O_3 (wt%)	NH_4Cl (wt%)	Y (wt%)
Al	58.8	39.2	2	0
Al1Y	58.2	38.8	2	1
Al3Y	57	38	2	3
Al5Y	55.8	37.2	2	5

reported hardness value is an average of at least 3 measurements. Dry sliding and corrosive wear tests were performed at ambient temperature using a CSEM High-Temperature pin-on-disk apparatus in agreement with G99-05 ASTM Standard [80]. The pin was a Si_3N_4 ball with 3 mm in diameter and the sliding speed was 1 mm/s. The samples were tested under a load of 2 N for 2000 loops, corresponding to a sliding distance of about 12.58 m. Each wear test was repeated three times. The volume loss caused by wear was measured using a ZeGage Profilometer (Zygo). For corrosive wear tests, they were performed under the same testing conditions but in tap water (PH 6.3).

The corrosion behavior of the samples was evaluated by performing polarization tests using an electrochemical testing apparatus (PC4-750) made by Gamry Instruments Inc. A saturated calomel electrode (SCE) was used as the reference electrode, and a platinum plate (Pt) was used as the counter electrode. The corrosive medium was tap water (pH $\sim$ 6.3). The electrochemical tests were performed at room temperature and polarization curves were obtained for treated and untreated samples, respectively.

Microstructures of the samples were characterized using a Zeiss EVO MA 15 LaB_6 filament scanning electron microscope. Backscattered images were taken using a Si diode detector and EDS (Energy Dispersive Spectroscopy) acquired with a peltier-cooled 10 mm^2 Bruker Quantax 200 Silicon drift detector with 123 eV resolution.

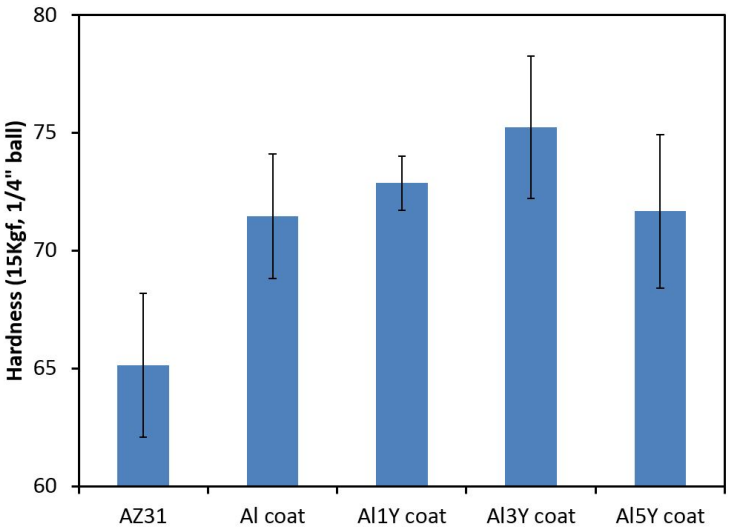

Figure 6.1: Rockwell hardness values of aluminized and non-treated AZ31 samples. Applied load: 15Kgf; Indenter: 1/4 inch WC ball.

6.3 Results and Discussion

6.3.1 Hardness and Wear

Figure 6.1 presents average surface hardness values of AZ31 samples aluminized with powders having different compositions. One may see that the aluminized samples show greater hardness values than the untreated sample. Volume losses of treated and untreated samples tested in dry sliding wear condition are shown in Figure 6.2. The figure demonstrates that the aluminizing treatment caused reduction in wear loss of the Mg alloy. Aluminizing with 1 wt% Y aluminum pack resulted in the maximum decrease in the volume loss.

Figure 6.3 compares the cross-sectional area of wear scars for AZ31 and the sample aluminized with Al1Y packing mixture. As shown, the treated sample has a smaller cross-section which supports the idea of a higher resistance to friction in this sample comparing to the original untreated AZ31 sample. Moreover, there is less accumulation of deformed material at the edges of the wear scars for the aluminized sample which is another sign for a higher capability against wear in this sample. According to Figure 6.4 the friction coefficients of the treated samples are lower than that of

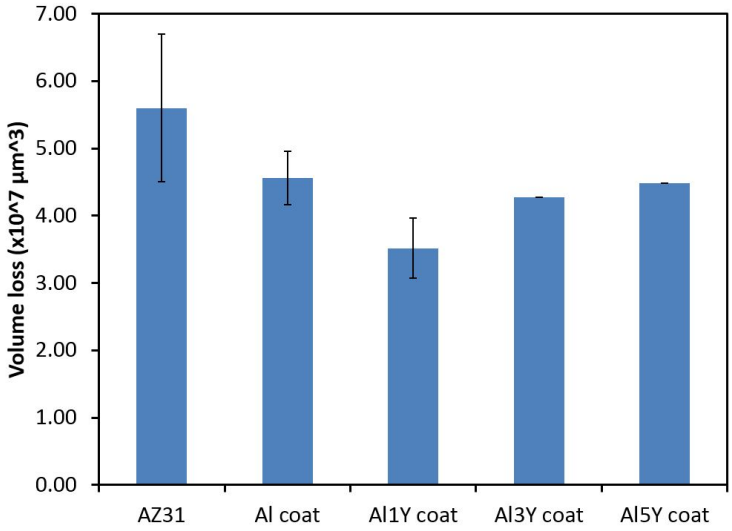

Figure 6.2: Volume losses of aluminized and bare AZ31 samples tested in dry sliding wear condition. Load: 2N; Speed: 1 m/s; Loop numbers: 2000; Radius: 1 mm; Pin: 3 mm Si_3N_4 ball.

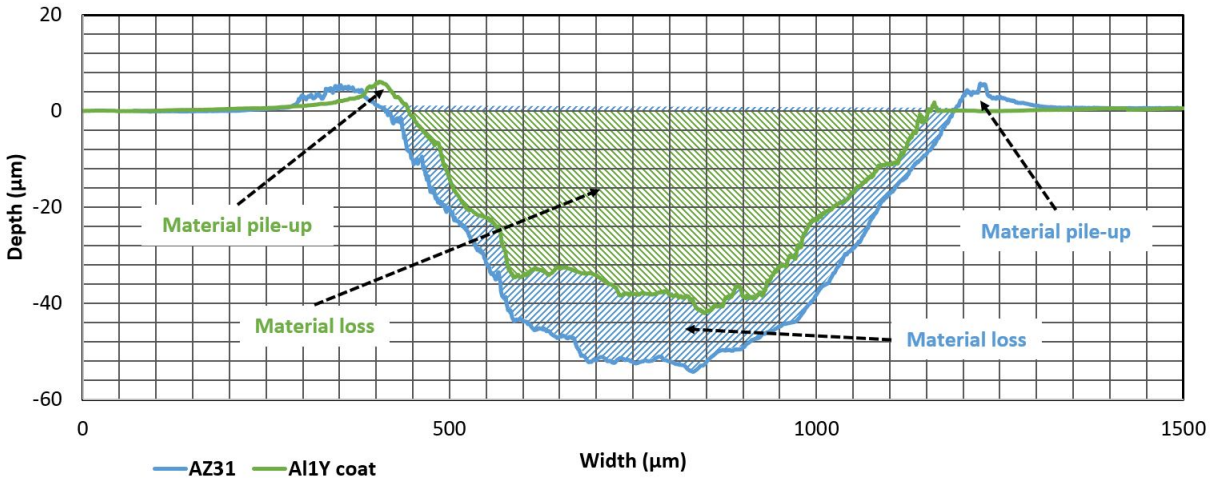

Figure 6.3: An illustration of the cross-sectional area of AZ31 and the sample treated with Al1Y packing mixture.

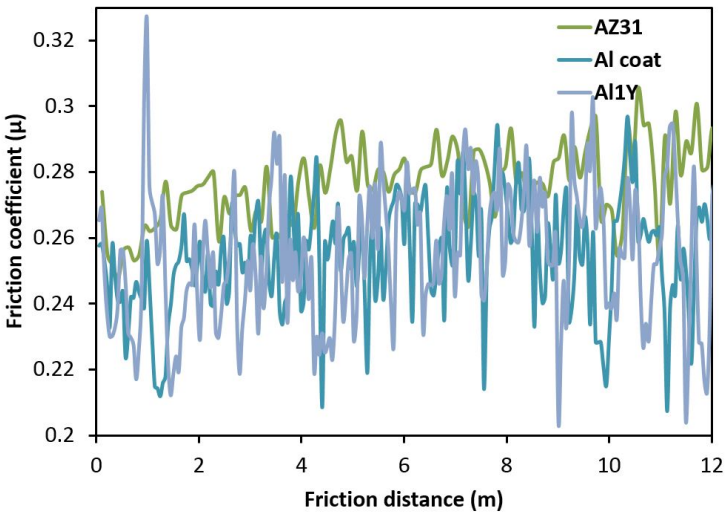

Figure 6.4: An illustration of the cross-sectional area of AZ31 and the sample treated with Al1Y packing mixture.

AZ31 sample implying a lower friction under normal loads, thus a lower material loss.

The increases in hardness and wear resistance should result from the increase in the fraction of intermetallic phases in the aluminized layer. Mg-Al and Al-Y intermetallic phases are harder than the Mg matrix [87, 143]. According to Mg-Al and Al-Y phase diagrams illustrated in Figure 5, when the surface of a Mg alloy is aluminized, the concentration of Al on the surface increases, resulting in an increased fraction of Mg_17Al_12 and thus higher hardness. When Y is added, formed Al_2Y phase is harder than Mg_17Al_12 [87]. It should be mentioned that Al is more competitive than Mg to attract yttrium and form Al_2Y [116]; thus yttrium can react with Al to form Al_2Y but unlikely forms Mg-Y phases when Al is present.

As shown, adding Y more than 3 wt% to the pack mixture reduced such benefits in terms of hardness and wear resistance. This decrease in the beneficial effect by adding overdosed rare-earth elements was also observed in previous studies, e.g., one on high-Cr cast irons with the incorporation of the rare-earth element [144]. The possible mechanism for the decline in the properties could be attributed to the bonding between the surface film and the alloy underneath. Excessive amount of yttrium may form a great amount of Al-Y second phase and loosen the bonding

between the surface oxide film and the alloy which in turn can decrease the corrosion resistance. More research is needed to make the mechanism clear.

Figure 6.6 illustrates SEM micrographs of worn surfaces of the aluminized and untreated AZ31 samples. In all cases, intensive plastic deformation and rough scars are signs of abrasive wear. These worn surfaces do not show a detectable difference in morphology.

6.3.2 Corrosion

Figure 6.7 illustrates polarization curves of treated and untreated samples in tap water. As presented, polarization curves clearly show the improvement in corrosion resistance of Y-incorporating aluminized samples. Aluminum is a passive element and its presence resulted in formation of a protective passive film (mainly Al_2O_3) that can stop continuous corrosion. Aluminizing clearly provides protection for the Mg alloy against corrosion reaction. Incorporation of yttrium led to considerably improved corrosion resistance of the aluminized layer. Based on the previous studies on the effect of Y on oxide scales formed at elevated temperatures [121], this oxygen-active element can strengthen the oxide film with additional component, Y_2O_3, and the adherence of the oxide film to the substrate is enhanced through inward growth of oxide with possible oxide pegging into or oxide keying into the grain boundaries. Figure 6.8 schematically illustrates how Al and Y could affect the surface passive film and the oxide pegging effect. However, the excessive amount of Y reduced the benefits on the performance of aluminizing treatment during corrosion tests (and corrosive wear tests as well, see next section). This has also been noticed in other studies [144, 145]. Further studies are needed in order to understand the mechanism behind.

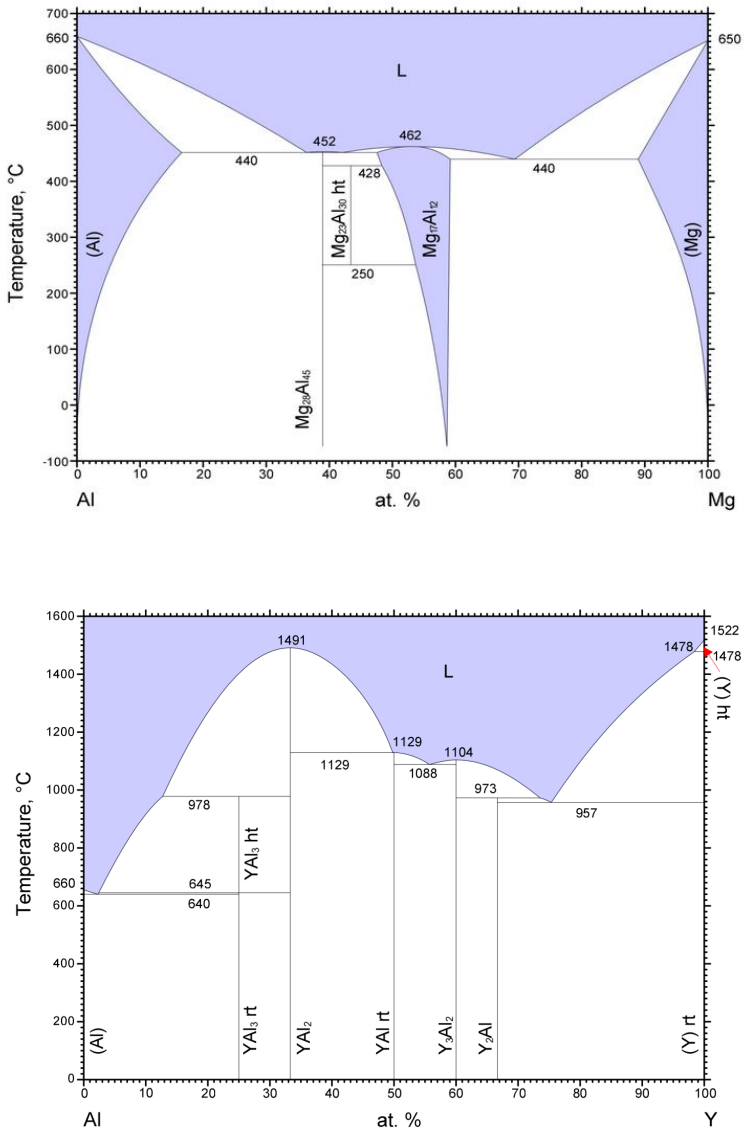

Figure 6.5: Mg-Al and Al-Y binary phase diagrams, adapted by ASM International (Zhong 2005) and (Kang et al. 2008) [20].

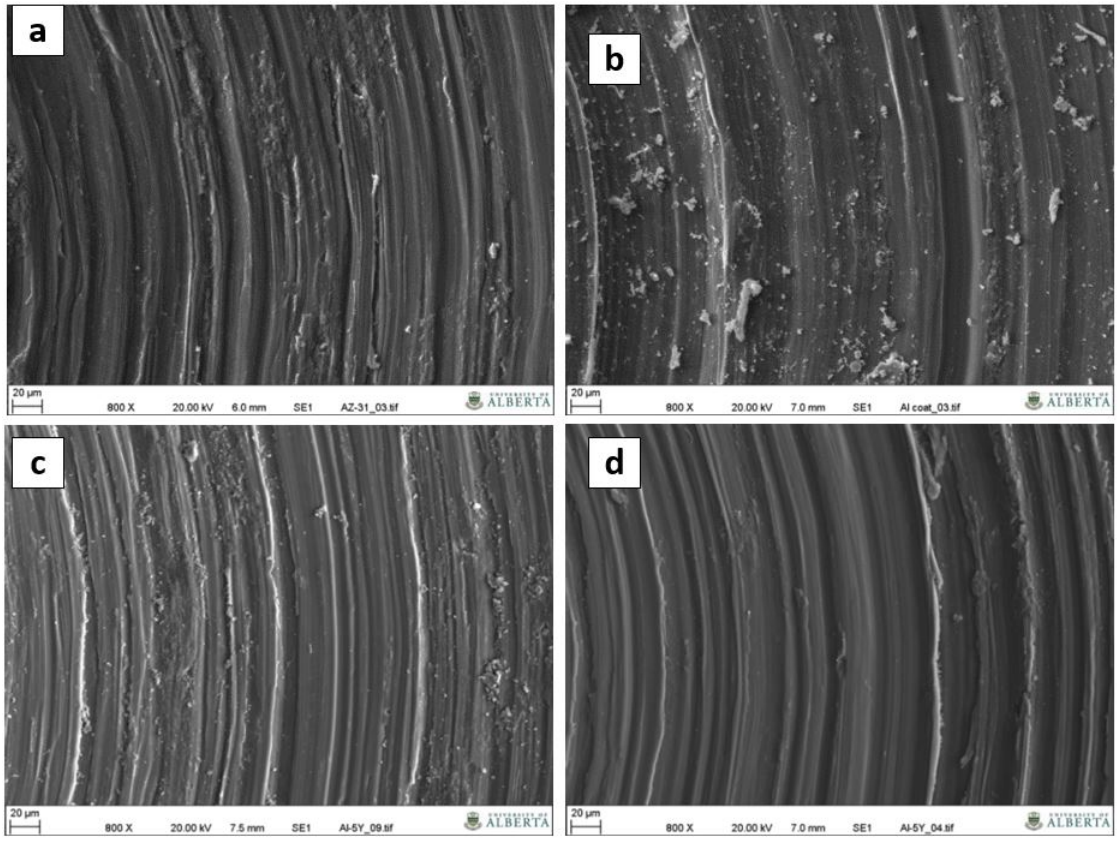

Figure 6.6: SEM images of worn surfaces: a) AZ31 alloy with no coating, b) Aluminized AZ31, c) 1 wt% Y-added aluminized AZ31 and d) 5 wt% Y-added aluminized AZ31.

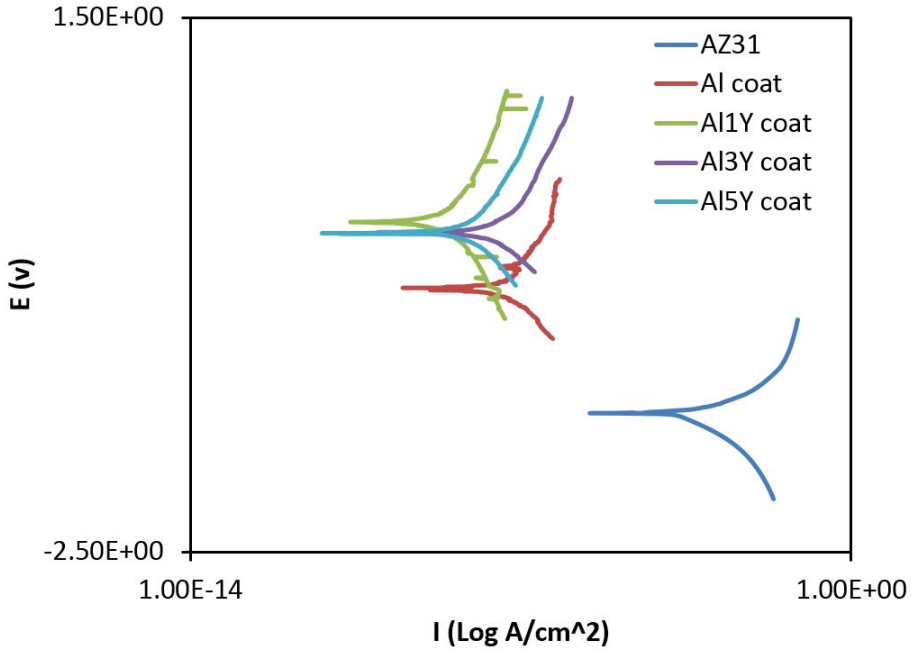

Figure 6.7: Polarization curves of aluminized and un-aluminized AZ31 samples. Corrosion environment is tap water.

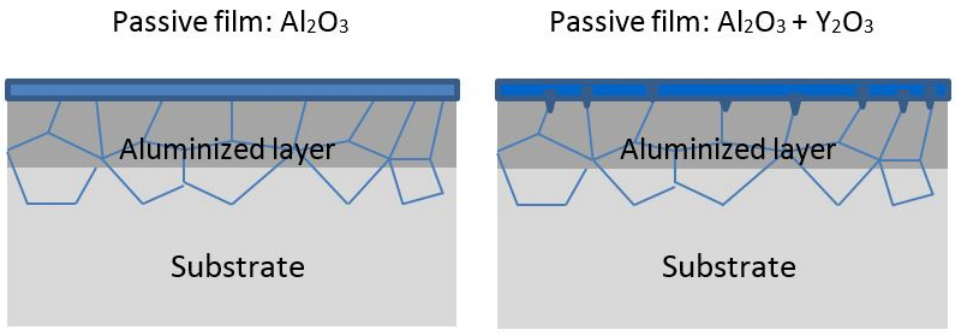

Figure 6.8: Schematic illustration of how Al and Y could affect the surface oxide film and the oxide pegging effect.

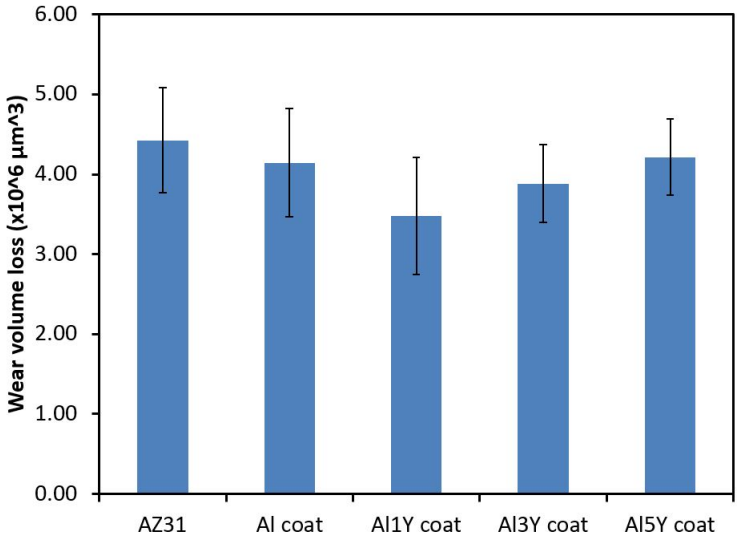

Figure 6.9: Volume losses of bare and aluminized AZ31 samples caused by wear in tap water. Load: 2N; Speed: 1 m/s; Loop numbers: 2000; Radius: 1 mm; Pin: 3 mm Si_3N_4 ball.

6.3.3 Corrosive wear

Effect of aluminizing on the corrosive wear of AZ31 alloy was investigated by performing sliding wear tests in a tap water environment. During corrosive wear test, wear and corrosion influenced the damage process synergistically. Figure 6.9 illustrates results of the corrosive wear tests, showing improvement in the corrosive wear resistance of AZ31 by aluminizing.

The addition of yttrium further enhanced the resistance to corrosive wear. The beneficial effect of yttrium is expected since the added Y increased the resistance to both wear and corrosion. 1 wt% Y in the coating mixture maximized the benefits which should be attributed to its maximum benefits to both corrosion and wear as demonstrated earlier. Adding larger amount of yttrium was not beneficial and volume loss of the sample with 5 wt% yttrium increased significantly.

During wear in water, plastic deformation and plowing grooves decreased as shown in Figure 6.10 (compared to those caused by dry wear shown in Figure 6) which illustrates SEM images of worn surfaces. On the worn surface of the bare AZ31

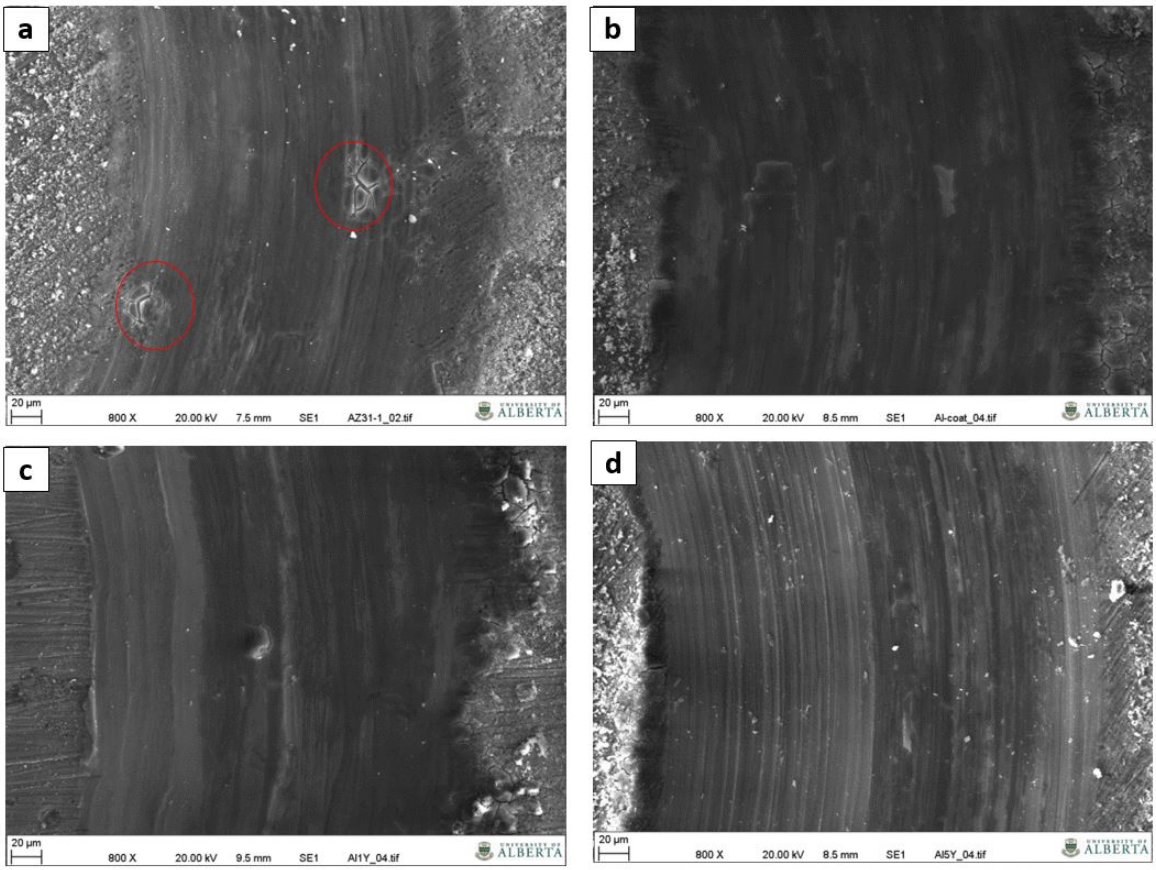

Figure 6.10: SEM images of worn surfaces caused by wear in tap water: a) AZ31 alloy with no coating, b) Aluminized AZ31, c) 1 wt% Y-added aluminized AZ31 and d) 5 wt% Y-added aluminized AZ31.

sample, cracks were observed which may result from corrosion-wear synergy or stress-corrosion cracking. No cracks were observed on the worn surfaces of the aluminized samples.

6.4 Conclusions

Effects of Y-containing aluminized coating on wear, corrosion, and corrosive wear of a magnesium alloy, AZ31, were investigated. The following conclusions are drawn:

1. Aluminizing raised hardness of AZ31 and decreased its dry sliding wear volume loss. Incorporating yttrium into the aluminized layer led to further improvement in hardness and wear resistance. 1 wt% Y resulted in maximum benefits.

2. Aluminizing considerably reduced the corrosion current of AZ31 in tap water and raised its corrosion potential. The addition of yttrium further reduced the corrosion rate improvement and 1 wt% Y led to the largest decrease in corrosion rate.

3. Aluminized AZ31 showed increased resistance to corrosive wear in water. The addition of yttrium further contributed to the improvement due to its beneficial effects on both corrosion resistance and wear resistance. Again, 1 wt% Y maximized the improvement.

Chapter 7

Maximizing the Benefit of Aluminization by Surface Nanocrystallization[1]

7.1 Introduction

High strength-to-weight ratio of magnesium makes Mg alloys very inviting for the automobile industry to develop fuel efficient and environmentally friendly vehicles. However, high chemical reactivity of magnesium largely limits its applications in various environments. Compared to aluminum alloys that are widely used in the transportation industry, magnesium alloys show lower strength and resistance to corrosion and wear.

Efforts have been made to improve the wear resistance of magnesium alloys through alloying with selected elements [75, 85, 87, 116, 146], making composites of Mg alloys with hard ceramic particles [147, 148, 149, 150, 151], developing special manufacturing processes [152, 153, 154, 155], surface modification using laser [156, 157, 158, 159], micro arc [160, 161, 162] and ion beam [163, 164], or coating techniques [165, 166, 167, 168]. Even though that research has developed some improvements in the wear resistance of magnesium alloys, when subjected to wear in corrosive environments, the improvement does not help much, since in this case both wear and corrosion resistances need to be enhanced in order to resist the synergistic

[1] A version of this chapter has been submitted as a peer-reviewed article to Tribology International

attack by wear and corrosion.

Aluminum has a higher electrochemical potential than magnesium due to its protective passive oxide film which makes Al alloys much more corrosion resistant than Mg alloys. For this reason, coating Mg alloys with Al or developing an Al-rich layer through diffusion has been a promising approach to make Mg alloys more resistant to oxidation. Previous studies reported in the literature proved the possibility of coating Mg alloys with Al employing pack powder diffusion [169, 170, 171, 172, 173, 174, 175, 176, 177, 178, 179, 180, 181, 182, 183], salt bath [184, 185, 186, 187, 188, 189], cold and hot spray [190, 191], and other coating processes [192, 193, 194, 195]. Such expected improvement in the corrosion resistance of Al-coated Mg alloys has been shown in some of the reported studies. However, very few studies [177, 183] were conducted to investigate the effect of Al coating on wear and corrosive wear of Mg alloys.

The objectives of this chapter are 1) to evaluate the effect of aluminizing on resistance of AZ31 alloy to wear and corrosive wear, and 2) to further improve the aluminized AZ31 alloy by surface nanocrystallization. Surface nanocrystallization has been demonstrated to be an effective process to enhance the corrosion resistance of passive materials through promoting atomic diffusion along high-density grain boundaries. The promoted diffusion helps reduce defects at the passive film/substrate interface and enhance oxide inward growth, resulting in faster passivation and a more protective passive film with stronger bonding with the substrate. Furthermore, refined grains increase the hardness, thus elevating the wear resistance [196, 197, 198]. It is thus expected that nanocrystallizing an aluminized Mg alloy surface would help maximizing its corrosion resistance and that to wear and corrosive wear.

7.2 Experimental Procedure

Pure Magnesium rods (99.9%), pure Aluminum granules (99.9%) and pure Zinc powder (99.9%) with a weight ratio of 96%, 3% and 1% were mixed and melted in an AGI

induction furnace to make AZ31 alloy. For homogeneity, the ingot was re-melted four times (the ingot was turned over before each re-melting). Small disk-shape pieces were cut from the ingot, ground using SiC papers of up to 1200 mesh and cleaned in alcohol.

The prepared disks were then aluminized using a pack aluminizing process. Pure Al powder (99.9%) and $AlCl_3$ activator powder were mixed to make a mixture of powders at a ratio of 95 wt.% to 5 wt.%, which was then used for the aluminizing treatment. The AZ31 disks were embedded in the powder mixture in alumina crucibles, which were sealed and heated at 600 °C in a Thermolyne tube furnace in an Argon atmosphere for 50 minutes. The furnace was then turned off and the samples were allowed to cool down in the furnace under the flow of Ar. After cooling, the treated samples were pulled out from the furnace and cleaned by light brushing and ultrasonic cleaning in alcohol. After cleaning the surface, some samples were repeatedly hammered for about 10 minutes using a roto-hammer (Robert Bosch Tool Corporation, USA) at a frequency of 50 Hz. The head of the hammer had a semi-spherical shape of 5 mm in diameter and was made of tool steel, which was much harder than both Al and AZ31. The impact energy of the hammering machine was 2.207 Nm. During the hammering process, the target surface was hammered homogenously over the entire sample surface. Fig 7.1 schematically illustrates the hammering process. After hammering, the sample was annealed at 250 °C in a Thermolyne tube furnace in an argon atmosphere for 40 minutes to develop nanocrystallized surface aluminized layer.

Mechanical properties of samples in different regions on the cross-section area were measured using a micro-indenter (Fischer Technology Inc.). The micro-indentation test was performed under a maximum load of 50 mN using a cone-shape diamond indenter tip and the distance between each of two regions was about 30 μm. Measurement was repeated at least three times for each region.

Dry sliding and corrosive wear tests were performed at ambient temperature using

a CSEM High Temperature pin-on-disk apparatus in agreement with G99-05 ASTM Standard [80]. The pin was a Si_3N_4 ball with 3 mm in diameter and the sliding speed was 1 mm/s. The samples were tested under a load of 2 N for 2000 loops, corresponding to a sliding distance of about 12.58 m. Each wear test was repeated for three times. The volume loss caused by wear was measured using a ZeGage profilometer (Zygo). For corrosive wear tests, they were performed under the same testing conditions but in a 3.5% NaCl solution.

The corrosion behavior of the samples was evaluated by performing polarization tests using an electrochemical testing apparatus (PC4-750) made by Gamry Instruments Inc. A saturated calomel electrode (SCE) was used as the reference electrode, and a platinum plate (Pt) was used as the counter electrode. The corrosive medium was 3.5 dilute NaCl solution which was made by dissolving 3.5% NaCl in distilled water. The electrochemical tests were performed at the room temperature and polarization curves were obtained for each sample.

Microstructures of the samples were characterized using a Zeiss EVO MA 15 LaB_6 filament scanning electron microscope. Backscattered images were taken using a Si diode detector and EDS (Energy Dispersive Spectroscopy) acquired with a peltier-cooled 10 mm^2 Bruker Quantax 200 Silicon drift detector with 123 eV resolution.

A Multimode 8 atomic force microscope (Bruker, US) was used in contact mode to determine the size of nano-sized grains in the aluminized layer. Before the AFM analysis, the hammered and annealed aluminized sample was sectioned and polished to a mirror-like surface using diamond suspensions, followed by etching using 0.5 % Nital solution.

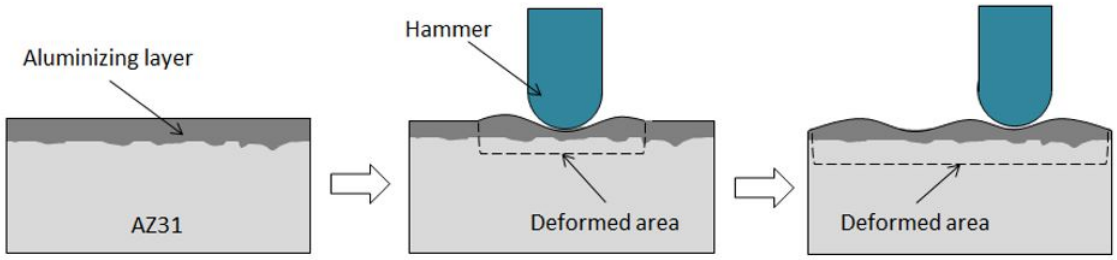

Figure 7.1: An schematic illustration of repeatedly hammering an aluminized sample.

7.3 Results and Discussion

7.3.1 Microstructure

Fig 7.2 presents a micrograph and a composition profile on the cross-section area of an aluminized sample. The line scan Energy-dispersive X-ray spectroscopy (EDS) analysis shows a gradual increase in Al content from inside the sample ($\approx$ 2.5 wt%) to its surface (more than 45 wt%). This increase in Al content occurred within a thickness of about 300 μm, which is approximately the thickness of the aluminized layer. As shown, there are some aluminum rich domains (point 2) in the top surface layer, which have a different composition from that of the matrix (for details see Table 7.1). Fig 7.3 demonstrates the cross-sectional view of the aluminized sample at a higher magnification. In the surface layer and also in the vicinity of the Al-rich phase, lamellar Mg-Al eutectic microstructure was observed. According to the Mg-Al binary phase diagram (Fig 7.4), the eutectic morphology is formed, consisting of Mg and β-$Mg_{17}Al_{12}$ phase. In most casting processes of making Mg-Al alloys containing more than 3 wt% Al, the cooling rate is low enough to cause Mg-Al eutectic microstructure. The eutectic microstructure may have different morphologies, depending on composition and cooling rate during casting. Alloys that have a composition closer to the eutectic composition (33 wt% Al) tend to exhibit lamellar morphologies, while those with aluminum content less than 10 wt% (e.g., AZ31) display partially or fully divorced eutectic morphologies [199, 200].

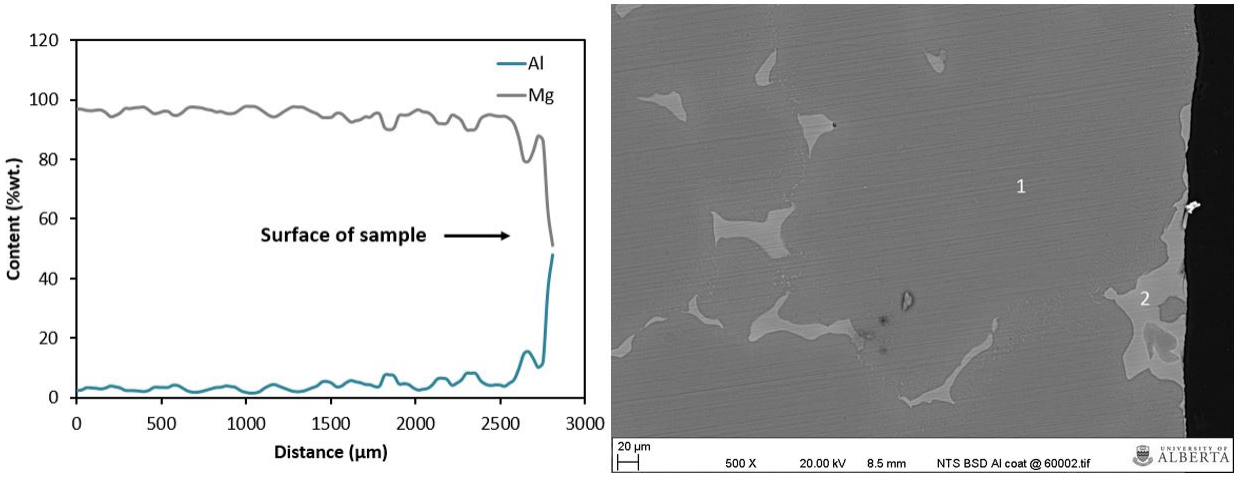

Figure 7.2: A line scan EDS analysis and a back scattered SEM picture of an aluminized sample.

Table 7.1: Point Energy-dispersive X-ray spectroscopy (EDS) analysis corresponing to Fig 7.2

Element	Point 1 (wt%)	Point 2 (wt%)
Magnesium	96.39	57.76
Aluminum	3.10	33.68
Zinc	0.51	8.56

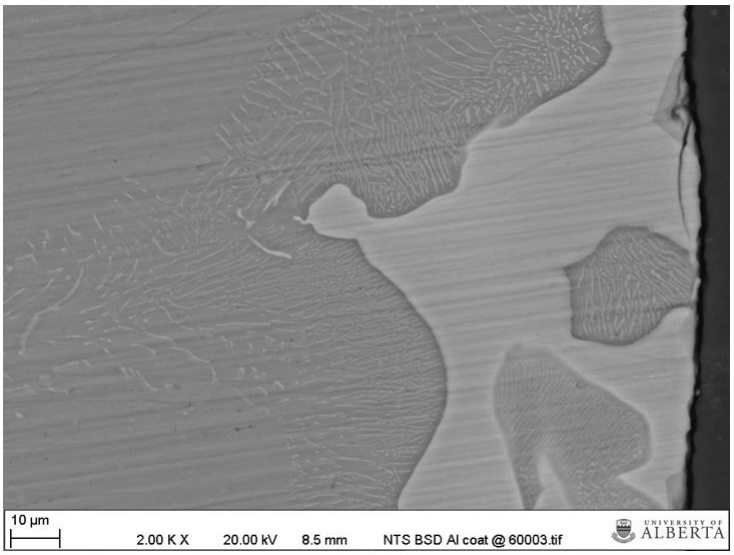

Figure 7.3: A micrograph image near the top surface of an aluminized sample taken with a higher magnification (x2000).

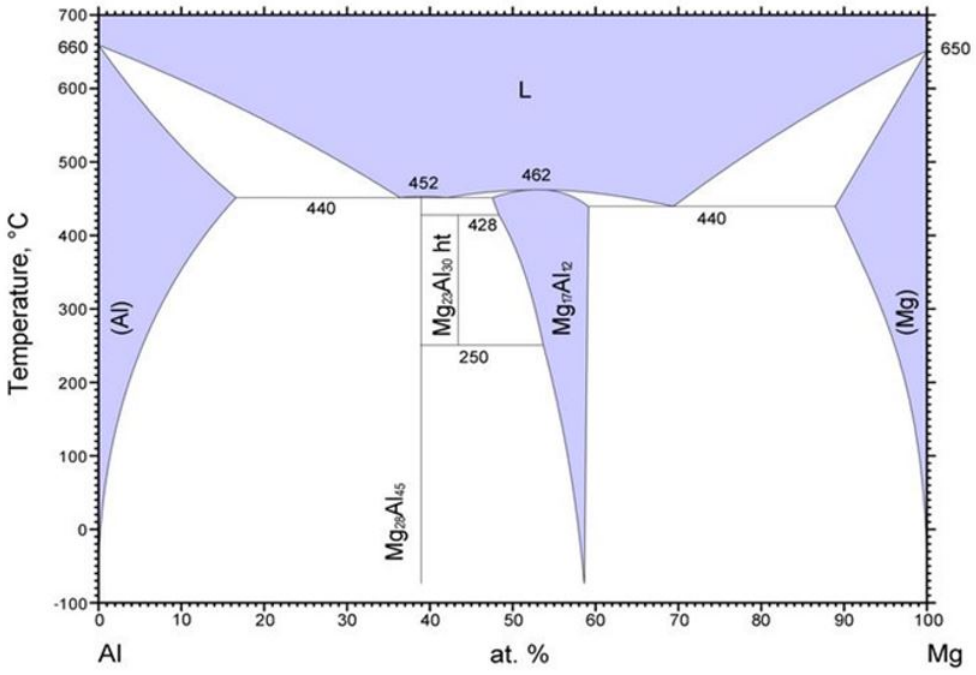

Figure 7.4: A Mg-Al binary phase diagram, adapted by ASM International (Zhong 2005).

Fig 7.5(a) represents a cross-sectional micrograph of an aluminized sample which was hammered followed by the heat treatment. Fig 7.5(b) shows an AFM topography image in the area very close to the top surface of the sample. The maximum grain size is about 260 nm, confirming that the surface layer has been nanocrystallized. The severe plastic deformation of the surface layer caused by hammering generated dislocation cells which were turned into nano-sized grains by the subsequent heat treatment. More details for such a surface nanocrystallization process can be found somewhere else [196, 201].

7.3.2 Hardness

Fig 7.6(a) presents the profiles of hardness versus distance from the top aluminized surface to inside of three samples, original (AZ31), aluminized, and aluminized with subsequent surface nanocrystallization. Corresponding load-depth indentation curves for their top surface layers are shown in Fig 7.6(b). As illustrated, the untreated AZ31

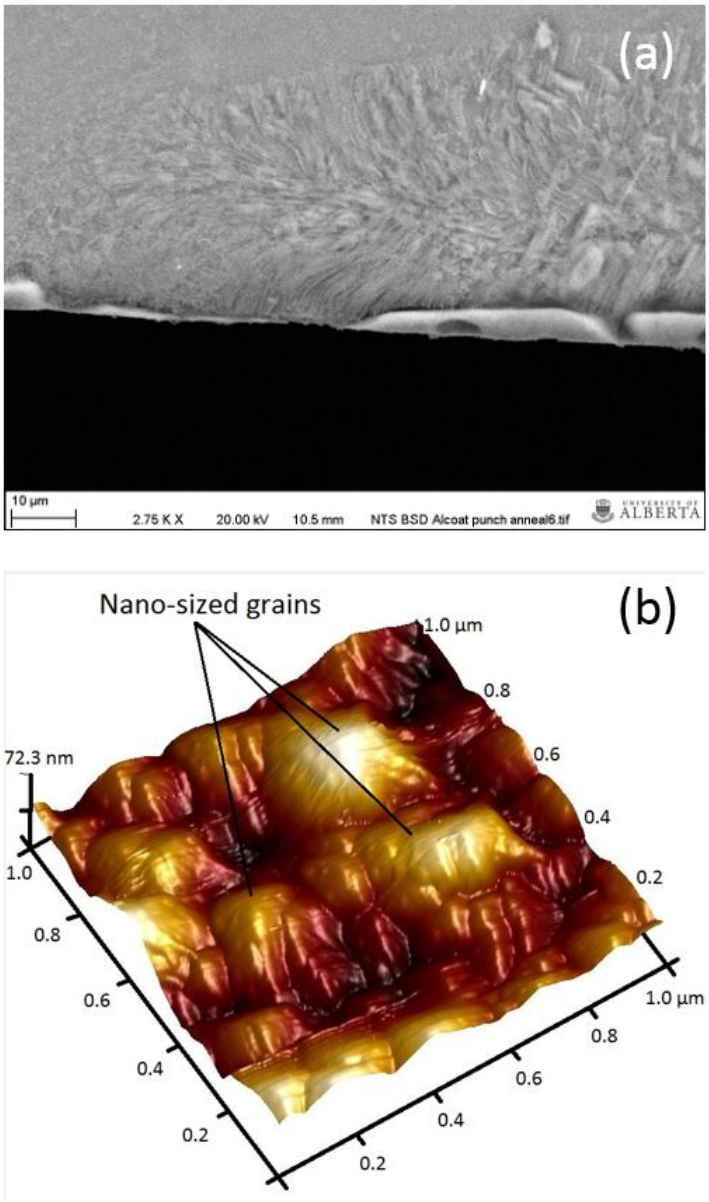

Figure 7.5: (a) A micrograph of the surface layer of an aluminized experienced surface nanocrystallization; (b) Corresponding AFM topographic image showing nano-sized structural features.

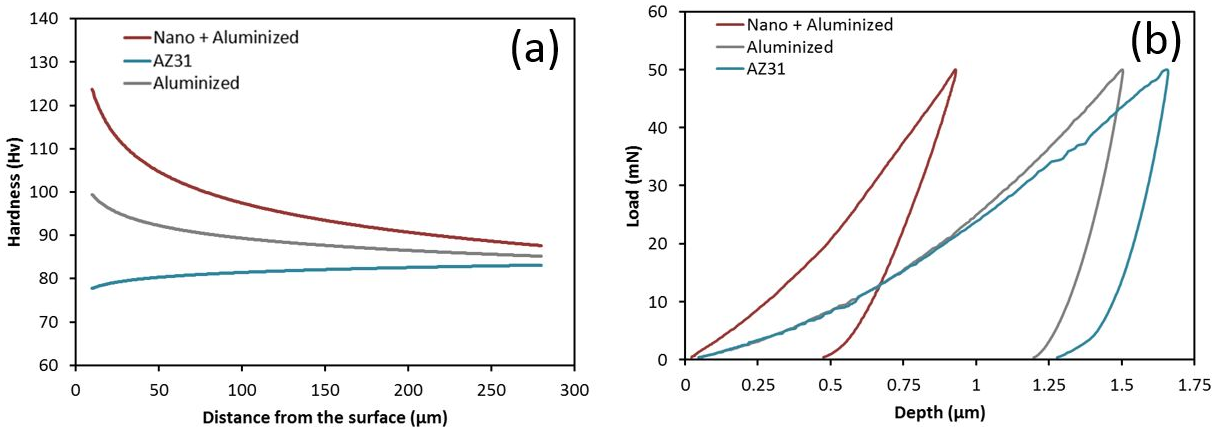

Figure 7.6: (a) Microhardness profiles of different samples versus the distance from the top surface. The deviation is typically within 15% based on the measurements (b)Load-depth indentation curves of top surface of the samples.

sample exhibits an approximately flat hardness line with no obvious changes. The aluminized sample, however, shows a greater hardness on the surface. The increase in hardness of the aluminizing layer results from the formation of Mg-Al(-Zn) phases [87, 187, 188], mainly $Mg_{17}Al_{12}$ phase in our case.

Nanocrystallization of the aluminizing layer further hardened the aluminized surface. The increment in the hardness is attributed to the formation of very fine grains, which follows the classical Hall-Petch relationship,

$$\sigma = \sigma_0 + Kd^{-\frac{1}{2}} \tag{7.1}$$

, where σ is the yield stress, σ_0 and K are material constants, and d is the grain diameter [202]. The equation is similarly applicable to hardness [203].

7.3.3 Corrosion Testing

Fig 7.7 presents polarization curves of samples tested in 3.5% NaCl solution. The curves show an enhancement in corrosion resistance of AZ31 by aluminizing. This improvement is attributed to the Al-rich surface, which brought in the passivation capability to the aluminized surface, leading to higher corrosion potential. The work function in the region close to the surface of the aluminized sample also increased as

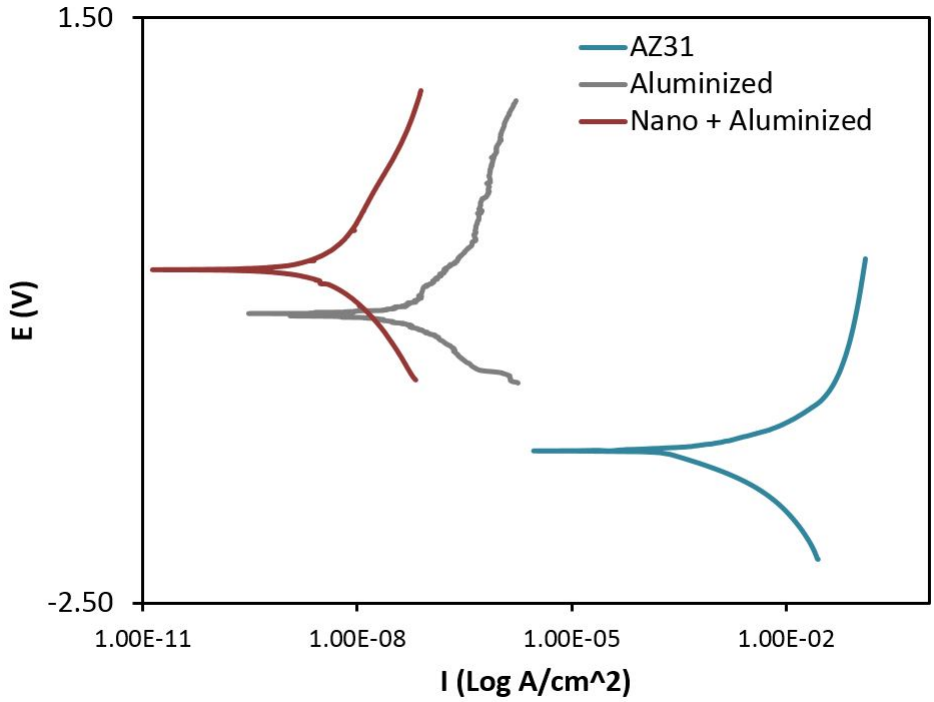

Figure 7.7: Polarization curves of untreated, aluminized and nanocrystallized aluminized samples in 3.5% NaCl solution.

Fig 7.8 illustrates, corresponding to a higher electrochemical stability and corrosion resistance.

It may need to be mentioned that more β-$Mg_{17}Al_{12}$ domains formed in the aluminized surface. It was expected that the presence of $Mg_{17}Al_{12}$ domains could lower the corrosion resistance of Mg-Al alloys due to galvanic reaction between the magnesium matrix and the $Mg_{17}Al_{12}$ phase, which is cathodic relative to the Mg matrix. However, the role of the $Mg_{17}Al_{12}$ phase may depend on its volume fraction and domain size. It is suggested that a high volume fraction of the β phase might act as a barrier to corrosion of the alloy [9, 36, 38]. Recent studies on Al reinforced by SiC nanoparticles [204] and Ni respectively reinforced by TiC microparticles and nanoparticles [205] demonstrate that the corrosion potential and electron work function, which is a measure of surface stability, increase by adding the nanoparticles. However, the microparticles showed an opposite effect. In the present case, there is a high fraction of β phase in the aluminized surface layer with a fine lamellar eutectic

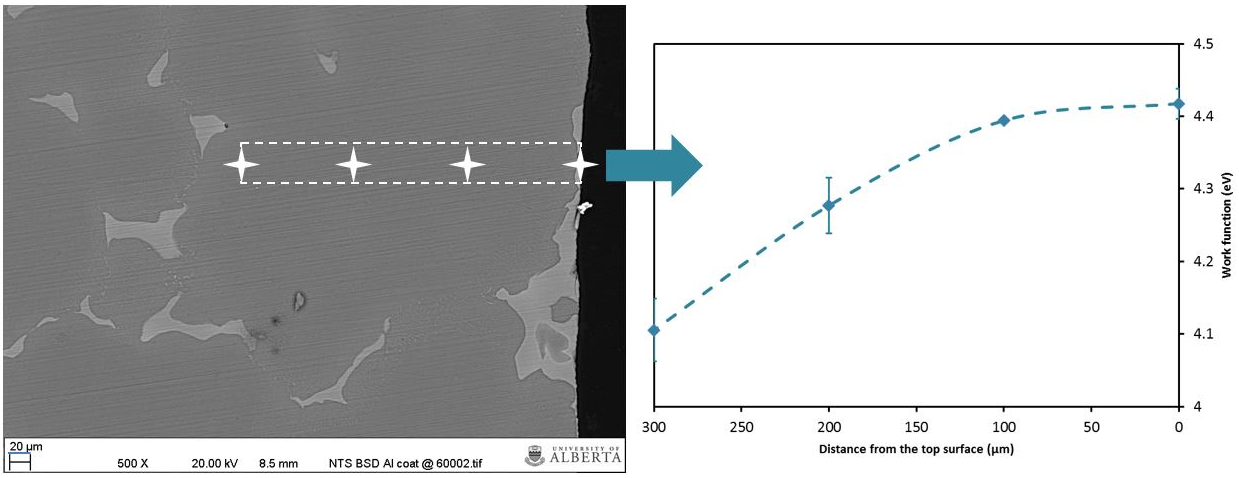

Figure 7.8: Work function measured in the vicinity of the aluminized surface of AZ31 alloy.

morphology (7.3) that could provide a corrosion barrier for the base alloy underneath [206]. More investigation on the role of β-$Mg_{17}Al_{12}$ phase on the corrosion behaviour of the aluminized Mg alloy is being carried out.

Hammering and annealing (recovery) further improved the effectiveness of aluminizing treatment with an elevated corrosion resistance. This improvement is the result of surface grain refinement, which enhanced the passivation capability due to accelerated atomistic diffusion as high-density grain boundaries. The faster diffusion also helped reduce the formation of defects, e.g., pores and micro-voids, at the interface between passive film and the substrate as well as inside the passive film. Besides, the existence of $Mg_{17}Al_{12}$ phase in a Mg alloy may promote nucleation of an oxide film, generating a thicker oxide film that lowers the corrosion rate [21, 48, 207]. By hammering and annealing the aluminized sample, the phase domains could be refined, thus enhancing the above-mentioned effect. One more benefit of surface nanocrystallization to the corrosion resistance of the aluminized AZ31 alloys is the effect of oxide pegging. High density of grain boundaries in the nanocrystallized surface may enhance inward growth of oxide film, leading to improved adherence of the passive film to the substrate [196, 197, 198].

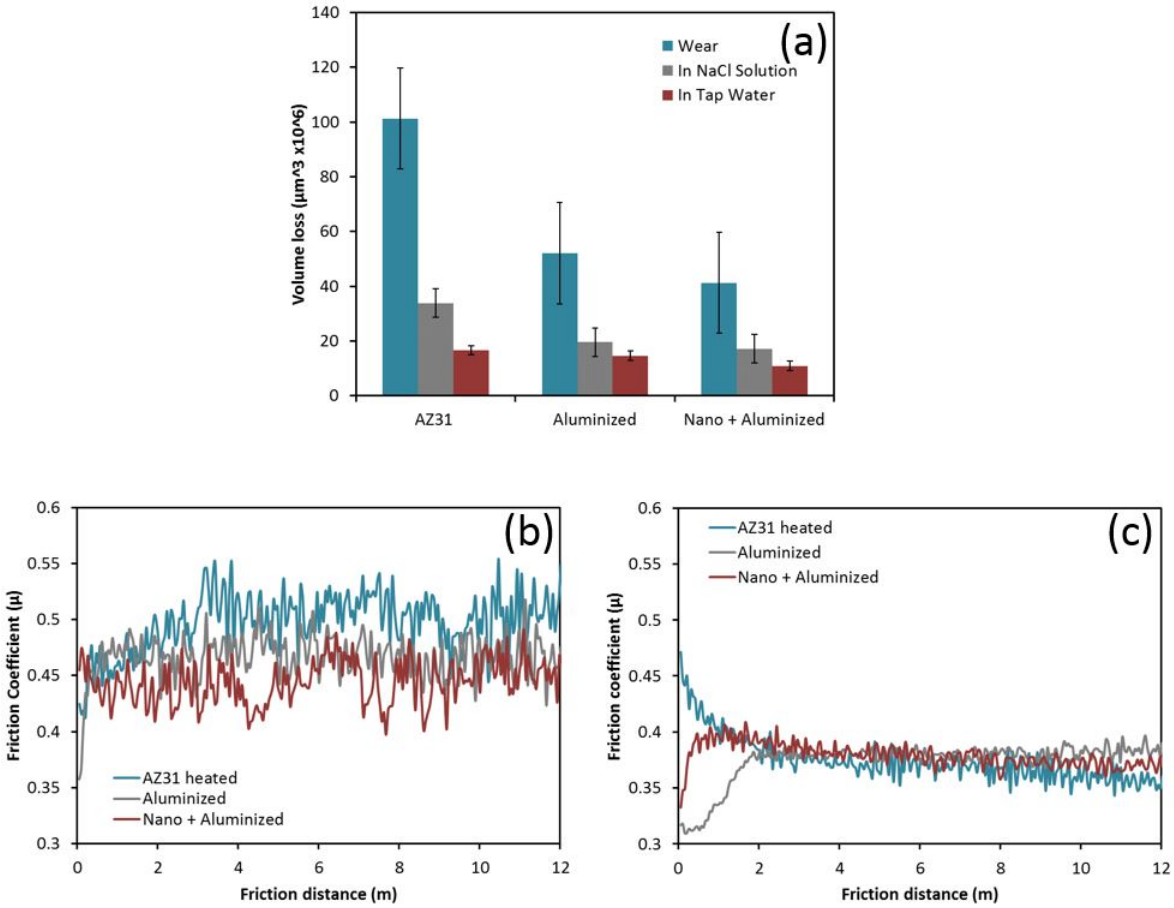

Figure 7.9: (a) Wear volume loss (in air) and corrosive wear volume loss (in 3.5% NaCl solution) of AZ31, aluminized and nanocrystallized aluminized samples; (b) Friction coefficient versus friction distance for samples worn in air; (c) Friction coefficient versus friction distance for samples worn in 3.5% NaCl solution.

7.3.4 Wear and Corrosive Wear

Fig 7.9(a) illustrates volume losses of AZ31 alloy, aluminized sample and, surface nanocrystallized aluminized sample caused by sliding wear in air, tap water, and in the 3.5% NaCl solution. As shown, aluminizing decreased the volume loss, which was further reduced by surface nanocrystallization.

Figure 7.10 illustrates cross-sectional profiles of wear tracks for AZ31, aluminized, and surface nanocrystallized aluminized samples, caused by dry wear. The profiles show that AZ31 sample has a larger cross-sectional area for the wear scar comparing to the two other samples. This denotes that the AZ31 sample has a larger wear scar

and, thus, more volume loss. In addition, more material pile-up was observed at the edges of the wear track for the AZ31 sample, indicating that more surface plastic deformation occurred in this sample during wear test which comes from its lower hardness. The aluminized sample with modified nanocrystallized surface showed the smallest cross-sectional area of wear track with the least material pile-up at the track edges. The cross-sectional profiles are consistent with the wear measurement.

The enhancement in dry wear resistance by aluminizing should be credited to increased hardness, mainly resulting from the formation of second phases such as β-$Mg_{17}Al_{12}$ [87, 187, 188]. Solid-solution hardening by Al should also play a role. The presence of β-$Mg_{17}Al_{12}$ phase and eutectic microstructure in the surface layer considerably hardened the surface layer, as shown in Fig 7.6, which benefited the wear resistance of the material. The hardened surface also helped reduce the contact area, thus leading to lowered friction as Fig 7.9(b) illustrates. A lowered friction coefficient is in turn beneficial to the wear resistance by reducing the tangential wearing force. The grain refinement by the surface nanocrystallization treatment further increased the surface hardness, rendering the surface more resistant to wear with further lowered coefficient of friction.

Fig 7.11 shows wear tracks on the samples. As illustrated, wear of the samples mainly resulted from ploughing, caused by abrasive wear. No significant difference in morphology of the wear track among the different samples was observed.

When tested in the solutions, as Fig 7.9 illustrates, aluminizing and surface nanocrystallization benefit the wear resistance of the Mg alloy in the dilute NaCl solution. With the aluminizing treatment, the introduced passivation capability, $Mg_{17}Al_{12}$ domains and solid-solution hardening enhanced the alloy with elevated resistance to corrosion and wear as well as to the synergy of corrosion and wear. When the aluminized surface was nanocrystallized by a combination of hammering and heat treatment, the surface was further improved with increased hardness, promoted passivation and the formation of a stronger and more adherent surface oxide film. These

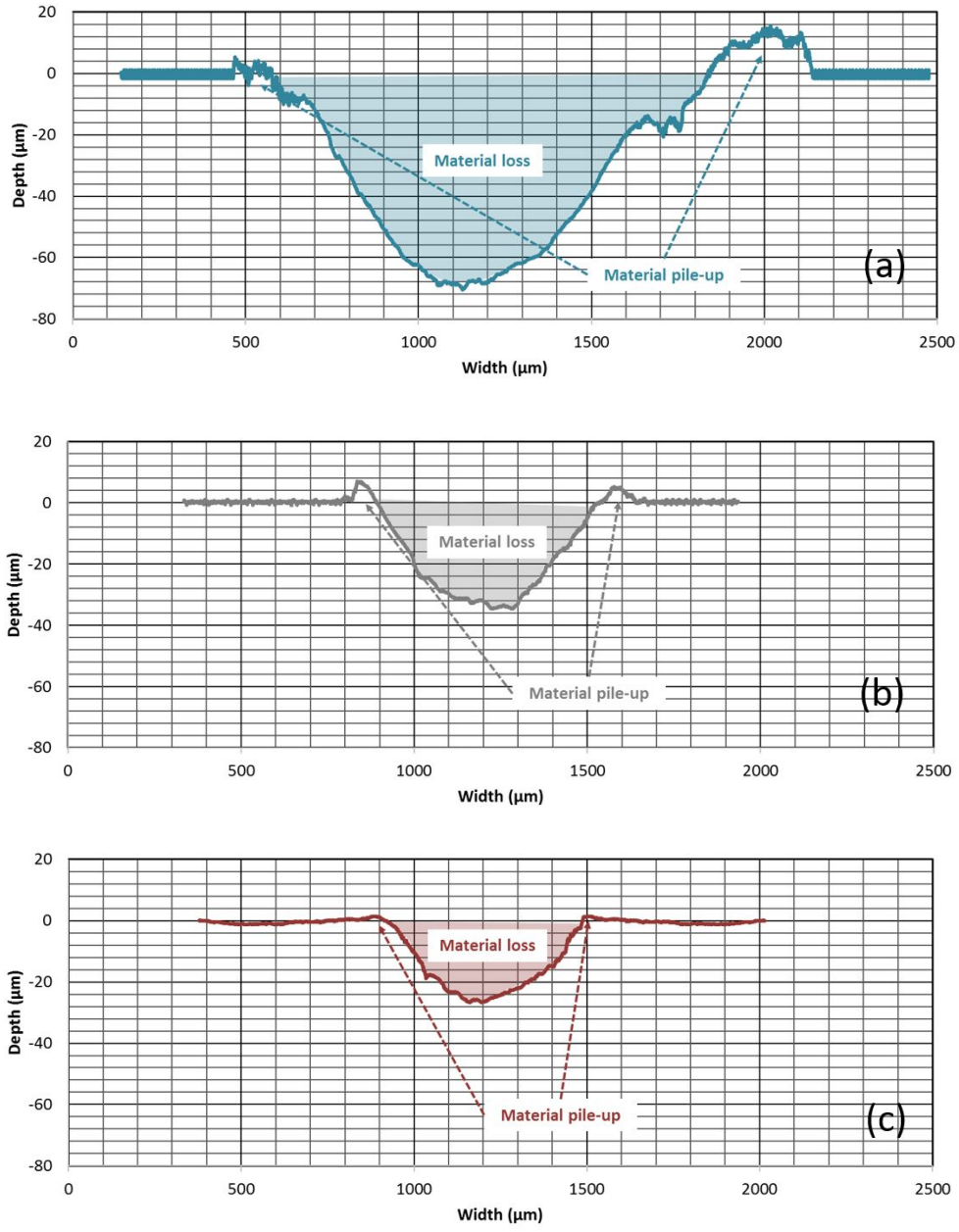

Figure 7.10: Cross-sectional profile of dry wear scars for: (a) AZ31, (b) Aluminized, and (c) nanocrystallized samples.

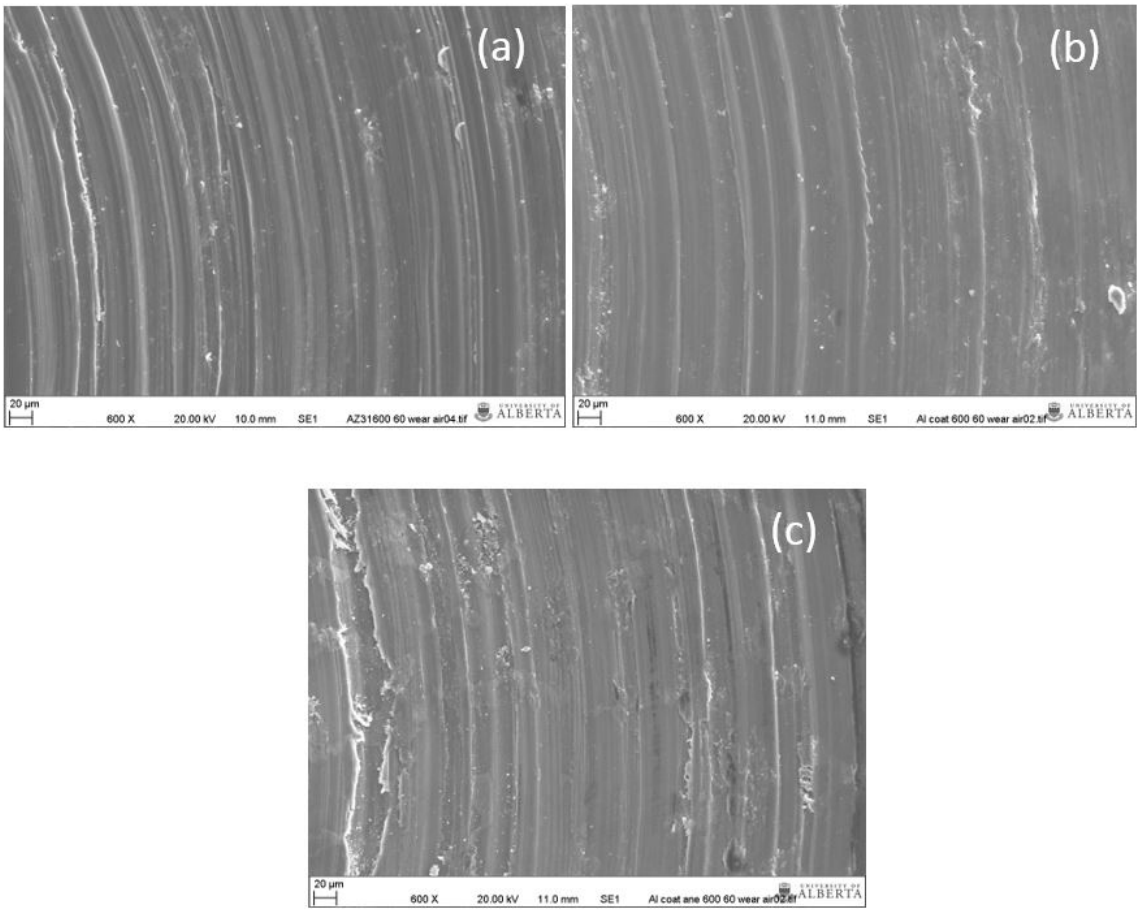

Figure 7.11: Wear tracks of samples. (a) AZ31, (b) Aluminized sample, and (c) nanocrystallized sample.

improvements further raised the resistance of the Mg alloy to corrosive wear. Since the dilute NaCl solution is more aggressive than tap water, the wear test in the NaCl solution caused larger volume losses than the tests in the tap water as illustrated in Figure 7.9(a). However, the trends or rankings of the samples under different testing conditions are similar.

It should be noted that in the wet environments, the volume losses are smaller than those caused by dry wear. This should be ascribed to the lubrication effect and the fact that the solutions may not result in strong wear-corrosion synergy, bearing in mind that the dilute NaCl solution and tap are not very corrosive media, although the former is relatively more aggressive than the latter. In addition, the coefficients of friction of the three surfaces did not show large difference, which should be due to the lubrication effect as well (e.g., see Figure 7.9(c)).

7.4 Conclusions

1. Aluminizing the surface of AZ31 alloy increased its resistance to corrosion, wear and corrosive wear by introducing passivation capability, hard β-$Mg_{17}Al_{12}$ phase and solid-solution hardened matrix.

2. The aluminized surface layer was nanocrystallized by repeated hammering and subsequent heat treatment. The hammering introduced severe plastic deformation and the recovery treatment turned dislocation cells into nano-sized grains with the maximum grain size around 260 nm.

3. The surface nanocrystallization further improved the resistance to corrosion, wear and corrosive wear. The improvements are attributed to the grain refinement, which resulted in increased hardness, stronger passivation capability and the formation of a more protective and adherent passive film. All the effects enhanced the Mg alloy against wear and synergistic attack of wear and corrosion.

Chapter 8

Conclusions and Future Work

8.1 Conclusions and Summary of Findings

A small amount of yttrium helped homogenize as-cast Mg-Al alloy, leading to minimization of $Mg_{17}Al_{12}$ phase and refined microstructure with more homogeneous element distributions. As the amount of added yttrium increased, Al_2Y phase became visible and its volume fraction increased, accompanied with increases in hardness and corresponding dry wear resistance. A small amount of yttrium ($\sim$ 1-2 wt%) enhanced the corrosion resistance of Mg-3 wt% Al in tap water and salt solution. The benefit of added yttrium decreased as the amount of added yttrium was further increased. The added yttrium reduced wear of the Mg alloy in tap water and salt solution with reduced oxide fragments, indicating that yttrium helped suppress corrosion-wear synergy. The combination of improved strength and corrosion resistance resulting from the Y addition can be the reason for the improved corrosive wear resistance of the material. It appears that the increase in the corrosive wear resistance of the Mg alloy with yttrium addition was mainly attributed to the increase in hardness and the corrosion may only play a minor role during corrosive wear in these mediums.

The surface oxide film on Mg alloys plays an important role in resisting corrosion. According to the experimental and computational results, in both ambient and aqueous environments, addition of yttrium reduced the OH/O ratio. This should be dominated mainly by reduction of the ratio of $Mg(OH)_2$ to MgO in the surface oxide

film which makes the film stronger and more stable. In addition to the improvement in the properties, yttrium also enhanced the adherence of the film to the substrate. In spite of that, adding excessive amount of yttrium (> 3 wt%) lessened the beneficial effects of Y on the surface oxide film with reduced adherence.

Aluminizing raised hardness of Mg-Al alloy and decreased its dry sliding wear volume loss. Incorporating yttrium into the aluminized layer led to further improvement in hardness and wear resistance. In addition, aluminizing considerably reduced the corrosion current of Mg-Al alloy in tap water and raised its corrosion potential. The improvement also was observed in corrosive wear properties of the alloy which is due to the beneficial effect of the process on both corrosion resistance and wear resistance. The enhancement in the properties is generated by expanded passivation capability, hard β-$Mg_{17}Al_{12}$ phase and solid-solution hardened matrix.

The aluminized surface layer was nanocrystallized by repeated hammering and subsequent recovery heat treatment. The hammering introduced severe plastic deformation and the heat treatment turned dislocation cells into nano-sized grains with the maximum grain size around 260 nm. The surface nanocrystallization further improved the resistance to corrosion, wear and corrosive wear. The improvements are attributed to the grain refinement which resulted in increased hardness and passivity and also formation of a more protective and adherent passive film. All the effects enhanced the Mg-Al alloy against wear and synergistic attack of wear and corrosion.

8.2 Suggested Topics for Future Work

1. Study the possibility of combining Y-incorporated aluminization with surface nanocrystallization to achieve further improvement in the properties.

2. More understanding of why 0.5-1 % of yttrium shows greater benefits in improving properties.

3. Understanding which of surface film or bulk properties are more important to

tribological and corrosion properties and the enhancement effects of yttrium is more beneficial to which of the bulk or film.

4. Optimizing diffusion parameters and pack mixture to achieve a consistent Y-incorporated aluminized layer on Mg alloys.

5. Study strength and adherence of the surface film formed on top of each micro-constituent.

6. Understanding the relation between local surface potentials and work function and corrosion behaviour of the alloy.

7. Apply other aluminization techniques that work at lower temperatures such as salt bath.

Bibliography

[1] Gerald Cole. Light Weighting the Automotive Industry - The Road to 2025 CAFÉ. In *3rd North Am. Automot. Light. Procure. Symp.*, pages 169–213, Detroit, 2015.

[2] US DOE. WORKSHOP REPORT: Light-Duty Vehicles Technical Requirements and Gaps for Lightweight and Propulsion Materials. Technical Report February, 2013.

[3] Alan A. Luo. Materials comparison and potential applications of magnesium in automobiles. In Suveen N. Mathaudhu, Alan A. Luo, Neale R. Neelameggham, Eric A. Nyberg, and Wim H. Sillekens, editors, *Essent. Readings Magnes. Technolgy*, pages 25–34. John Wiley & Sons, Inc., 2014.

[4] H Watarai. Trend of Research and Development for Magnesium Alloys - Reducing the Weight of Structural Materials in Motor Vehicles -. *Sci. Technol. trends*, Quarterly(18):84–97, 2004.

[5] Jae Joong Kim and Do Suck Han. Recent Development and Applications of Magnesium Alloys in the Hyundai and Kia Motors Corporation. *Mater. Trans.*, 49(5):894–897, 2008.

[6] K U Kainer, editor. *Magnesium Alloys and Technologies*. Wiley-VCH, 2003.

[7] Manoj Gupta and Nai Mui Ling Sharon. *Magnesium, Magnesium Alloys, & Magnesium Composites*. John Wiley & Sons, Inc., New Jersey, 2010.

[8] Edward Ghali. *Corrosion Resistance of Aluminum and Magnesium Alloys*. John Wiley & Sons, Inc., New Jersey, 2010.

[9] Gl L. Song and Andrej Atrens. Corrosion mechanisms of magnesium alloys. *Adv. Eng. Mater.*, 1(1):11–33, 1999.

[10] James E Hillis and Scott O Shook. Composition and Performance of an Improved Magnesium AS41 Alloy. In *SAE Tech. Pap.* SAE International, 1989.

[11] J H Nordlien, K Nisancioglu, S Ono, and N Masuko. Morphology and structure of oxide films formed on MgAl alloys by exposure to air and water. *J. Electrochem. Soc.*, 143(8):2564–2572, 1996.

[12] K. a. Unocic, H. H. Elsentriecy, M. P. Brady, H. M. Meyer, G. L. Song, M. Fayek, R. a. Meisner, and B. Davis. Transmission Electron Microscopy Study of Aqueous Film Formation and Evolution on Magnesium Alloys. *J. Electrochem. Soc.*, 161(6):C302–C311, apr 2014.

[13] M. Taheri, R. C. Phillips, J. R. Kish, and G. a. Botton. Analysis of the surface film formed on Mg by exposure to water using a FIB cross-section and STEM-EDS. *Corros. Sci.*, 59:222–228, 2012.

[14] M. Santamaria, F. Di Quarto, S. Zanna, and P. Marcus. Initial surface film on magnesium metal: A characterization by X-ray photoelectron spectroscopy (XPS) and photocurrent spectroscopy (PCS). *Electrochim. Acta*, 53:1315–1325, 2007.

[15] Iulian Radu, D.Y. Li, and R. Llewellyn. Tribological behavior of Stellite 21 modified with yttrium. *Wear*, 257(11):1154–1166, dec 2004.

[16] Hojat Ahmadi and Meisam Nouri. Beneficial effects of yttrium on mechanical failure and chemical stability of the passive film in 6061 aluminum alloy. *J. Mater. Sci.*, 45(13):3426–3432, 2010.

[17] Bharat Bhushan. *Intrucution to Tribology*. John Wiley & Sons, Inc., second edition, 2013.

[18] Friction and wear. In W.F. Gale and T.C. Totemeir, editors, *Smithells Met. Ref. B*. Elsevier, ASM International, eight edition, 2004.

[19] D. Y. Li. Corrosive Wear, 2013.

[20] ASM International. Alloy Phase Diagram Database, 2014.

[21] S. Feliu Jr, M. C. Merino, R. Arrabal, a. E. Coy, and E. Matykina. XPS study of the effect of aluminium on the atmospheric corrosion of the AZ31 magnesium alloy. *Surf. Interface Anal.*, 41(3):143–150, mar 2009.

[22] P Stasinopoulos and P Compston. *Sustainable Automotive Technologies 2013*. 2014.

[23] K.U. Kainer. Challenges for implementation of magnesium into more applications. In Alok Singh, Kiran Solanki, Michele V. Manuel, and Neale R. Neelameggham, editors, *Magnes. Technol. 2016*, pages 5–6. John Wiley & Sons, Inc., 2016.

[24] X. M. Wang, X. Q. Zeng, Y. Zhou, G. S. Wu, S. S. Yao, and Y. J. Lai. Early oxidation behaviors of Mg-Y alloys at high temperatures. *J. Alloys Compd.*, 460(1-2):368–374, 2008.

[25] G. L. Makar and J. Kruger. Corrosion of magnesium. *Int. Mater. Rev.*, 38(3):138–153, 1993.

[26] Norbert Hort, Yuanding Huong, and Karl Ulrich Kainer. Intermetallics in magnesium alloys. *Adv. Eng. Mater.*, 8(4):235–240, 2006.

[27] Helmut Kaufmann and Peter J. Uggowitzer. Fundamentals of the New Rheocasting process for magnesium alloys. *Adv. Eng. Mater.*, 3(12):963–967, 2001.

[28] C Blawert, N Hort, and K U Kainer. Automotive Applications of Magnesium and Its Alloys. *Trans. Indian Inst. Met.*, 57(4):397–408, 2006.

[29] Z. Pu, G. L. Song, S. Yang, J. C. Outeiro, O. W. Dillon, D. A. Puleo, and I. S. Jawahir. Grain refined and basal textured surface produced by burnishing for improved corrosion performance of AZ31B Mg alloy. *Corros. Sci.*, 57:192–201, 2012.

[30] Cheng Zhong, Fan Liu, Yating Wu, Jingjing Le, Lei Liu, Meifeng He, Jiacai Zhu, and Wenbin Hu. Protective diffusion coatings on magnesium alloys: A review of recent developments. *J. Alloys Compd.*, 520:11–21, apr 2012.

[31] R. Arrabal, a. Pardo, M. C. Merino, M. Mohedano, P. Casajús, K. Paucar, and G. Garcés. Effect of Nd on the corrosion behaviour of AM50 and AZ91D magnesium alloys in 3.5wt.% NaCl solution. *Corros. Sci.*, 55:301–312, 2012.

[32] US DOE. Workshop Report: Trucks and Heavy Duty Vehicles Technical Requirements and Gaps for Lightweight and Propulsion Materials. Technical Report February, 2013.

[33] F. Zivić, N. Grujović, G. Manivasagam, C. Richard, J. Landoulsi, and V. Petrović. The potential of magnesium alloys as bioabsorbable / biodegradable implants for biomedical applications. *Tribol. Ind.*, 36(1):67–73, 2014.

[34] Horst E. Friedrich and Barry L. Mordike. *Magnesium technology: Metallurgy, design data, applications*. Springer Berlin Heidelberg, 2006.

[35] D Eliezer and H Alves. Corrosion and Oxidation of Magnesium Alloys. In Myer Kutz, editor, *Handb. Mater. Sel.*, pages 267–291. John Wiley & Sons, Inc., New York, 2002.

[36] G. Song and a. Atrens. Understanding Magnesium CorrosionA Framework for Improved Alloy Performance. *Adv. Eng. Mater.*, 5(12):837–858, dec 2003.

[37] Edward Ghali, Wolfgang Dietzel, and Karl-Ulrich Kainer. General and Localized Corrosion of Magnesium Alloys: A Critical Review. *J. Mater. Eng. Perform.*, 13(1):7–23, feb 2004.

[38] Rong-chang Chang Zeng, Jin Zhang, Wei-jiu Jiu Huang, W. Dietzel, K.U. U. Kainer, C. Blawert, and Wei Ke. Review of studies on corrosion of magnesium alloys. *Trans. Nonferrous Met. Soc. China*, 16(SUPPL. 2):s763–s771, jun 2006.

[39] Chunhua Xu and Wei Gao. Pilling-Bedworth ratio for oxidation of alloys. *Mater. Res. Innov.*, 3(4):231–235, 2000.

[40] Khaled M. Ismail and Sannakaisa Virtanen. Electrochemical Behavior of Magnesium Alloy AZ31 in 0.5MKOH Solution. *Electrochem. Solid-State Lett.*, 10(3):C9, 2007.

[41] Jan Halvor Nordlien, Sachiko Ono, Noburo Masuko, and Kemal Nisancioglu. Morphology and structure of oxide films formed on magnesium by exposure to air and water. *J. Electrochem. Soc.*, 142(10):3320–3322, 1995.

[42] J.H. Nordlien, S. Ono, N. Masuko, and K. Nisancioglu. A TEM investigation of naturally formed oxide films on pure magnesium. *Corros. Sci.*, 39(8):1397–1414, aug 1997.

[43] Noburo Nordlien, Jan Halvor, Nisancioglu, Kemal, Ono, Scachiko, Masuko. Morphology and Structure of Oxide Films Formed on MgAl Alloys by Exposure to Air and Water. *J. Electrochem. Soc.*, 144(2):461–466, 1997.

[44] Nobuyoshi Hara, Yasuhiro Kobayashi, Daisuke Kagaya, and Noboru Akao. Formation and breakdown of surface films on magnesium and its alloys in aqueous solutions. *Corros. Sci.*, 49(1):166–175, jan 2007.

[45] E Ghali. Activity and passivity of magnesium (Mg) and its alloys. In Guang-

ling Song, editor, *Corros. Magnes. Alloy.*, chapter 2, pages 66–90. Woodhead Publishing Limited, first edition, 2011.

[46] Ming Liu, Sandrine Zanna, Helene Ardelean, Isabelle Frateur, Patrik Schmutz, Guangling Song, Andrej Atrens, and Philippe Marcus. A first quantitative XPS study of the surface films formed, by exposure to water, on Mg and on the MgAl intermetallics: Al3Mg2 and Mg17Al12. *Corros. Sci.*, 51(5):1115–1127, may 2009.

[47] M. P. Brady, M. Fayek, H. H. Elsentriecy, K. a. Unocic, L. M. Anovitz, J. R. Keiser, G. L. Song, and B. Davis. Tracer Film Growth Study of Hydrogen and Oxygen from the Corrosion of Magnesium in Water. *J. Electrochem. Soc.*, 161(9):C395–C404, jun 2014.

[48] S. J. Splinter and N. S. McIntyre. Initial interaction of water vapour with Mg-Al alloy surfaces at room temperature. *Surf. Sci.*, 314(2):157–171, 1994.

[49] S. Feliu, a. Pardo, M.C. Merino, a.E. Coy, F. Viejo, and R. Arrabal. Correlation between the surface chemistry and the atmospheric corrosion of AZ31, AZ80 and AZ91D magnesium alloys. *Appl. Surf. Sci.*, 255(7):4102–4108, 2009.

[50] Sebastián Feliu, C. Maffiotte, a. Samaniego, Juan Carlos Galván, and Violeta Barranco. Effect of the chemistry and structure of the native oxide surface film on the corrosion properties of commercial AZ31 and AZ61 alloys. *Appl. Surf. Sci.*, 257:8558–8568, 2011.

[51] Sochiko Ono. Surface phenomena and protective film growth on magnesium and magnesium alloys. *Mater. Sci. Technol.*, 16:91–104, 1998.

[52] Mara Cristina Lopes De Oliveira, Viviam Serra Marques Pereira, Olandir Vercino Correa, and Renato Altobelli Antunes. Corrosion performance of anodized

AZ91D magnesium alloy: Effect of the anodizing potential on the film structure and corrosion behavior. *J. Mater. Eng. Perform.*, 23(2):593–603, 2014.

[53] K A Gschneidner, B J Beaudry, and J Capellen. Rare Earth Metals. In *ASM Handbook, Vol. 2 Prop. Sel. Nonferrous Alloy. Spec. Mater.*, volume 2, pages 720–732. ASM International, 1990.

[54] X.Y Y. Wang and D.Y Y. Li. Effects of yttrium on mechanical properties and chemical stability of passive film of aluminide coating on 1045 steel. *Surf. Coatings Technol.*, 160(1):20–28, oct 2002.

[55] X.Y. Wang and D.Y. Li. Beneficial effects of yttrium on the mechanical failure and chemical stability of the passive film of 304 stainless steel. *Mater. Sci. Eng. A*, 315(1-2):158–165, sep 2001.

[56] Iulian Radu and D.Y. Li. Investigation of the role of oxide scale on Stellite 21 modified with yttrium in resisting wear at elevated temperatures. *Wear*, 259(1-6):453–458, jul 2005.

[57] S Krishnamurthy, M Khobaib, E Robertson, and F H Froes. Corrosion Behavior of Rapidly Solidified Mg-Nd and Mg-Y Alloys. *Mater. Sci. Eng.*, 99:507–511, 1988.

[58] M.F. Montemor, a.M. Simões, and M.J. Carmezim. Characterization of rare-earth conversion films formed on the AZ31 magnesium alloy and its relation with corrosion protection. *Appl. Surf. Sci.*, 253(16):6922–6931, jun 2007.

[59] N I U Jie-xin, Chen Qiu-rong, X U Nai-xin, and W E I Zhong-ling. Effect of combinative addition of strontium and rare earth elements on corrosion resistance of AZ91D magnesium alloy. *Trans. Nonferrous Met. Soc. China*, 18:1058–1064, 2008.

[60] Michiaki Yamasaki, Naoyuki Hayashi, Shogo Izumi, and Yoshihito Kawamura. Corrosion behavior of rapidly solidified MgZnrare earth element alloys in NaCl solution. *Corros. Sci.*, 49(1):255–262, jan 2007.

[61] A Samaniego, K Gusieva, I Llorente, S Feliu Jr, and N Birbilis. Exploring the possibility of protective surface oxides upon Mg alloy AZ31 via lutetium additions. *Corros. Sci.*, 89:101–110, 2014.

[62] F. Zucchi, V. Grassi, A. Frignani, C. Monticelli, and G. Trabanelli. Electrochemical behaviour of a magnesium alloy containing rare earth elements. *J. Appl. Electrochem.*, 36(2):195–204, 2006.

[63] N. D. Nam, J. G. Kim, K. S. Shin, and H. C. Jung. The effect of rare earth additions on the electrochemical properties of Mg-5Al-based alloys. *Scr. Mater.*, 63(6):625–628, 2010.

[64] Xuemin Wang, Xiaoqin Zeng, Guosong Wu, and Shoushan Yao. The effect of Y-ion implantation on the oxidation of AZ31 magnesium alloy. *Mater. Lett.*, 61(4-5):968–970, feb 2007.

[65] Xuemin Wang, Xiaoqin Zeng, Shoushan Yao, Guosong Wu, and Yijian Lai. The corrosion behavior of Ce-implanted magnesium alloys. *Mater. Charact.*, 59(5):618–623, 2008.

[66] H.B. Yao, Y. Li, and a.T.S. Wee. Passivity behavior of melt-spun MgY Alloys. *Electrochim. Acta*, 48(28):4197–4204, dec 2003.

[67] William R. Warke. Wear Filures. In *Princ. Fail. Anal.* ASM International, Materials Park, 2002.

[68] J.F. Nie, X. Gao, and S.M. Zhu. Enhanced age hardening response and creep resistance of MgGd alloys containing Zn. *Scr. Mater.*, 53(9):1049–1053, nov 2005.

[69] C. Sanchez, G. Nussbaum, P. Azavant, and H. Octor. Elevated temperature behaviour of rapidly solidified magnesium alloys containing rare earths. *Mater. Sci. Eng. A*, 221(1-2):48–57, dec 1996.

[70] K. Nakatsugawa, , I. , Kamado, , S. , Kojima, , Y. , Ninomiya, , R. , Kubota,. Corrosion of magnesium alloys containing rare earth. *Corros. Rev.*, 16(1-2):139–157.

[71] Xuemin Wang, Xiaoqin Zeng, Shoushan Yao, Guosong Wu, and Yijian Lai. The corrosion behavior of Ce-implanted magnesium alloys. *Mater. Charact.*, 59(5):618–623, may 2008.

[72] Yizhen Lu, Qudong Wang, Xiaoqin Zeng, Wenjiang Ding, and Chunquan Zhai. Effects of rare earths on the microstructure, properties and fracture behavior of Mg Al alloys. *Mater. Sci. Eng. A278*, 278:66–76, 2000.

[73] Chen Jun, Li Quanan, Li Jianghong, Li Xiaofeng, Li Kejie, and Zhang Xingyuan. Microstructure and mechanical properties of Mg-6Al magnesium alloy with yttrium and neodymium. *China Foundry*, 6(2):124–128, 2008.

[74] Guo Dong Tong, Hai Feng Liu, and Yao Hui Liu. Effect of rare earth additions on microstructure and mechanical properties of AZ91 magnesium alloys. *Trans. Nonferrous Met. Soc. China (English Ed.*, 20(SUPPL. 2):s336–s340, 2010.

[75] Y.B. Liu Q.J. Qi, X.H. Yang, Q Qi, YB Liu, and XH Yang. Effects of rare earths on friction and wear characteristics of magnesium alloy AZ91D. *Trans. Nonferrous Met. Soc. China*, 13(1):111–115, 2003.

[76] Tiancheng Zhang and D.Y. Y. Li. Improvement in the resistance of aluminum with yttria particles to sliding wear in air and in a corrosive medium. *Wear*, 251(1-12):1250–1256, oct 2001.

[77] W.B. Bouaeshi and D.Y. Li. Effects of Y2O3 addition on microstructure, mechanical properties, electrochemical behavior, and resistance to corrosive wear of aluminum. *Tribol. Int.*, 40(2):188–199, feb 2007.

[78] Iulian Radu and D. Y. Li. The wear performance of yttrium-modified Stellite 712 at elevated temperatures. *Tribol. Int.*, 40(2 SPEC. ISS.):254–265, 2007.

[79] Isao Nakatsugawa Masao Kiryuu, Hayato Okumura, Shigeharu KamaIdo, Yo Kojima, Ryuuji Ninomiya. Corrosion resistance of heat resistant magnesium alloys containing heavy rare earth elements. *J. Japan Inst. Light Met.*, 46(1):39–44, 1996.

[80] G99-05, 2010, Standard Test Method for Wear Testing with a Pin-on-Disk Apparatus, 2010.

[81] William Moffatt. *The handbook of binary phase diagrams*. General Electric Co., Corporate Research and Development,, Schenectady, N.Y. :, 1976.

[82] Y Li and H Jones. Effect of rare earth and silicon additions on structure and properties of l11eltspun Mg-9AI-1Zn alloy. *Mater. Sci. Technol.*, 12(August):651–661, 1996.

[83] T Rzychoń and A Kiełbus. Effect of rare earth elements on the microstructure of Mg-Al alloys. *AMME*, 17(1):149–152, 2006.

[84] Tao Zhang, Guozhe Meng, Yawei Shao, Zhongyu Cui, and Fuhui Wang. Corrosion of hot extrusion AZ91 magnesium alloy. Part II: Effect of rare earth element neodymium (Nd) on the corrosion behavior of extruded alloy. *Corros. Sci.*, 53(9):2934–2942, sep 2011.

[85] Kaveh Meshinchi Asl, Afshin Masoudi, and Farzad Khomamizadeh. The effect of different rare earth elements content on microstructure, mechanical and wear behavior of MgAlZn alloy. *Mater. Sci. Eng. A*, 527(7-8):2027–2035, mar 2010.

[86] Zhi-wei Huang, Yu-hui Zhao, Hua Hou, Yu-hong Zhao, Xiao-feng Niu, and Pei-de Han. Structural, thermodynamics and elastic properties of Mg17Al12, Al2Y and Al4Ba phases by first-principles calculations. *J. Cent. South Univ.*, 19(6):1475–1481, 2012.

[87] Xiaoguang Sun, Meisam Nouri, You Wang, and D.Y. Li. Corrosive wear resistance of MgAlZn alloys with alloyed yttrium. *Wear*, 302(1-2):1624–1632, apr 2013.

[88] Chao-Chi Jain, Ching-Yuan Bai, Shi-Wei Chen, and Chun-Hao Koo. The Microstructure and Mechanical Properties of AZ31-xRE Magnesium Alloys. *Mater. Trans.*, 48(5):1149–1156, 2007.

[89] Gui hua SU, Liang ZHANG, Li ren CHENG, Yong bing LIU, and Zhan yi CAO. Microstructure and mechanical properties of Mg-6Al-0.3Mn-xY alloys prepared by casting and hot rolling. *Trans. Nonferrous Met. Soc. China (English Ed.*, 20(3):383–389, 2010.

[90] D.Y. Li. Corrosive Wear. In Yip-Wah Wang, Q. Jane; Chung, editor, *Encycl. Tribol.* Springer, first edit edition, 2013.

[91] F. Rosalbino, E. Angelini, S. De Negri, a. Saccone, and S. Delfino. Effect of erbium addition on the corrosion behaviour of MgAl alloys. *Intermetallics*, 13(1):55–60, jan 2005.

[92] Xuehua Zhou, Yuanwei Huang, Zhongling Wei, Qiurong Chen, and Fuxing Gan. Improvement of corrosion resistance of AZ91D magnesium alloy by holmium addition. *Corros. Sci.*, 48(12):4223–4233, dec 2006.

[93] N N Aung and W Zhou. Effect of heat treatment on corrosion and electrochemical behaviour of AZ91D magnesium alloy. pages 1397–1401, 2003.

[94] J.R. Davis, editor. *ASM Specialty Handbook: Copper and Copper Alloys*. ASM International, 1 edition, 2001.

[95] Denny A. Jones. *Principles and Prevention of Corrosion*. Prentice Hall, 1995.

[96] J. M. Howe. *Interfaces in Materials: Atomic Structure, Kinetics and Thermodynamics of Solid-Vapor, Solid-Liquid and Solid-Solid Interfaces*. John Wiley & Sons, Inc., NY, first edit edition, 1997.

[97] S. Das, A. T. Morales, and A. T. Alpas. Microstructural evolution during high temperature sliding wear of Mg-3% Al-1% Zn (AZ31) alloy. *Wear*, 268(1):94–103, 2010.

[98] Katarzyna N Braszczyńska-Malik and Katarzyna N Braszczy. Precipitates of γ Mg 17 Al 12 Phase in AZ91 Alloy. In Frank Czerwinski, editor, *Magnes. Alloy. - Des. Process. Prop.*, chapter Five, pages 97–112. InTech, 2011.

[99] Yeshuang Wang, Qudong Wang, Chunjiang Ma, Wenjiang Ding, and Yanping Zhu. Effects of Zn and RE additions on the solidification behavior of Mg- 9Al magnesium alloy. *Mater. Sci. Eng. A*, 342:178–182, 2003.

[100] Hugh Avedesian, Michael M. , Baker, editor. *ASM Specialty Handbook Magnesium and Magnesium Alloys*. ASM International, 1999.

[101] S. Celotto and T. J. Bastow. Study of precipitation in aged binary Mg-Al and ternary Mg-Al-Zn alloys using 27Al NMR spectroscopy. *Acta Mater.*, 49(1):41–51, 2001.

[102] S. Celotto. TEM study of continuous precipitation in Mg9 wt%Al1 wt%Zn alloy. *Acta Mater.*, 48(8):1775–1787, may 2000.

[103] Fu-sheng Pan, Mei-bao Chen, Jing-feng Wang, Jian Peng, and Ai-tao Tang. Effects of yttrium addition on microstructure and mechanical properties of

as-extruded AZ31 magnesium alloys. *Trans. Nonferrous Met. Soc. China*, 18(50725413):s1–s6, dec 2008.

[104] Wei Qiu, Han Enhou, and Lu Liu. Microstructure and Mechanical Properties of Mg-3Al-1Zn-xRE Alloys. *J. Mater. Sci. Technol.*, 25(3):356–360, 2009.

[105] Zhi Ming Wang, Hao Ran Geng, Jin Feng Li, and Xin Ying Teng. Influence of Y and Ba on Microstructure and Mechanical Properties of AZ91 Magnesium Alloys. *Key Eng. Mater.*, 353-358:1593–1596, 2007.

[106] S. J. Wang, G. Q. Wu, R. H. Li, G. X. Luo, and Z. Huang. Microstructures and mechanical properties of 5 wt.% Al2Yp/Mg-Li composite. *Mater. Lett.*, 60(15):1863–1865, 2006.

[107] N. Kashefi and R. Mahmudi. The microstructure and impression creep behavior of cast AZ80 magnesium alloy with yttrium additions. *Mater. Des.*, 39:200–210, 2012.

[108] Zude Zhao, Qiang Chen, Yanbin Wang, and Dayu Shu. Microstructures and mechanical properties of AZ91D alloys with Y addition. *Mater. Sci. Eng. A*, 515(1-2):152–161, 2009.

[109] Guangling Song, Andrej Atrens, Xianliang Wu, and Bo Zhang. Corrosion behaviour of AZ21, AZ501 and AZ91 in Sodium Chloride. *Corros. Rev.*, 40(10):1769–1791, 1998.

[110] Jinghuai Zhang, Xiaodong Niu, Xin Qiu, Ke Liu, Changming Nan, Dingxiang Tang, and Jian Meng. Effect of yttrium-rich misch metal on the microstructures, mechanical properties and corrosion behavior of die cast AZ91 alloy. *J. Alloys Compd.*, 471(1-2):322–330, mar 2009.

[111] B.E. Hayden, E. Schweizer, R. Kotz, and A.M. Bradshaw. The early stages of oxidation of magnesium single crystal surfaces. *Surf. Sci.*, 111:26–38, 1981.

[112] P. M. Bradford, B. Case, G. Dearnaley, J. F. Turner, and I. S. Woolsey. Ion beam analysis of corrosion films on a high magnesium alloy (Magnox Al 80). *Corros. Sci.*, 16(10):747–766, 1976.

[113] C Chen, S J Splinter, T Do, and N S Mclntyre. Measurement of oxide film growth on Mg and Al surfaces over extended periods using XPS. *Surf. Sci.*, 382:L652–L657, 1997.

[114] H.B Yao, Y Li, and a.T.S Wee. An XPS investigation of the oxidation/corrosion of melt-spun Mg. *Appl. Surf. Sci.*, 158(1-2):112–119, may 2000.

[115] S. F. Liu, B. Li, X. H. Wang, W. Su, and H. Han. Refinement effect of cerium, calcium and strontium in AZ91 magnesium alloy. *J. Mater. Process. Technol.*, 209(8):3999–4004, 2009.

[116] Meisam Nouri, Xiaoguang Sun, and D.Y. Y. Li. Beneficial effects of yttrium on the performance of Mg3%Al alloy during wear, corrosion and corrosive wear. *Tribol. Int.*, 67:154–163, nov 2013.

[117] W.C. Oliver and G.M. Pharr. Measurement of hardness and elastic modulus by instrumented indentation: Advances in understanding and refinements to methodology. *J. Mater. Res.*, 19(01):3–20, mar 2011.

[118] Chiu Chen. *Studies of Oxide Growth on Some Al, Mg, and Mg Alloy Surfaces under Ambient Exposure Conditions*. Master of engineering science thesis, The University of Western Ontario, 1996.

[119] Raul Arrabal Sebastián, Feliu Jr., C. Maffiotte, Juan Carlos Galván, Angel Pardo, Maria Concepción Merino and Feliu Jr. Sebastián. The Application of X-Ray Photoelectron Spectroscopy in Understanding Corrosion Mechanisms of Magnesium and Mg-Al Alloys. *Open Surf. Sci. J.*, 3:1–14, 2011.

[120] Michael P. Marder. *Condensed Matter Physics*. John Wiley & Sons, Inc., 2010.

[121] Iulian Radu and D. Y. Li. A Further Study of the Beneficial Effects of Yttrium on Oxide Scale Properties and High-Temperature Wear of Stellite 21. *Tribol. Lett.*, 30(1):27–34, mar 2008.

[122] R. J. Hussey and M. J. Graham. The influence of reactive-element coatings on the high-temperature oxidation of pure-Cr and high-Cr-content alloys. *Oxid. Met.*, 45(3-4):349–374, 1996.

[123] Physical and optical properties of minerals. In David R. Lids, editor, *CRC Handb. Chem. Phys.*, chapter Physical a, pages 138–144. CRC Press/Taylor and Francis, Boca Raton, 1997.

[124] C B Baliga and P Tsakiropoulos. The structure and morphology of the corrosion products formed on the surfaces of a rapidly solidified Mg-3.5 Al alloy. *Mater. Sci. Eng. A*, 134(i):1029–1032, 1991.

[125] G Kresse and J Furthmiiller. Efficiency of ab-initio total energy calculations for metals and semiconductors using a plane-wave basis set. *Comput. Mater. Sci.*, 6:15–50, 1996.

[126] G. Kresse and J. Hafner. Ab initio molecular dynamics for liquid metals. *Phys. Rev. B*, 47(1):558–561, 1993.

[127] G Kresse and J Furthmu. Efficient iterative schemes for ab initio total-energy calculations using a plane-wave basis set. *Phys. Rev. B*, 54(16):11 169–11 186, 1996.

[128] G Kresse and D Joubert. From ultrasoft pseudopotentials to the projector augmented-wave method. *Phys. Rev. B*, 59(3):11–19, 1999.

[129] John P. Perdew, Kieron Burke, and Matthias Ernzerhof. Generalized Gradient Approximation Made Simple. *Phys. Rev. Lett.*, 77(18):3865–3868, oct 1996.

[130] Hendrik J Monkhorst and James D Pack. Special points for Brillonin-zone integrations. *Phys. Rev. B*, 13(12):5188–5192, 1976.

[131] P. Ravindran, Lars Fast, P. a. Korzhavyi, B. Johansson, J. Wills, and O. Eriksson. Density functional theory for calculation of elastic properties of orthorhombic crystals: Application to TiSi[sub 2]. *J. Appl. Phys.*, 84(9):4891, 1998.

[132] Z.R. Liu, J.H. Chen, S.B. Wang, D.W. Yuan, M.J. Yin, and C.L. Wu. The structure and the properties of S-phase in AlCuMg alloys. *Acta Mater.*, 59(19):7396–7405, nov 2011.

[133] S.F. Pugh. Relations between the elastic moduli and the plastic properties of polycrystalline pure metals. *Philos. Mag. Ser. 7*, 45(367):823–843, 1954.

[134] T. Hu, J.H. Chen, J.Z. Liu, Z.R. Liu, and C.L. Wu. The crystallographic and morphological evolution of the strengthening precipitates in CuNiSi alloys. *Acta Mater.*, 61(4):1210–1219, feb 2013.

[135] J.E. Gray and B. Luan. Protective coatings on magnesium and its alloys a critical review. *J. Alloys Compd.*, 336(1-2):88–113, apr 2002.

[136] J Kipkemoi and D Tsipas. Rare-earth modified chromium-aluminide coatings applied by pack cementation method on low-alloy steels. *J. Mater. Sci.*, 31:6247–6250, 1996.

[137] Jiu Ba Wen, Wei Zhang, Xiao Yuan Li, and Quan An Li. The Influence of La on the Corrosion Resistance of Hot-Dip Aluminized Steel. *Mater. Sci. Forum*, 475-479:3851–3854, 2005.

[138] Tiancheng Zhang and D.Y Y. Li. Beneficial effect of oxygen-active elements on the resistance of aluminide coatings to corrosive erosion and dry erosion. *Surf. Coatings Technol.*, 130(1):57–63, aug 2000.

[139] Hojat Ahmadi and D.Y Li. Mechanical and tribological properties of aluminide coating modified with yttrium. *Surf. Coatings Technol.*, 161(2-3):210–217, dec 2002.

[140] Tiancheng Zhang and D Y Li. Effects of cerium on dry sand erosion and corrosive erosion of aluminide coating on 1030 steel. *J. Mater. Sci. Lett.*, 9:429–432, 2000.

[141] Hojat Ahmadi and D.Y Y. Li. Beneficial effects of yttrium on mechanical properties and high-temperature wear behavior of surface aluminized 1045 steel. *Wear*, 255(7-12):933–942, aug 2003.

[142] Tiancheng Zhang, Yichun Luo, and D.Y Y. Li. Erosion behavior of aluminide coating modified with yttrium addition under different erosion conditions. *Surf. Coatings Technol.*, 126(2-3):102–109, apr 2000.

[143] M.-X. X. Zhang, H. Huang, K. Spencer, and Y.-N. N. Shi. Nanomechanics of MgAl intermetallic compounds. *Surf. Coatings Technol.*, 204(14):2118–2122, apr 2010.

[144] Tiancheng Zhang and D.Y Li. Effect of alloying yttrium on corrosionerosion behavior of 27Cr cast white iron in different corrosive slurries. *Mater. Sci. Eng. A*, 325(1-2):87–97, feb 2002.

[145] Linchun Wang and D.Y. Li. Effects of yttrium on microstructure, mechanical properties and high-temperature wear behavior of cast Stellite 6 alloy. *Wear*, 255(1-6):535–544, aug 2003.

[146] P Poddar, A Das, and K L Sahoo. Effect of rare earth elements on tribological behaviour of magnesium alloys. *Tribol. - Mater. Surfaces Interfaces*, 6(4):147–154, 2012.

[147] Ashok Kumar Mondal, B.S.S. S S Chandra Rao, and Subodh Kumar. Wear behaviour of AE42+20% saffil Mg-MMC. *Tribol. Int.*, 40(2):290–296, feb 2007.

[148] S.C Sharma, B Anand, and M Krishna. Evaluation of sliding wear behaviour of feldspar particle-reinforced magnesium alloy composites. *Wear*, 241(1):33–40, jun 2000.

[149] Anna Da Forno and Massimiliano Bestetti. A composite coating for corrosion and wear protection of AM60B magnesium alloy. In Stefano P. Trasatti and Juliet Ippolito, editors, *2nd Work. Corros. Model. Life Predict. (CMLP 2010)*, pages 79–84, Rome, Italy, 2010. TRANS TECH PUBLICATIONS LTD.

[150] Mustafa Aydin and Fehim Findik. Wear Properties of Magnesium Matrix Composites Reinforced with SiO2 Particles. *Ind. Lubr. Tribol.*, 62(4):232–237, 2010.

[151] Ali Arslan Kaya, Eyup Sabri Kayal, Dan Eliezer, G. Gertsberg, and N. Moscovitch. Addition of B₄C to AZ91 via Diecasting and Its Effect on Wear Behaviour. *Mater. Sci. Forum*, 488-489:741–744, 2005.

[152] Bin Hu, Liming Peng, Yanling Yang, and Wenjiang Ding. Effect of solidification conditions on microstructure, mechanical and wear properties of Mg5Al3Ca0.12Sr magnesium alloy. *Mater. Des.*, 31(8):3901–3907, sep 2010.

[153] Peter J Blau and Matthew Walukas. Sliding friction and wear of magnesium alloy AZ91D produced by two different methods. *Tribol. Int.*, 33(2000):573–579, 2008.

[154] L.A. Dobrzański, T. Tański, L. Čížek, J. Domagała, L.A. Dobrzanski, T. Tanski, L. Cizek, and J. Domagala. Mechanical properties and wear resistance of magnesium casting alloys. *J. Achiev. Mater. Manuf. Eng.*, 31(1):83–90, 2008.

[155] Kaveh Meshinchi Asl, Alireza Tari, and Farzad Khomamizadeh. Effect of deep

cryogenic treatment on microstructure, creep and wear behaviors of AZ91 magnesium alloy. *Mater. Sci. Eng. A*, 523(1-2):27–31, oct 2009.

[156] Y. Yang and H. Wu. Improving the wear resistance of AZ91D magnesium alloys by laser cladding with AlSi powders. *Mater. Lett.*, 63(1):19–21, jan 2009.

[157] R. G. Li, J. An, and Y. Lu. Friction and wear characteristics of Mg11Y2·5Zn magnesium alloy treated by laser surface melting. *Surf. Eng.*, 26(5):347–353, jul 2010.

[158] Kyouji Murayama, Atsuya Suzuki, Shigeharu Kamado, Yo Kojima, Yoshiro Ito, and Hitoshi Hiraga. Improvement of Wear Resistance of Magnesium by Laser-Alloying with Silicon. *Mater. Trans.*, 44(4):531–538, 2003.

[159] Hitishi Hiraga, Takashi Inoue, Shigeharu Kamado, and Yo Kojima. Improving the Wear Resistance of a Magnesium Alloy by Laser Melt Injection. *Mater. Trans.*, 42(7):1322–1325, 2001.

[160] X. P. Zhang, Z. P. Zhao, F. M. Wu, Y. L. Wang, and J. Wu. Corrosion and wear resistance of AZ91D magnesium alloy with and without microarc oxidation coating in Hank's solution. *J. Mater. Sci.*, 42(20):8523–8528, jun 2007.

[161] Bai Yang Lou, Bao Liang, and Xiao Li. The Influence of Micro-Arc Oxidation on Corrosive-Wear Behavior of Magnesium Alloy. *Appl. Mech. Mater.*, 55-57:1785–1788, may 2011.

[162] Ebru Emine Demirci, Ersin Arslan, Kadri Vefa Ezirmik, Özlem Baran, Yaar Totik, and Ihsan hsan Efeoglu. Investigation of wear, corrosion and tribocorrosion properties of AZ91 Mg alloy coated by micro arc oxidation process in the different electrolyte solutions. *Thin Solid Films*, 528:116–122, jan 2013.

[163] P. Li, M.K. K. Lei, X.P. P. Zhu, X.G. G. Han, C. Liu, and J.P. P. Xin. Wear

mechanism of AZ31 magnesium alloy irradiated by high-intensity pulsed ion beam. *Surf. Coatings Technol.*, 204(14):2152–2158, apr 2010.

[164] P. Li, M.K. Lei, and X.P. Zhu. Dry sliding tribological behavior of AZ31 magnesium alloy irradiated by high-intensity pulsed ion beam. *Appl. Surf. Sci.*, 257(1):72–81, oct 2010.

[165] H Hoche, H Scheerer, D Probst, E Broszeit, and C Berger. Development of a plasma surface treatment for magnesium alloys to ensure sufficient wear and corrosion resistance. *Surf. Coatings Technol.*, 174-175:1018–1023, 2003.

[166] J. Senf and E. Broszeit. Wear and Corrosion Protection of Aluminum and Magnesium Alloys Using Chromium and Chromium Nitride PVD Coatings. *Adv. Eng. Mater.*, 1(2):133–137, oct 1999.

[167] Guosong Wu, Wei Dai, He Zheng, and Aiying Wang. Improving wear resistance and corrosion resistance of AZ31 magnesium alloy by DLC/AlN/Al coating. *Surf. Coatings Technol.*, 205(7):2067–2073, dec 2010.

[168] Wei Jiu Huang, Rong Chang Zeng, and An Hua Chen. A Comparative Study on the Fretting Wear Resistant Properties of AZ91D and AM60B Magnesium Alloys. *Mater. Sci. Forum*, 488-489:745–748, 2005.

[169] M-X. Zhang and P. M. Kelly. Surface alloying of AZ91D alloy by diffusion coating. *J. Mater. Res.*, 17:2477–2479, 2002.

[170] Ma Youping, Xu Kewei, Wen Weixin, He Xipeng, and Liu Pengfei. The effect of solid diffusion surface alloying on properties of ZM5 magnesium alloy. *Surf. Coatings Technol.*, 190(2-3):165–170, jan 2005.

[171] Fencheng Liu, Wei Liang, Xianrong Li, Xingguo Zhao, Yan Zhang, and Hongxia Wang. Improvement of corrosion resistance of pure magnesium via vacuum pack treatment. *J. Alloys Compd.*, 461(1-2):399–403, aug 2008.

[172] Liqun Zhu and Guangling Song. Improved corrosion resistance of AZ91D magnesium alloy by an aluminium-alloyed coating. *Surf. Coatings Technol.*, 200(8):2834–2840, jan 2006.

[173] Haiyan Yang, Xingwu Guo, Guohua Wu, Shaohua Wang, and Wenjiang Ding. Continuous intermetallic compounds coatings on AZ91D Mg alloy fabricated by diffusion reaction of Mg-Al couples. *Surf. Coatings Technol.*, 205(8-9):2907–2913, 2011.

[174] J. Hirmke, M.-X. X. Zhang, and D.H. H. StJohn. Surface alloying of AZ91E alloy by Al-Zn packed powder diffusion coating. *Surf. Coatings Technol.*, 206(2-3):425–433, oct 2011.

[175] Xianrong Li, Wei Liang, Xingguo Zhao, Yan Zhang, Xiaopeng Fu, and Fencheng Liu. Bonding of Mg and Al with Mg Al eutectic alloy and its application in aluminum coating on magnesium. *J. Alloys Compd.*, 471:408–411, 2009.

[176] Fencheng Liu, Xianrong Li, Wei Liang, Xingguo Zhao, and Yan Zhang. Effect of temperature on microstructures and properties of aluminized coating on pure magnesium. *J. Alloys Compd.*, 478(1-2):579–585, jun 2009.

[177] You Ping Ma, Xiu Lan Li, Lei Yang, and Xi Peng He. Effect of surface diffusion alloying on erosion wear property of ZM5 magnesium alloy. *Trans. Nonferrous Met. Soc. China (English Ed.*, 23(2):323–328, 2013.

[178] Joon Sik Park, Jeong Min Kim, Ha Young Kim, Jae Seol Lee, Ik Hyun Oh, and Chang Suck Kang. Surface Protection Effect of Diffusion Pack Cementation Process by Al-Si Powders with Chloride Activator on Magnesium and Its Alloys. *Mater. Trans.*, 49(5):1048–1051, 2008.

[179] R Mola and Foundry Engineering. Fabrication and Microstructure of Lay-

ers Containing Intermetallic Phases on Magnesium. *Arch. FOUNDRY Eng.*, 13(1):99–102, 2013.

[180] I Shigematsu, M Nakamura, N Saitou, and K Shimojima. Surface treatment of AZ91D magnesium alloy by aluminum. *J. Mater. Sci. Lett.*, 9:473–475, 2000.

[181] H.Q. Sun, Y.N. Shi, M.-X. Zhang, and K. Lu. Surface alloying of an Mg alloy subjected to surface mechanical attrition treatment. *Surf. Coatings Technol.*, 202(16):3947–3953, may 2008.

[182] Jin Zhang, Ying Wang, Rong Chang Zeng, and Wei Jiu Huang. Effects of Post Heat Treatment on the Interfacial Characteristics of Aluminum Coated AZ91D Magnesium Alloy. *Mater. Sci. Forum*, 546-549:529–532, 2007.

[183] J.S. Park, J.M. Kim, H.Y. Kim, C.S. Kang, and S.W. Choi. Surface Protection of Magnesium Alloys via Pack Cementation Coatings with Aluminum Powder and Chlorides. *Mater. Sci. Forum*, 638-642:793–798, jan 2010.

[184] Meifeng He, Lei Liu, Yating Wu, Zhixin Tang, and Wenbin Hu. Improvement of the properties of AZ91D magnesium alloy by treatment with a molten AlCl3NaCl salt to form an MgAl intermetallic surface layer. *J. Coatings Technol. Res.*, 6(3):407–411, oct 2008.

[185] Meifeng He, Lei Liu, Yating Wu, Cheng Zhong, and Wenbin Hu. Influence of microstructure on corrosion properties of multilayer MgAl intermetallic compound coating. *Corros. Sci.*, 53(4):1312–1321, apr 2011.

[186] Jifu Zhang, Chuanwei Yan, and Fuhui Wang. Applied Surface Science Electrodeposition of Al Mn alloy on AZ31B magnesium alloy in molten salts. *Appl. Surf. Sci.*, 255:4926–4932, 2009.

[187] C. Zhong, M.F. F. He, L. Liu, Y.J. J. Chen, B. Shen, Y.T. T. Wu, Y.D. D. Deng, and W.B. B. Hu. Formation of an aluminum-alloyed coating on AZ91D

magnesium alloy in molten salts at lower temperature. *Surf. Coatings Technol.*, 205(7):2412–2418, dec 2010.

[188] Cheng Zhong, Meifeng He, Lei Liu, Yating Wu, Yujuan Chen, Yida Deng, Bin Shen, and Wenbin Hu. Lower temperature fabrication of continuous intermetallic coatings on AZ91D magnesium alloy in molten salts. *J. Alloys Compd.*, 504(2):377–381, aug 2010.

[189] Jingjing Le, Lei Liu, Fan Liu, Yida Deng, Cheng Zhong, and Wenbin Hu. Interdiffusion kinetics of the intermetallic coatings on AZ91D magnesium alloy formed in molten salts at lower temperatures. *J. Alloys Compd.*, 610:173–179, oct 2014.

[190] Yongshan Tao, Tianying Xiong, Chao Sun, Lingyan Kong, Xinyu Cui, Tiefan Li, and Guang Ling Song. Microstructure and corrosion performance of a cold sprayed aluminium coating on AZ91D magnesium alloy. *Corros. Sci.*, 52(10):3191–3197, 2010.

[191] A. Pardo, P Casajus, M. Mohedano, A. E. Coy, F. Viejo, B. Torres, E. Matykina, P. Casajús, M. Mohedano, A. E. Coy, F. Viejo, B. Torres, and E. Matykina. Corrosion protection of Mg/Al alloys by thermal sprayed aluminium coatings. *Appl. Surf. Sci.*, 255(15):6968–6977, 2009.

[192] Haiyan Yang, Xingwu Guo, Guohua Wu, Wenjiang Ding, and Nick Birbilis. Electrodeposition of chemically and mechanically protective Al-coatings on AZ91D Mg alloy. *Corros. Sci.*, 53(1):381–387, 2011.

[193] Ch Christoglou, N Voudouris, G N Angelopoulos, M Pant, and W Dahl. Deposition of aluminium on magnesium by a CVD process. *Surf. Coatings Technol. 184*, 184:149–155, 2004.

[194] Lin Hai Tian, Rui Hua Zhu, Yan Zhang, and Bin Tang. Microstructure and

Corrosion Resistance of Aluminized Coatings on Magnesium Alloy by Pulsed Bias Magnetron Sputtering. *Mater. Sci. Forum*, 687:688–693, jun 2011.

[195] Liu-ho Chiu, Chun-chin Chen, and Chih-fu Yang. Improvement of corrosion properties in an aluminum-sprayed AZ31 magnesium alloy by a post-hot pressing and anodizing treatment. *Surf. Coat. Technol.*, 191:181–187, 2005.

[196] X.Y. Mao, D.Y. Li, F. Fang, R.S. Tan, and J.Q. Jiang. A simple technique of nanocrystallizing metallic surfaces for enhanced resistances to mechanical and electrochemical attacks. *Mater. Sci. Eng. A*, 527(12):2875–2880, may 2010.

[197] X.Y. Mao, D.Y. Li, F. Fang, R.S. Tan, and J.Q. Jiang. Application of a simple surface nanocrystallization process to a Cu30Ni alloy for enhanced resistances to wear and corrosive wear. *Wear*, 271(9-10):1224–1230, jul 2011.

[198] C. Chen, D.Y. Li, and C.J. Shang. Nanocrystallization of aluminized surface of carbon steel for enhanced resistances to corrosion and corrosive wear. *Electrochim. Acta*, 55(1):118–124, dec 2009.

[199] Arne K Dahle, Young C Lee, Mark D Nave, Paul L Scha, and David H Stjohn. Development of the as-cast microstructure in magnesium aluminium alloys. *J. Light Met.*, 1:61–72, 2001.

[200] Lee P Barber. *Characterization of the Solidification Behavior and Resultant Microstructures of Magnesium-Aluminum Alloys*. PhD thesis, Worcester Polytechnic Iinstitute, 2004.

[201] K Lu and J Lu. Surface nanocrystallization (SNC) of metallic materials-presentation of the concept behind a new approach. *J. Mater. Sci. Technol.*, 15(3):193–197, 1999.

[202] George E Dieter. *Mechanical Metallurgy*. McGraw-Hill, Singapore, si metric edition, 1988.

[203] Ying-hui Wei, Bao-sheng Liu, Li-feng Hou, Bing-she Xu, and Gang Liu. Characterization and properties of nanocrystalline surface layer in Mg alloy induced by surface mechanical attrition treatment. *J. Alloys Compd.*, 452(2):336–342, 2008.

[204] Sareh Mosleh-Shirazi, Guomin Hua, Farshad Akhlaghi, Xianguo Yan, and Dongyang Li. Interfacial valence electron localization and the corrosion resistance of Al-SiC nanocomposite. *Sci. Rep.*, 5:18154, 2015.

[205] Zirun Yang, Hao Lu, Ziran Liu, Xianguo Yan, and Dongyang Li. Effect of particle size on the surface activity of TiCNi composite coating via the interfacial valence electron localization. *RSC Adv.*, 6(23):18793–18799, 2016.

[206] Ming Chun Zhao, Ming Liu, Guangling Song, and Andrej Atrens. Influence of the beta-phase morphology on the corrosion of the Mg alloy AZ91. *Corros. Sci.*, 50:1939–1953, 2008.

[207] Jr S Feliu, J C Galván, A Pardo, M C Merino, and R Arrabal. Native Air-Formed Oxide Film and its Effect on Magnesium Alloys Corrosion. *Open Corros. J.*, 3:80–91, 2010.